Improvements in the LES modelling of the stable boundary layer

Modifications to the prognostic subgrid TKE equation

V. N. Vertregt

TUDelft
Delft
University of
Technology

Challenge the future

Improvements in the LES modelling of the stable boundary layer

Modifications to the prognostic subgrid TKE equation

by

V. N. Vertregt

in partial fulfilment of the requirements for the degree of

Master of Science

in Applied Physics

at the Delft University of Technology,

to be defended publicly on September 30, 2015 at 15:00

Student number: 4003969
Project duration: October, 2014 – September, 2015
Supervisor: dr. S. R. de Roode
Thesis committee: Prof. dr. H. Jonker,   TU Delft
                     Dr. ir. M. J. B. M. Pourquie TU Delft

TUDelft
Delft
University of
Technology

CONTENTS

1

INTRODUCTION

1.1. MOTIVATION - WIND PREDICTION

In the past few years, energy production from renewable resources such as wind have become increasingly important. As the power output of the wind turbines is dependent on the wind speed, good weather and wind predictions are vital to plan overall energy production. At this time, weather models with a spatial resolution of ≈ 10 km are used for this purpose. However, turbulent eddies in the atmosphere are typical much smaller than this grid size, and are not explicitly calculated in the models. These turbulent effects are important in the local wind strength and profile, and incorporating them in a local model might therefore be very beneficial for accurately the predicting of power output of wind farms.

Large Eddy Simulation (LES) is a way to take the turbulent eddies into account and therefore provide accurate wind predictions on a small scale. However in stable atmospheric conditions, for instance during the night or on cold winter days, LES results can be unreliable. Why is this problematic for the wind prediction for wind farms? In stable atmospheric conditions there is little vertical mixing in the atmosphere, in which a local wind maximum, called the *nocturnal jet*, can be formed. Figure 1.1 shows the horizontal wind speed from two high resolution LES runs, in which a nocturnal jets are formed.
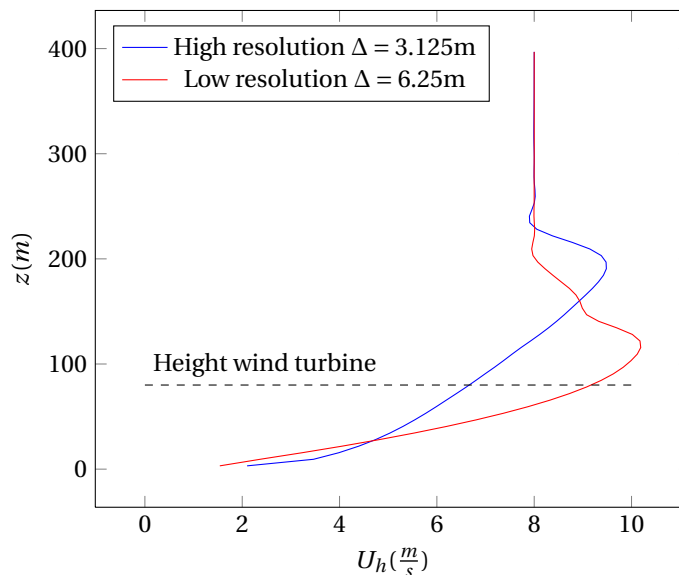
Figure 1.1: Nocturnal jet in stable atmospheric conditions, as produced in two LES simulations with a different resolution

Because of the vertical gradient in the wind speed and the formation of the nocturnal jet, small errors in the LES results can lead to big differences in predicted wind speed at the height of wind turbines, typically 80

m. Figure 1.1 shows the results of the same situation, but simulated at two different resolutions. It is clear that the predicted wind speed at 80 m differs substantially. In this thesis the reason behind the unreliability of LES modelling in stable conditions will be researched, as well as proposed changes to improve the LES framework.

1.2. LES MODELLING OF THE ATMOSPHERIC BOUNDARY LAYER

LES is a way to take local turbulent effects into account when modelling the evolution temperature, velocity and pressure in the atmosphere. The computational domain is divided in a grid. At each grid point, the filtered Navier-Stokes equations are numerically solved. In this way, the larger, energy containing eddies are explicitly calculated, or *resolved*. Motions smaller than the grid size are parametrized and enter the equations as *subgrid fluxes*. Several methods exist to do this parametrization, in this thesis the *prognostic TKE equation* will be examined.

The correct functioning of the LES model depends on the size of the grid compared to the size of the energy containing eddies. When the size of the grid is smaller than the size of the eddies, the important turbulent motions will be resolved and the LES model will yield usable results. If the energy containing eddies are smaller than the applied grid size, the solution is *subgrid dominated*. The solutions of the LES model will then not depend on the filtered Navier-Stokes equations themselves, but rather on parametrizations of the motions.

(a) Unstable atmosphere   (b) Stable atmosphere
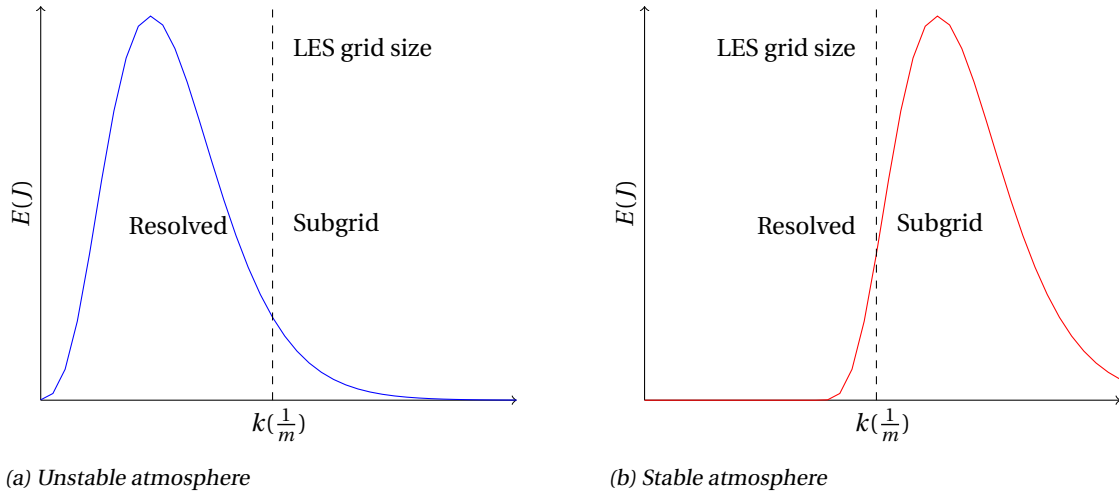
Figure 1.2: The difference in turbulent kinetic energy in the atmosphere between stable and unstable atmospheric conditions, compared to LES grid size.

For modelling the atmospheric boundary layer, this proves a challenge as the size of the energy containing eddies can vary a lot depending on the conditions. For a sunny day with a lot of cloud formation, a grid size of 50 m suffices to capture the important behaviour, while a stable boundary layer in a cold winter night would need grid sizes of around 10 m, according to [1]. Figure 1.2 illustrates the situation when LES simulation is done using the same grid size in the two different situations.

As will be shown in this thesis, subgrid dominated solutions suffer from serious problems, yielding unreliable answers. Solutions do not follow experimental results, and are not robust to - for instance - changes in the grid resolutions. This of course no desirable outcome. One possible solution would be to vary the grid resolution with the stability of the atmosphere, in order to always resolve the most important turbulent motions. For practical reasons, this is not a useful solution: this implies a two step process in order to do useful simulations.

In this thesis the behaviour of subgrid dominated LES results will be researched, as well as several options to improve the results of LES models in stable atmospheric conditions. One of the most important ideas is described by Sullivan *et al.* [2], which will be the main focus point of this thesis.

1.3. DALES

The *Dutch Atmospheric Large Eddy Simulation* (DALES), described by Heus *et al.* [3], is a LES model developed and extensively used by researchers from Delft University of Technology, Wageningen University, Utrecht University and the Royal Netherlands Meteorological Institute, all based in the Netherlands. It formed the basis of the GPU version (GALES) of the original code, which Schalkwijk [4] used to perform high resolution weather forecasts for the entire Netherlands. The original code of DALES version 4.0 will be used and adapted to test several improvements of the LES model, in order to produce more reliable results in stable atmospheric conditions.

1.4. OUTLINE

In the Chapter 2 LES Framework, the important equations behind the LES code used in DALES will be explained as well as the Monin-Obukhov similarity theory which is used to assess the results. The Chapter 3 will describe the GABLS case on which the different models will be tested. Chapter 4 will show how the original code of DALES performs in modelling the stable boundary, and where it fails. In Chapter 5 will be a derivation and explanation of the model proposed by Sullivan *et al.* [2] and some adaptions. The Chapter 6 will discuss the performance of the new model. In the Chapter 7 the drawbacks and advantages of the different alternatives will be compared. Finally, an outlook into further research directions will be given. In the Appendices, results from all simulations will given in order to provide a complete view of the different models.

2

LES FRAMEWORK

In this chapter first a theoretical background will be given for the LES framework, and in particular the closure model used in DALES, called the prognostic subgrid TKE equation. Secondly the similarity theory of Monin and Obukhov [5] will be introduced, a empirical scaling theory with which the LES results will be compared. As explained in the Introduction, subgrid dominated LES solutions do not agree with these empirical results.

As different authors use quite different notation for equations, the notation used in this thesis will be introduced first. Every explicitly calculated quantity x (e.g. velocity u_i and potential temperature θ_v) can be written as the sum of the filtered ($\widetilde{x}$) and the fluctuating (x') part. The filtered quantities will be resolved by the model, while the fluctuations are not.

$$x = \widetilde{x} + x' \tag{2.1}$$

The values of $\widetilde{x}$ are known at grid cells, the values x' are not. The filtered equations will include a filtered product of two terms $\widetilde{x'y'}$. The following notation will be used:

$$\widetilde{xy} = \widetilde{x}\widetilde{y} + \widetilde{x'y'} \tag{2.2}$$

As only $\widetilde{x}$ and $\widetilde{y}$ are explicitly calculated in the LES framework, the quantity $\widetilde{x'y'}$ is not known and must therefore be *parameterized*.

Often filtered quantities are averaged over the whole horizontal domain, this is denoted by $\langle \widetilde{x} \rangle$ and called the *slab averaged* value. Usually this is done for producing statistics, however, the Sullivan model depends heavily on the slab avering operation. The usual rules for averaging are valid: $\langle x + y \rangle = \langle x \rangle + \langle y \rangle$ and $\langle Cx \rangle = C \langle x \rangle$, where x and y are resolved quantities and C is a constant.

2.1. THE LES EQUATIONS

The LES equations can be derived from the Navier-Stokes equations using filtering and applying the Boussinesq approximation. An elaborate derivation can be found in Wyngaard [6]. The LES equations used in the DALES code are given by:

$$\frac{\partial \widetilde{u_i}}{\partial t} + \frac{\partial \widetilde{u_j}\widetilde{u_i}}{\partial x_j} = -\frac{\partial \widetilde{\pi}}{\partial x_i} + \frac{\widetilde{\theta_v}}{\theta_0} g \delta_{i3} - \frac{\partial \tau_{ij}}{\partial x_j} + F_i \tag{2.3}$$

$$\frac{\partial \widetilde{\theta_v}}{\partial t} + \frac{\partial \widetilde{u_j}\widetilde{\theta_v}}{\partial x_j} = -\frac{\partial \widetilde{u'_j \theta'_v}}{\partial x_j} \tag{2.4}$$

In this set of equations - and of course, in the remainder of the thesis - the symbols t, u_i, δ_{ij} and x_i have their usual meaning. The term π is the modified pressure, given by $\widetilde{\pi} = \frac{\bar{p}}{\rho_0} + \frac{2}{3}e$. The term ρ_0 is the atmospheric

reference density, p is the pressure and e is the subgrid turbulent kinetic energy, or *subgrid TKE*. This is given by:

$$e = \frac{1}{2}\widetilde{u_i' u_i'} \tag{2.5}$$

θ_v is the *virtual potential temperature*, the theoretical potential temperature of dry air with the same density as moist air. The *potential temperature* is the temperature which an air parcel would have if brought adiabatically brought to the reference pressure. Further information can be found in, for instance, the book of Stull [7]. The following relation holds:

$$\frac{\theta_v'}{\langle\widetilde{\theta_v}\rangle} = \frac{-\rho'}{\langle\widetilde{\rho}\rangle} \tag{2.6}$$

The physical interpretation of this quantity is as follows: if an air parcel has a higher θ_v than its surroundings, it experiences a buoyancy force upwards and visa versa. A precise definition and formula can be found in Heus *et al.* [3]. The term τ_{ij} is called the deviatoric subgrid stress tensor, and is given by:

$$\tau_{ij} = \widetilde{u_i' u_j'} - \frac{2}{3}e\delta_{ij} \tag{2.7}$$

Finally, the term F_i is a combination of other body forces on the atmosphere, such as the Coriolis force. By numerically integrating the equations 2.3 and 2.4 in time, values for $\widetilde{u_i}$ and $\widetilde{\theta_v}$ can be calculated, *provided that e, τ_{ij} and $\widetilde{u_j'\theta_v'}$ are known*. This is called the *closure problem*. In the prognostic subgrid TKE model, a third equation is solved for the subgrid TKE e. The subgrid TKE combined with a length scale λ are used to parametrize the subgrid shear τ_{ij} and subgrid buoyancy flux $\widetilde{u_j'\theta_v'}$.

2.1.1. Parametrization and the prognostic TKE equation

One of the unknown variables needed to solve the LES equations, is the turbulent kinetic energy $e = 1/2\widetilde{u_i'u_i'}$. This is the difference between the filtered total kinetic energy $1/2\widetilde{u_i u_i}$ and the kinetic energy of the filtered velocity field $1/2\widetilde{u_i}\widetilde{u_i}$. The TKE equation used in DALES is:

$$\underbrace{\frac{\partial e}{\partial t}}_{I} + \underbrace{\widetilde{u_j}\frac{\partial e}{\partial x_j}}_{II} = \underbrace{\frac{\widetilde{w'\theta_v'}}{\theta_0}g}_{P_b} - \underbrace{\tau_{ij}\frac{\partial \widetilde{u_i}}{\partial x_j}}_{P_s} - \underbrace{\frac{\partial \widetilde{\pi' u_j'}}{\partial x_j}}_{III} - \underbrace{\frac{\partial \widetilde{e' u_j'}}{\partial x_j}}_{IV} - \epsilon \tag{2.8}$$

The first term (I) on the left hand side is the storage of subgrid TKE and the second term (II) is the advection of subgrid TKE by the resolved flow: together they form the material derivative of TKE. The term P_b on the right hand side is TKE production/destruction due to variations in θ_v. The term P_s is production of TKE by turbulent shear. The term III is the transport of TKE by pressure fluctuation. The term IV is transport of TKE due to fluctuations of TKE. The final term ϵ is dissipation of subgrid TKE by viscous processes.

Because only the filtered quantities are calculated in the LES modelling, both the LES and the TKE equation contain some unknown quantities, which include the terms $\widetilde{u_i' u_j'}$, $\widetilde{\theta_v' u_j'}$ or $\widetilde{\pi' u_j'}$. These need to be parametrized, using known variables. The following parametrizations are used:

$$\tau_{ij} = -K_m\left(\frac{\partial \widetilde{u_i}}{\partial x_j} + \frac{\partial \widetilde{u_j}}{\partial x_i}\right) = -2K_m S_{ij} \tag{2.9}$$

$$\widetilde{\theta_v' u_j'} = -K_h \frac{\partial \widetilde{\theta_v}}{\partial x_j} \equiv -K_h \frac{\theta_0}{g}N^2 \tag{2.10}$$

$$\widetilde{\pi' u_j'} + \widetilde{e' u_j'} = -K_m \frac{\partial e}{\partial x_j} \tag{2.11}$$

With these parametrizations, all unknown terms can be expressed in filtered quantities, which are explicitly calculated. The quantity $N = \sqrt{\frac{g}{\theta_0}\frac{\partial \widetilde{\theta_v}}{\partial z}}$ is called the Brunt-Väisälä frequency, which is to the frequency of an

air parcel oscillating due to θ_v differences. The only thing necessary for closure is then a formula for the K_m and the K_h and the dissipation ϵ. In DALES, all these terms are expressed in terms of the TKE:

$$K_m = c_m \lambda \sqrt{e} \tag{2.12}$$

$$K_h = c_h \lambda \sqrt{e} \tag{2.13}$$

$$\epsilon = \frac{c_\epsilon}{\lambda} e^{3/2} \tag{2.14}$$

In these equations c_m is a model constant which follow from theory and λ is a typical length scale for the turbulent eddies, for which two options exist in the DALES code. The length scale is either defined by $\lambda = \Delta = (\Delta x \Delta y \Delta z)^{1/3}$, were $\Delta x, y, z$ are the grid spacings, or:

$$\lambda = \min(\Delta, c_n \frac{\sqrt{e}}{N}) \tag{2.15}$$

In this equation, $c_n = 0.76$. The term $c_n e/N$ is the Deardorff length scale ([8]), which is the length a air parcel with given energy can travel before all the kinetic energy is transferred to potential energy. The constants c_h and c_ϵ are given by:

$$c_h = (c_{h,1} + c_{h,2}\frac{\lambda}{\Delta})c_m \tag{2.16}$$

$$c_\epsilon = c_{\epsilon,1} + c_{\epsilon,2}\frac{\lambda}{\Delta} \tag{2.17}$$

The $c_h, 1, 2$ and $c_{\epsilon,1,2}$ are constants in the DALES code. Implementing the parametrisations of Formula 2.9, 2.10 and 2.11 in the subgrid TKE equations (2.8) yields the following model:

$$\frac{\partial e^{1/2}}{\partial t} + \widetilde{u_j}\frac{\partial e^{1/2}}{\partial x_j} = \frac{1}{2e^{1/2}}(\underbrace{-K_h N^2}_{P_b} + \underbrace{K_m S^2}_{P_s}) + K_m \frac{\partial e^{1/2}}{\partial x_j} - \frac{c_\epsilon e}{2\lambda} \tag{2.18}$$

In this equation, $S^2 = 2\sum_{i,j} S_{ij}S_{ij}$. The derivation of this formula can be found in Appendix A. All the numerical values of the subgrid constants can be found in Heus *et al.* [3].

2.1.2. DISCRETIZATION OF THE EQUATIONS

The DALES code is discretized using a Awakara-C grid, which is given in Figure 2.1. The velocity components u, v and w are defined at the cell faces, while the pressure, subgrid TKE and other scalar quantities are located in the cell center.

It is clear from Figure 2.1 that the velocity components u, v, w are defined at different points in the grid structure, which influences the implementation of the Sullivan based models and boundary conditions at ground level. Figure 2.2 contains an schematic drawing of the lowest grid levels:
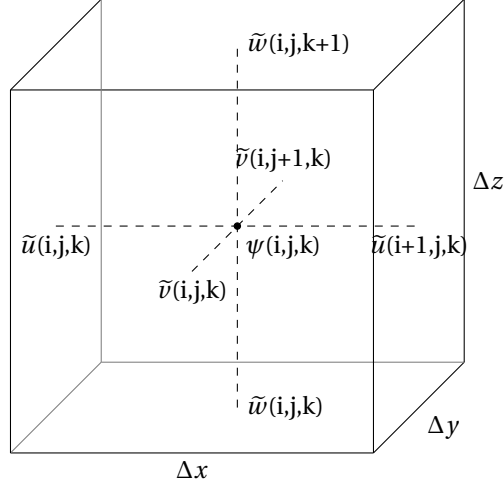
Figure 2.1: Definition of the grid used in DALES, $\psi = \{e, \widetilde{p}, \widetilde{\theta_v}\}$
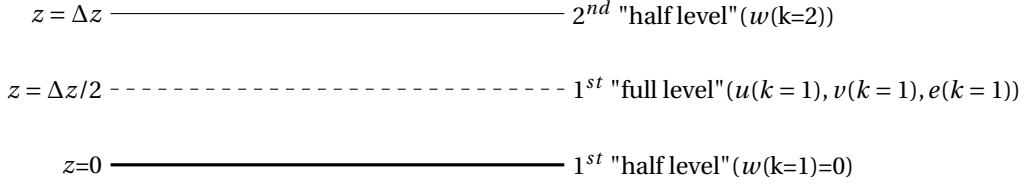
Figure 2.2: Surface boundary in the DALES framework

2.2. SIMILARITY RELATIONS

Much research has been done in non-dimensional relation to describe the parametrisation of turbulent fluxes in the atmosphere. Monin and Obukhov [5] introduced the usage of non-dimensional forms of the wind gradient and the temperature gradient, also called *stability* or *similarity functions*, given by:

$$\phi_m = \frac{\kappa z}{u_*} \frac{\partial U_h}{\partial z} \tag{2.19}$$

$$\phi_h = -\frac{\kappa z u_*}{\overline{w\theta_v}} \frac{\partial \theta_v}{\partial z} \tag{2.20}$$

In this equation, ϕ_m and ϕ_h are the similarity functions, $\kappa = 0.4$ is the Von Kárman constant, $U_h = \sqrt{u^2 + v^2}$ is the horizontal wind velocity and u_* and $\overline{w'\theta_v'}$ are respectively the friction velocity and the total buoyancy flux. The friction velocity is given by:

$$u_* = \sqrt[4]{\overline{uw}^2 + \overline{vw}^2} \tag{2.21}$$

In this equation $\overline{u'w'}$ indicates the total uw momentum flux. The bar $\overline{x}$ is used to indicate that these quantities are *not* LES specific: they can be measured. This has been done by among others Businger *et al.* [9]. In this thesis, we use the local scaling theory following Baas *et al.* [10] and introduced by Nieuwstadt [11]. The measurements en theory suggest that the similarity functions ϕ_m and ϕ_h both follow the following relation in the stable boundary layer:

$$\phi = 1 + \alpha \frac{z}{\Lambda} \tag{2.22}$$

In this equation, α is a constant, found to be approximately 5 by Businger *et al.* [9] and Λ is the *local* Monin-Obukhov length and is given by:

$$\Lambda = \frac{-(u_*)^3}{\kappa \frac{g}{\theta_0} \overline{w\theta_v}} \tag{2.23}$$

What exactly defines a stable or unstable boundary layer? This depends on the amount and sign of the shear and the buoyancy term, combined in the *gradient Richardson number,* here expressed in the LES terms (Garratt [12]):

$$Ri_g = \frac{N^2}{S^2} = \frac{\frac{g}{\theta_0} \frac{\partial \widetilde{\theta_v}}{\partial z}}{\left(\frac{\partial \widetilde{u}}{\partial z}\right)^2 + \left(\frac{\partial \widetilde{v}}{\partial z}\right)^2} \tag{2.24}$$

Ri_g is negative in an unstable boundary layer: the buoyancy force then accelerates rising air parcels, producing turbulent eddies and the buoyancy term in the subgrid TKE equation produces TKE. Ri_g is positive in an stable boundary layer: the buoyancy force then decelerates rising air parcels and so destroys turbulent eddies, the buoyancy term in the TKE equations also destroys subgrid TKE. If the $Ri_g > Ri_{\text{critical}} \approx 0.3$, then the atmosphere changes from turbulent to laminar.

2.2.1. Similarity functions in subgrid dominated DALES solutions

If the DALES solution is dominated by the subgrid, the Monin Obukhov functions can be evaluated theoretical. It this case, the total momentum and buoyancy flux only consist of subgrid fluxes:

$$u_* = \sqrt[4]{\overline{u'w'}^2 + \overline{v'w'}^2} = \sqrt[4]{\tau_{uw}^2 + \tau_{vw}^2}$$

$$\overline{w'\theta_v'} = \widetilde{w'\theta_v'}$$

The buoyancy flux can be rewritten using the parametrizations from Formula 2.10:

$$\frac{\widetilde{w'\theta_v'}}{u^*} = -\frac{K_h}{u_*} \frac{\partial \widetilde{\theta_v}}{\partial z} \tag{2.25}$$

For rewriting u_*, some more assumptions are necessary. Substituting the parametrization from Formula 2.9 and assuming a horizontally homogeneous solution yields:

$$u_* = \sqrt[4]{\tau_{uw}^2 + \tau_{vw}^2} = \sqrt[4]{K_m^2 \left[\left(\frac{\partial \widetilde{u}}{\partial z} + \frac{\partial \widetilde{w}}{\partial x}\right)^2 + \left(\frac{\partial \widetilde{v}}{\partial z} + \frac{\partial \widetilde{w}}{\partial y}\right)^2\right]} = K_m^{\frac{1}{2}} \sqrt{\frac{\partial U_h}{\partial z}} \tag{2.26}$$

The second equality follows because $\frac{\partial}{\partial x,y}$ are zero if the solution is homogeneous. Moreover, $\widetilde{w} = 0$ if there are no resolved fluctuations. By dividing the similarity functions from Formulas 2.19 and 2.20, and substituting the previous results:

$$\frac{\phi_h}{\phi_m} = \frac{-\frac{\kappa z u_*}{\widetilde{w'\theta_v'}} \frac{\partial \widetilde{\theta_v}}{\partial z}}{\frac{\kappa z}{u^*} \frac{\partial U_h}{\partial z}} = \frac{K_m \frac{\partial U_s}{\partial z} \frac{\partial \widetilde{\theta_v}}{\partial z}}{K_h \frac{\partial \widetilde{\theta_v}}{\partial z} \frac{\partial U_h}{\partial z}} = \frac{K_m}{K_h} \equiv Pr_t \tag{2.27}$$

The number Pr_t is called the turbulent Prandtl number, and is found to be 1 by Businger *et al.* [9]. From substituting the definitions of $K_{m,h}$, Formulas 2.12 and 2.13, the expression can be rewritten to:

$$Pr_t = \frac{c_m}{c_h} = \frac{c_m}{\left(c_{h,1} + c_{h,2} \frac{\lambda}{\Delta}\right) c_m} = \frac{1}{c_{h,1} + c_{h,2} \frac{\lambda}{\Delta}} \tag{2.28}$$

Substituting the definition of c_h from Formula 2.16 leads to the second equality. Apparently, in a subgrid dominated DALES solution, the turbulent Prandtl number and the ratio between ϕ_m and ϕ_h depend on the exact values of $c_{h,1}$ and $c_{h,2}$ and the chosen value for the length scale λ. As $c_{h,1} = 1$, the turbulent Prandtl number can only be set to 1 in the subgrid dominated solution if $c_{h,2}$ is chosen to be zero.

2.2.2. MONIN OBUKHOV OBEYING LENGTH SCALE

The previous section shows that constants in the DALES code directly influence the behaviour of the Monin Obukhov stability functions in case of subgrid dominated solutions. One of the parameters in the LES framework is the length scale λ, associated with a typical eddy size. How should λ be chosen such that the subgrid dominated DALES solution follows Monin Obukhov? The following derivations up to 2.34 follows the article of Duynkerke and Roode [13]. First, the Monin Obukhov function for momentum ϕ_h, Formula 2.20 needs to be rewritten in terms of non-dimensional quantities:

$$\phi_m \equiv \frac{\kappa z}{u_*} \frac{\partial U_h}{\partial z} = \frac{\kappa z u_*^2}{u_*^3} \frac{\partial U_h}{\partial z} = \frac{K_m}{K_h N^2} \left(\frac{\partial U_h}{\partial z}\right)^2 \frac{z}{\Lambda} \tag{2.29}$$

In the third step, two substitutions are done. First, from the definition of the Monin Obukhov length in Formula 2.23 follows that:

$$\frac{u_*^3}{\kappa} = -\Lambda \frac{g}{\theta_0} \widetilde{w'\theta_v'} = \Lambda K_h N^2$$

In the second equivalence the parameterization in DALES (Formula 2.10) is used. The final step is substituting the approximation made in Formula 2.26 for the definition of u_*. In order to simplify 2.29 even more, some assumptions are made. If there is no vertical resolved velocity $\widetilde{w}$, and the velocity field is horizontally homogeneous, then:

$$S^2 \equiv 2 \sum_{i,j} S_{ij}^2 = \left(\frac{\partial \widetilde{u}}{\partial z}\right)^2 + \left(\frac{\partial \widetilde{v}}{\partial z}\right)^2 = \left|\frac{\partial U_h}{\partial z}\right|^2 \tag{2.30}$$

Using this result, the definitions of the gradient Richardson number $Ri_g = \frac{N^2}{S^2}$ and the turbulent Prandtl number $Pr_t = \frac{K_m}{K_h}$ provides the following result:

$$\phi_m = \frac{Pr_t}{Ri_g} \frac{z}{\Lambda} \tag{2.31}$$

In order to arrive at the length scale λ, it is easiest to derive the K_m which would obey the Monin-Obukhov theory and compare this with the actual formulation in the DALES code from Formula 2.12. Combining the definition of ϕ_m in Formula 2.29 (first equality) with the result of Formula 2.26 results in:

$$\phi_m = \frac{\kappa z}{\sqrt{K_m}} \left|\frac{\partial U_h}{\partial z}\right|^{1/2} \iff K_m = \frac{(\kappa z)^2}{\phi_m^2} \left|\frac{\partial U_h}{\partial z}\right| \tag{2.32}$$

If the result from Equation 2.31 is now combined with the *observed* functions for ϕ_m from Formula 2.22, it follows that

$$\phi_m = \frac{1}{1 - \alpha \frac{Ri_g}{Pr_t}} \tag{2.33}$$

Combining the last two results, K_m should obey the following relation to produce correct results in the stable atmospheric conditions:

$$K_m = (\kappa z)^2 (1 - \alpha \frac{Ri_g}{Pr_t})^2 \left|\frac{\partial U_h}{\partial z}\right| \tag{2.34}$$

In order to determine the correct length scale λ, now an expression is needed for the resulting K_m from DALES. If a steady state is assumed, together with a no transport of TKE Equation 2.18 can be rewritten to the well known subgrid model by Smagorinsky [14]:

$$0 = \frac{1}{2}\lambda(c_m S^2 - c_h N^2) - \frac{c_\epsilon e}{\lambda} = \frac{1}{2}\lambda S^2(c_m - c_h Ri_g) - \frac{c_\epsilon e}{\lambda} \tag{2.35}$$

Substituting the definitions of $c_h = c_{h,1}$, which corresponds with the suggestion of the previous section, this yields for the subgrid TKE e and subsequently for K_m:

$$e = \frac{c_m}{c_\epsilon}(1 - c_{h,1} Ri g_g)\lambda^2 S^2 \tag{2.36}$$

$$K_m \equiv c_m \sqrt{e}\lambda = \frac{c_m^{3/2}}{c_\epsilon^{1/2}}(1 - c_{h,1} Ri_g)^{1/2}\lambda^2 S \tag{2.37}$$

The constant $c_s \frac{c_m^{3/2}}{c_\epsilon^{1/2}}$ is the Smagorinsky constant. In order to let the DALES K_h obey the experimental Monin Obukhov results, λ must be chosen in such a way that Equations 2.37 equals 2.34. As $S = \left| \frac{\partial U_h}{\partial z} \right|$, and $Pr_t = 1$ for the stable case, the resulting λ equals:

$$\lambda_{MO} = \frac{\kappa z}{c_s^2} \frac{1 - \alpha Ri_g}{\left(1 - c_{h,1} Ri_g \right)^{1/4}} \tag{2.38}$$

It is useful to look graphically at this result. In Figure 2.3a is the resulting λ_{MO} plotted for several values of Ri_g, and in Figure 2.3b is the λ_{MO}/z plotted versus Richardson. Usually $\lambda = \Delta$ is chosen as length scale. If then, at a certain height, $\Delta > \lambda_{MO}$, this will result in too much eddy diffusion, as $K_{m,h}$ scales with Δ. From Figure 2.3b, the dashed line, can be deduced that this results in to much mixing for $z < \Delta/2$, regardless of the Richardson number. At larger heights, for $z = \Delta$ for instance, depending on the Richardson number there can still be too much mixing. When using anisotropic grids, this poses a problem. Results will be presented for a run with $\Delta x = \Delta y = 200$ and $\Delta z = 6.25$, yielding $\Delta = 60$ m. For this run, there will be too much mixing up to $30 m$, and even higher depending on the Richardson number. The next section will show that this is indeed the case.
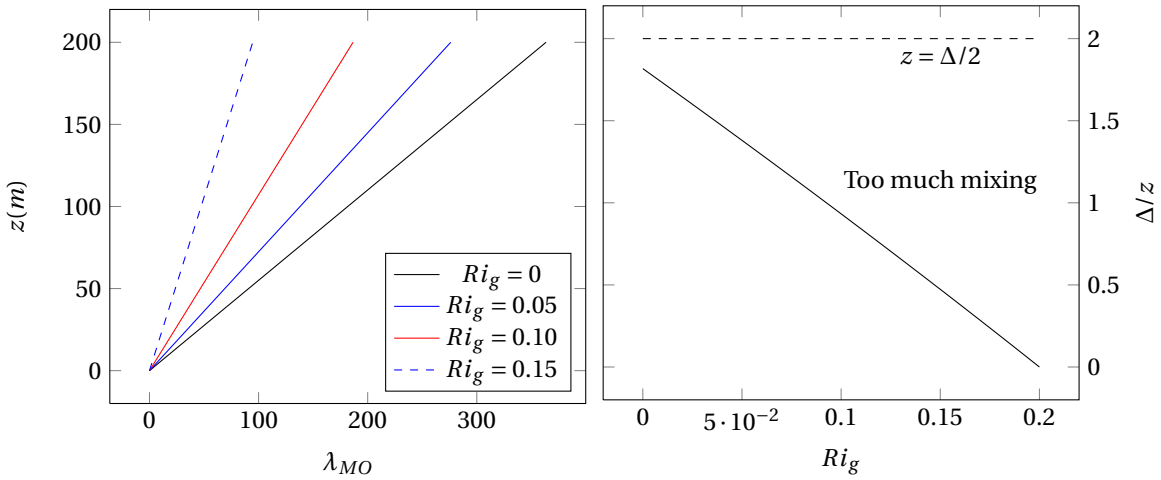
(a) The length scale λ_{MO} versus the z.

(b) The dimensionless length λ_{MO}/z versus Ri_g.

Figure 2.3: Graphical representation of the λ_{MO} length scale.

3

THE GABLS CASE

In order to evaluate the output of DALES, the GABLS case is used. This is a case based on Arctic observations by Kosovic and Curry [15] of the stable boundary layer, used in an intercomparison study by Beare *et al.* [1] of LES models as a part of the GEWEX Atmospheric Boundary Layer Study (GABLS).

(a) Surface wind profile   (b) θ_v profile
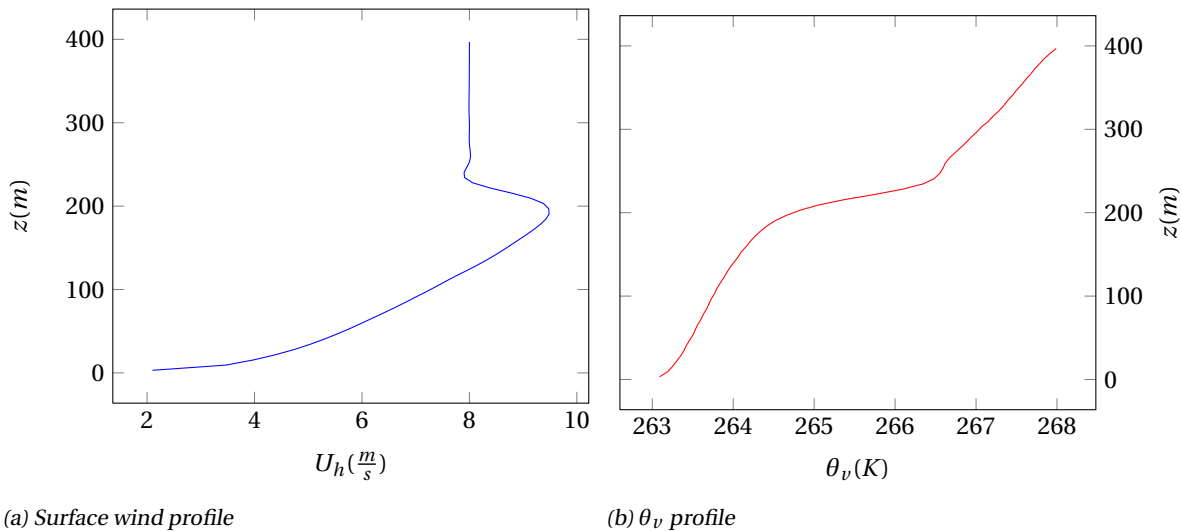
Figure 3.1: GABLS case profiles, quasi steady state after 9 hours . The profiles are slab averages over the complete horizontal domain, and are time averaged over 10 minutes.

The case is a simulation of an arctic night lasting 9 hours at a latitude 72 ° N. The initial wind profile is set equal to 8 m/s in the x-direction, the initial θ_v profile is constant 265 K up to 100 m, above it has a slight slope of 0.01 K/m. The initial surface temperature is 263.5 K, and decreases with 0.25 K/h. In Figure 3.1 are the resulting quasi steady state profiles after 9 hours from a high resolution DALES run ($\Delta x = 3.125 m$). These results are in agreement with the various results of LES models which participated in the inter comparison study by Beare *et al.* [1] and will therefore be used as reference, indicated by *high resolution run or Hres DALES*. The plots are averaged over 10 minutes and the horizontal domain of 400 × 400 m^2. Around the height of 200 m, a *nocturnal jet* is formed: a local maximum in the geostrophic wind. This happens at the location where $\frac{\partial \theta_v}{\partial z}$ is at its maximum. This height is also called the *boundary layer height* or *inversion*.

4

RESULTS OF DALES

Although the previous chapter shows that the high resolution version of DALES yields results for the stable GABLS case which agree with other LES models, these results depend on the horizontal resolution. As an illustration, the resulting horizontal wind profiles are plotted for 7 DALES runs in Figure 4.1a of the GABLS case. In each run, the total number of grid cells is 64^3, but the total horizontal domain is doubled between runs. Effectively, the horizontal grid cell size is therefore doubled each new run. All simulation are performed on the *Cirrus* cluster of the TU Delft, using 8 processor cores. Always 64^3 grid points were used, except [1] when the vertical grid size Δz was changed in Section 4.2. In order to give exact information on which options of DALES were used, a typical inputfile (NAMoptions) is included in the Appendix C. All the results presented are averaged of the horizontal domain and a time period of 10 minutes, and consist of the last 10 minutes of the GABLS simulation.
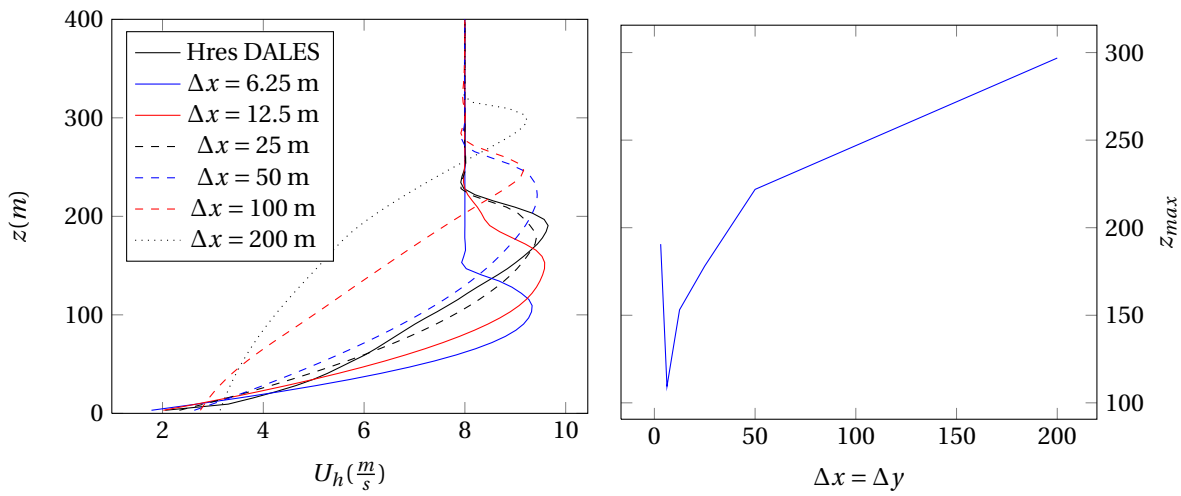
(a) Surface wind velocity for several horizontal grid sizes   *(b) Height of the nocturnal jet versus the horizontal grid size*

Figure 4.1: DALES results for the stable boundary layer. Note that the Hres DALES solution has a horizontal grid spacing of 3.125 m.

Figure 4.1a shows that the results of the DALES code for this stable case is very dependent on the horizontal grid resolution. Figure 4.1b shows how the height of the *nocturnal jet* depends on the horizontal grid size. Why do the results of DALES in the stable case depend so much upon the horizontal grid resolution? In Figure 4.2 the TKE profiles are plotted for the high resolution situation ($\Delta x = \Delta y = 3.125$m) and for the run with the lowest resolution ($\Delta x = \Delta y = 200$ m). The TKE is divided in resolved, subgrid and total, with the

---

[1] In the final week for the deadline of this thesis, a numerical error was found in the boundary layer conditions of the original DALES code. The four runs with $\Delta x = 6.25$m - $\Delta x = 50$m were redone with an improved version of the code. More information is in Appendix D

following definitions:

$$TKE_{subgrid} = \sum_i \langle \widetilde{u_i u_i} - \widetilde{u_i}\widetilde{u_i} \rangle \equiv e$$

$$TKE_{resolved} = \sum_i \langle (\widetilde{u_i} - \langle \widetilde{u_i} \rangle)(\widetilde{u_i} - \langle \widetilde{u_i} \rangle) \rangle$$

$$TKE_{total} = TKE_{subgrid} + TKE_{resolved}$$

Two big differences are visible between the TKE profiles. First, the total TKE in the $\Delta x = 200$ m run differs two orders of magnitude from the high resolution run. Apparently, the TKE scales with the horizontal grid size for the stable case. Secondly, in the run with $\Delta x = 200$ m the TKE consists completely of subgrid TKE, while the resolved TKE is dominant in the high resolution run. From the complete results of the other runs, Appendix F.1, all runs with $\Delta x \geq 6.25$ m are dominated by the subgrid.

(a) Hres DALES, $\Delta x = 3.125$ m   (b) $\Delta x = 200$ m
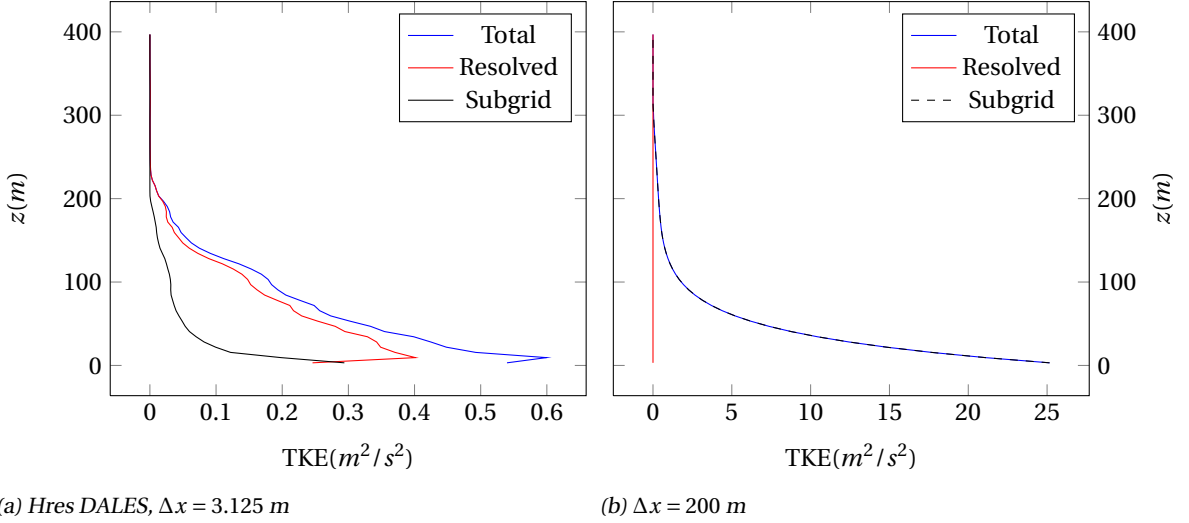
Figure 4.2: Vertical distribution of turbulent kinetic energy for two DALES simulations of the GABLS case

4.0.3. RELATION HORIZONTAL GRID SIZE AND SUBGRID TKE

Can these difference be understood from looking at the formulation of the DALES equations? For the subgrid dominated case, results show that transport can be neglected and the results appear to be steady state, horizontally homogeneous solutions with $\widetilde{w} = 0$ for the subgrid TKE. With these simplifications, Equation 2.18 reduces to:

$$0 = \frac{1}{2e^{1/2}}\left(-K_h N^2 + K_m S^2 - \frac{c_\epsilon e^{3/2}}{\lambda}\right) \tag{4.1}$$

It is now important to remember that both c_h and c_ϵ also depend on the grid size because of a term λ/Δ. For the length scale λ are two possibilities in the DALES code: $\lambda = \Delta$ or $\lambda = \min(\Delta, c_n \sqrt{e}/N)$.

Very stable conditions: $\lambda = c_n \frac{\sqrt{e}}{N}$ By implementing the definition of λ and $K_{m,h}$ the Expression 4.1 can be written as:

$$0 = -\left(c_{h,1} + c_{h,2}\frac{c_n\sqrt{e}}{N\Delta}\right)c_m c_n eN + c_m c_n e\frac{S^2}{N} - \left(c_{\epsilon,1} + c_{\epsilon,2}\frac{c_n\sqrt{e}}{N\Delta}\right)\frac{eN}{c_n} \tag{4.2}$$

This equation can be simplified by dividing by $c_n c_m Ne$, and using that $Ri_g = N^2/S^2$:

$$0 = -\left(c_{h,1} + c_{h,2}\frac{c_n\sqrt{e}}{N\Delta}\right) + \frac{1}{Ri_g} - \left(c_{\epsilon,1} + c_{\epsilon,2}\frac{c_n\sqrt{e}}{N\Delta}\right)\frac{1}{c_m c_n^2} \tag{4.3}$$

Solving this equation for e gives:

$$e = \Delta^2 Ri_g S^2 \left(\frac{\frac{c_m c_n}{Ri_g} - c_{h,1} c_m c_n - \frac{c_{\epsilon,1}}{c_n}}{c_{h,2} c_m c_n^2 + c_{\epsilon,2}} \right)^2 \tag{4.4}$$

It is clear from this equation, that when $\lambda = c_n e / N < \Delta$, the resulting steady state subgrid TKE scales with Δ^2, given a a certain S^2 and Ri_g. This is indeed what is found in the qualitatively simulations: higher subgrid TKE if Δ is larger.

Moderate stable conditions: $\lambda = \Delta$ Also for moderate stable conditions, when $\lambda = \Delta > c_n e / N$, this derivation can be done. Rewriting Equation 4.1 and substituting the definitions for $K_{m,h}$ from Formula 2.12 and 2.13 and $\lambda = \Delta$ and solving for e yields:

$$e = \frac{\Delta^2}{2c_\epsilon} \left(-c_h N^2 + c_m S^2 \right) \tag{4.5}$$

As c_ϵ and c_h do not depend on Δ anymore, because of the term λ / Δ in Equations 2.17 and 2.16. It is clear that also in this case the subgrid TKE grows with the Δ^2.

This explains the bigger sub grid TKE, but also the changing profiles: because of the dominance of the subgrid, the $\frac{\partial \tau_{ij}}{\partial x_i}$ term is the most important term in the LES equation for momentum. As the K_m is big compared to the high resolution case, the U_h profiles will be less steep and therefore *apparently* the nocturnal jet will also be located higher in the atmosphere. This assumption will be verified in the next Section 4.0.4.

This result coincides with the theoretical derivation of the λ_{MO} in Section 2.2.2. Here it was indicated that the length scale $\lambda = \Delta$ results in a $K_{m,h}$ which is too big at the lower levels of the atmosphere. This results again in two much mixing. Furthermore, from Figure 2.3a[2] can be seen that, given a certain Richardson number, this effect is stronger for larger Δ. Figure 4.1a shows that the slope of U_h is indeed larger in the lower level for bigger Δx, if the simulation is subgrid dominated.

4.0.4. NOCTURNAL JET HEIGHT AND MONIN OBUKHOV THEORY

A second important aspect of the resulting profiles is whether they obey the Monin-Obukhov similarity theory. For the two extreme grid sizes, the results are plotted in Figure 4.3. The high resolution results seem to follow the Monin-Obukhov, although both ϕ_m and ϕ_h are slightly less steep than the required $1 + 5z/\Lambda$ and $Pr = \phi_m / \phi_h \neq 1$. The results of the low resolution case do not follow the Monin Obukhov theory: $Pr \gg 1$, and both similarity functions have a slope which is lower than required. The first observation can be understood from the derivation in Section 2.2.1, which resulted in:

$$\frac{\phi_h}{\phi_m} = Pr_t = \frac{1}{c_{h,1} + c_{h,2} \frac{\lambda}{\Delta}} \tag{4.6}$$

As $\lambda = \Delta$ in this case, the and $c_{h,1} = 1$, $c_{h,2} = 2$ ([3]), it should follow from DALES results that $\frac{\phi_h}{\phi_m} = \frac{1}{3}$. Figure 4.3 shows that this is exactly what happens when the DALES solution becomes subgrid dominated, here shown for $\Delta x = 200$ m.

In the previous section the link was described between the subgrid TKE and the K_h, resulting in a lower $\frac{\partial U_h}{\partial z}$. Beside a wrong turbulent Prandtl number, Figure 4.3 shows also that the ϕ_m and ϕ_h are also less steep for large Δx. This is also the case for other simulations, these plots are in Appendix F.1. Using the derivations from Section 2.2.1 it is possible to test what the influence is of the slope in the Monin Obukhov similarity function to the height of the nocturnal jet, by using a simple 1D model. The exact derivation can be found in

---

[2]The Richardson number are plotted as reference in Figure 4.5.
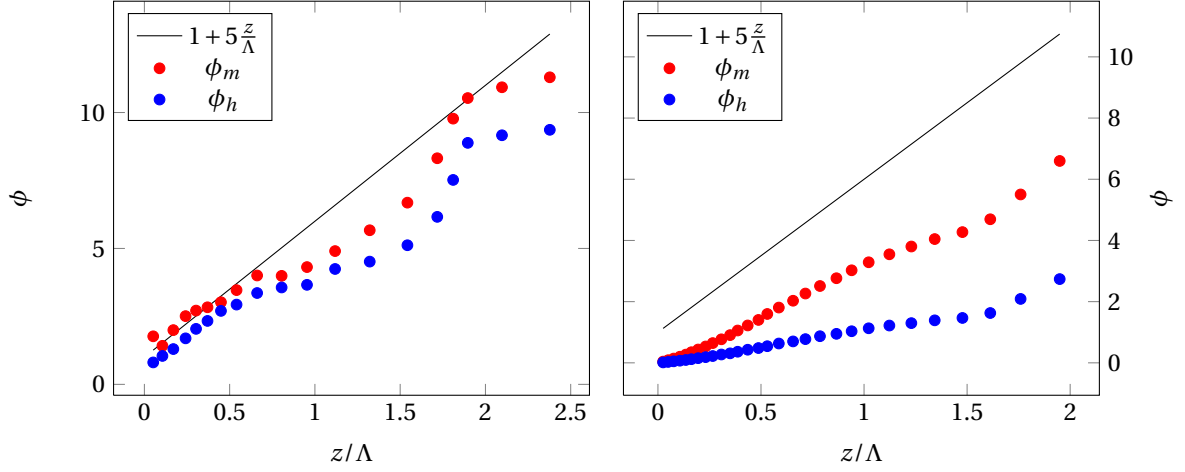
(a) Hres DALES, $\Delta x = 3.125\ m$ *(b) $\Delta x = 200\ m$*

Figure 4.3: Monin-Obukhov similarity functions for the DALES results of the GABLS case

Appendix B, the model consists of numerical integrating the simplified LES equations given by:

$$\frac{\partial u}{\partial t} = fv - fv_{geo} - \frac{\partial}{\partial w}\left(-K_m \frac{\partial u}{\partial z}\right)$$

$$\frac{\partial v}{\partial t} = -fu + fu_{geo} - \frac{\partial}{\partial w}\left(-K_m \frac{\partial v}{\partial z}\right) \tag{4.7}$$

$$\frac{\partial \theta_v}{\partial t} = -\frac{\partial}{\partial z}\left(-K_h \frac{\partial \theta_v}{\partial z}\right)$$

In this equation, f is the Coriolis parameter (Appendix B) and $K_{m,h}$ are given by 2.34, such that the wind and θ_v profiles will follow the Monin Obukhov theory. This model was numerically integrated using the exact same boundary conditions as in the LES simulations, given in Chapter 3. How does this simple model compare to the high resolution DALES results?
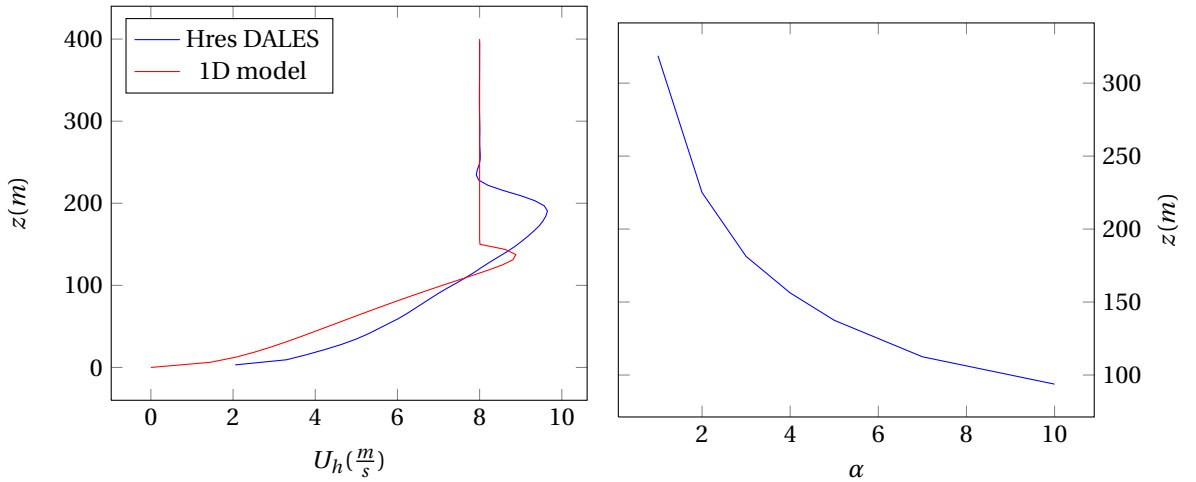
(a) Horizontal wind velocity   *(b) Height of the nocturnal jet versus slope α*

Figure 4.4: Results of the simple 1D model

From Figure 4.4a it is clear that the simple model captures some characteristics of the high resolution DALES solution, but the nocturnal jet converges at a different height. Nonetheless, this model could help explaining how the slope of $\phi_{m,h}$ results in a different height for the nocturnal jet. For this, the simple 1D model was run

for several values of α, in Formula 2.22. This results in different values for K_m, h, and might thus influence the height of the nocturnal jet. Figure 4.4b shows that this is indeed the case. For a less steep slope of the similarity functions, therefore a lower α, the nocturnal jet converges at a higher level in the atmosphere.

However, this does not yet completely explain the behaviour of the DALES solutions. In Appendix F.1 can be seen that the similarity functions of the runs with $\Delta x = 25, 50, 100$ are quite similar, although the nocturnal jet converges at different heights.

4.0.5. GRADIENT RICHARDSON NUMBERS

As reference are the Richardson numbers plotted for these cases in Figure 4.5, up till the height of the nocturnal jet, as the Ri_g is very unstable above this height. It is clear that only the resolved dominated high resolution run ($\Delta x = 3.125$m) differs from the others: it has bigger Ri_g numbers in the lower part of the atmosphere. The Richardson number of the other cases are very small in the lower part of the atmosphere.

This results does not agree with the simple 1D model from the previous section. It was argued there that a lower slope of the Monin Obukhov similarity functions α result in a higher nocturnal jet. This is indeed what happens in the LES results. However, the slope of the Monin Obukhov function can be written in terms of Ri_g, see Formula 2.31 from Chapter 2 given here for easy reference:

$$\phi_m = \frac{Pr_t}{Ri_g} \frac{z}{\Lambda}$$

According to this formula, a lower slope of ϕ_m should coincide with a higher Ri_g number: the results in Figure 4.5 show that this is not the case. This indicates that the 1D model from the previous section gives a valuable insight, but the complete explanation is more complicated.
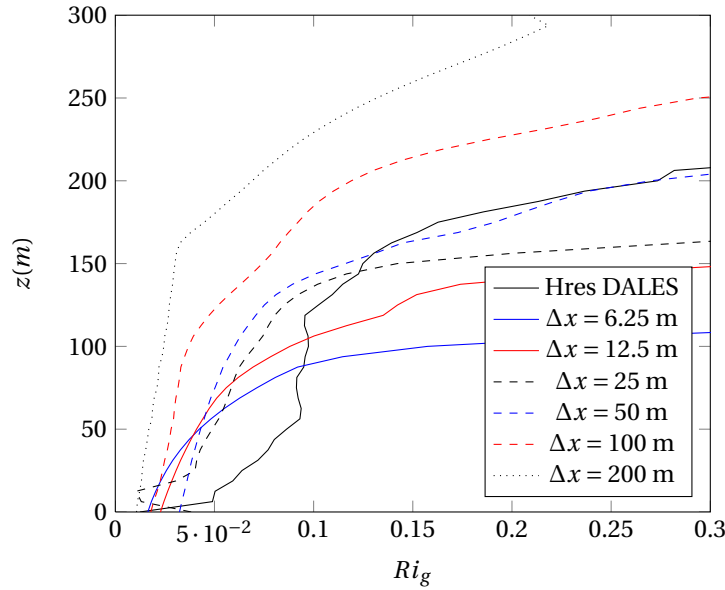
Figure 4.5: Gradient Richardson number in the GABLS case using DALES with different grid sizes. Agina, Hres DALES uses $\Delta x = 3.125$.

4.1. TURBULENT PRANDTL NUMBER $Pr_t = 1$

The previous section shows that, among other results, the turbulent Prandtl number $\frac{1}{3}$ instead of 1 due to the formulation of the constants c_h of formula 2.16. This formulation was introduced by Deardorff [8] to ensure a correct Pr_t number in situations with a small subgrid TKE. By removing the dependencies of Δ from c_h and c_ϵ, it is possible to test whether the Prandtl number converges now to the value of 1, as it should. The constants are now changed to:

$$c_h^* = c_{h,1} c_m$$
$$c_\epsilon^* = c_{\epsilon,1} + c_{\epsilon,2} \qquad\qquad (4.8)$$

In Figure 4.6 are the results of an experiment with this change in subgrid constants, compared to the high resolution reference and a run with the original DALES code with the same $\Delta x = 12.5$ m. Results with different Δx are presented in Appendix F.2. These results show that the strong dependency of the nocturnal jet of the grid size is still present, as was to be expected. From the similarity functions however, it is clear that the Prandtl number is now indeed 1, as $\phi_m \approx \phi_h$ for all simulations.

(a) U_h profiles   *(b) Similarity functions*
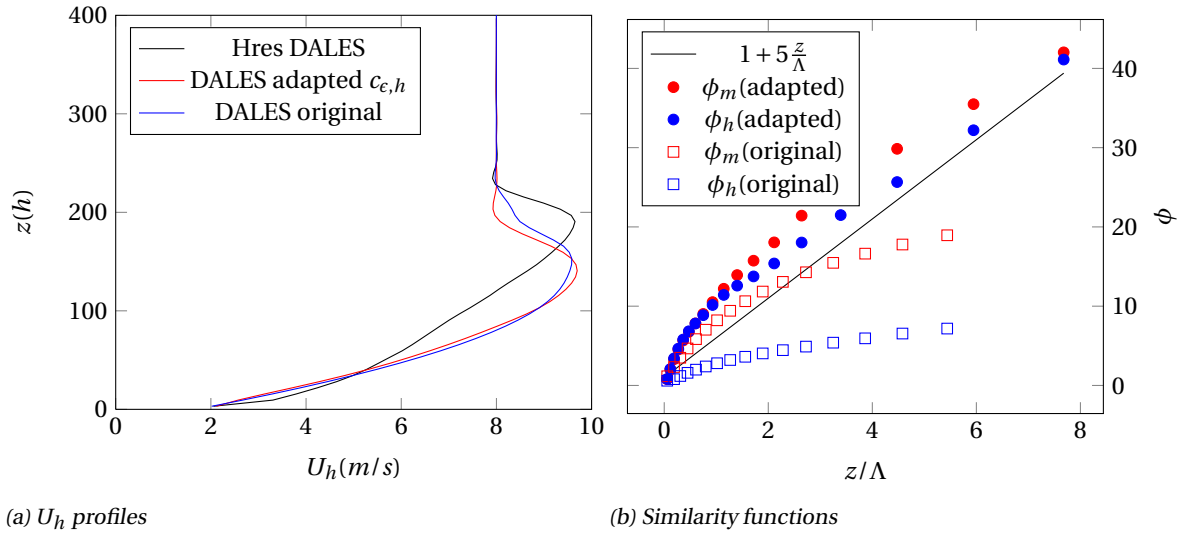
Figure 4.6: Results of the DALES run with adapted $c_{\epsilon,h}^*$ (Formulas 4.8) compared with the high resolution DALES result and a DALES run with the same $\Delta x = 12.5$ m.

4.2. ANISOTROPIC EDDY DIFFUSIVITIES

Part of the problems of the DALES results with changing grid sizes might be due to the changing aspect ratio of the grid boxes. In the experiments presented in Figure 4.1a the horizontal grid size is changed from 3.125 m up to 200 m, while the vertical grid size remains constant at 6.25 m. However, the diffusivities $K_{m,h}$ are based upon a mean $\Delta = (\Delta x \Delta y \Delta z)^{1/3}$, so also the vertical diffusivity changes when only the horizontal resolution is changed.

In order to verify whether the discrepancy between the Δx and Δz influences the solution, two extra series of experiments have been done with different values for Δz, while the total domain height remained 400 m. In order to compare them, the *aspect ratio* has been defined as:

$$r = \frac{\Delta x}{\Delta z} \qquad\qquad (4.9)$$

In Figure 4.7 is the height of the nocturnal jet plotted versus the aspect ratio, for several values of Δz and Δx.

From Figure 4.7 can be concluded that the part of the problem can be traced back to the aspect ratio $r \neq 1$, as for each of the series of simulations holds that the height of the nocturnal jet increases with the aspect ratio. However, this is only part of the solution. If different data points with the same aspect ratio are compared, for instance at $r = 4$, it is clear that the nocturnal jet height also increases with Δ.

A solution for part of the problem caused by the aspect ratio could be introducing an anisotropic $K_{m,h}$. This means that $K_{m,h}$ is different for the horizontal (x, y) and the vertical (z) direction. The method proposed by Khairoutdinov [16] has been followed in this thesis. By changing the definition of Δ to $\Delta = \Delta z$ in the LES code,
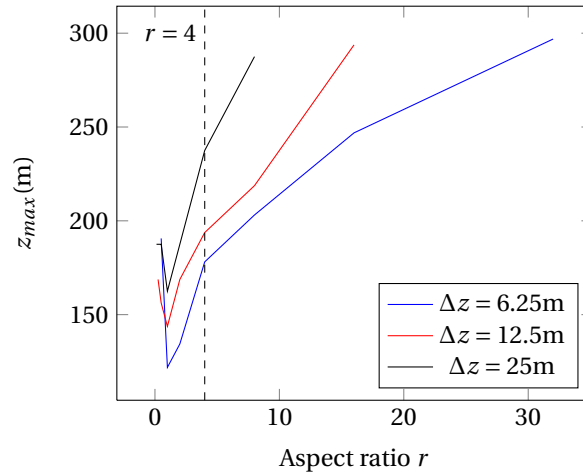
Figure 4.7: Height of the nocturnal jet versus the aspect ratio for three sets of DALES runs with different Δz

the vertical diffusion does not depend on the horizontal grid size any more. For the horizontal eddy diffusion, the terms K_h and K_m should then be multiplied with $\frac{\Delta x \Delta y}{(\Delta z)^2}$ to obtain the original definition.

Do this method help fixing part of the problems of the DALES code? In Figure 4.8 are the surface wind profiles of the high resolution DALES reference, the results of a run with the new anisotropic $K_{m,h}$ and the original DALES code, both with $\Delta x = 12.5$m. Also the Monin Obukhov similarity functions have been plotted. This experiment has been repeated for several values of Δx, elaborate results are in Appendix F.3.
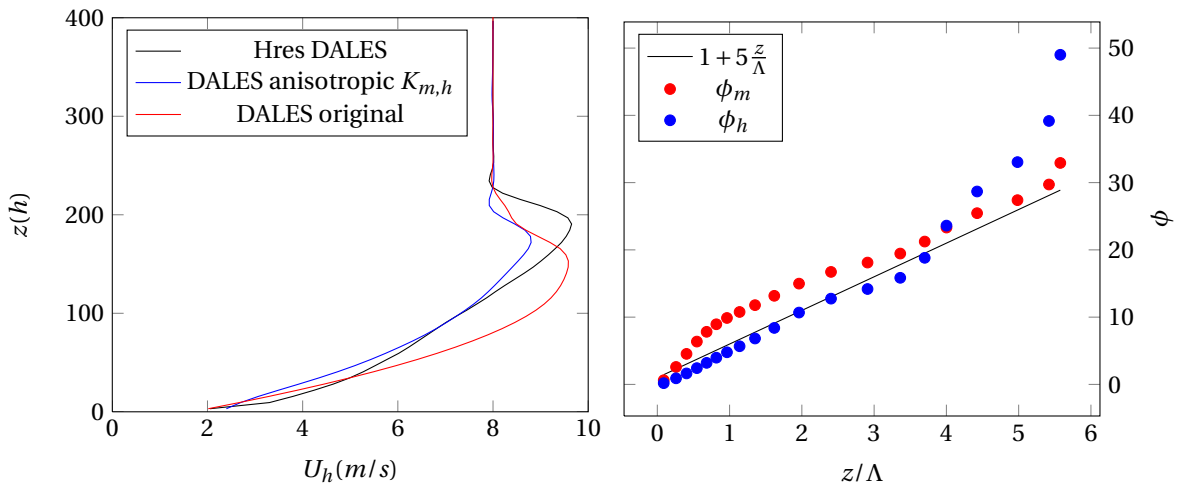
(a) Profiles

(b) Similarity functions for the DALES with anisotropic $K_{m,h}$.

Figure 4.8: Results of one experiment with anisotropic $K_{m,h}$. The runs with the adapted and original DALES code have been performed with $\Delta x = 12.5$.

The results in Figure 4.8 seem very good, as the U_h profile approaches the high resolution run much better than the original DALES code at the same resolution. Also the similarity functions follow the Monin-Obukhov theory very well. Unfortunately, this is not the case for the other experiments at different grid resolutions with this version of the DALES code, see Appendix F.3. For smaller Δx the profile is very similar to the runs with the original DALES code. This was to be expected, as the aspect ratio $r \approx 1$. For higher Δx, the code becomes unstable: above the nocturnal jet, a lot of resolved turbulence is generated, see Appendix F.3.

5

THE SULLIVAN MODEL

In the previous section the problems with the LES code used in DALES were extensively studied. It was shown that the for a subgrid dominated case, the subgrid TKE scaled with the grid size, yielding unreliable results. Moreover, the subgrid dominated solutions did not follow the Monin Obukhov similarity theory. Sullivan *et al.* [2] proposes an adaptation to the LES equation 2.3 and subgrid TKE equation 2.18 in order to overcome this problem and ensure at the same that the resulting profiles follow indeed the Monin-Obukhov similarity relation.

5.1. THE ORIGINAL IDEA

In order reduce the subgrid TKE production and ensure that the resulting U_h profile follows the Monin Obukhov theory, the following changes are made to respectively the subgrid TKE production term P_s from Equation 2.18 and the subgrid shear term τ_{ij} from 2.3:

$$P_s^{sul} = 2K_m\gamma(S_{ij} - \langle S_{ij}\rangle)(S_{ij} - \langle S_{ij}\rangle) = \gamma K_m(S')^2 \tag{5.1}$$

$$\tau_{ij}^{sul} = -2K_m\gamma S_{ij} - 2K_M\langle S_{ij}\rangle \tag{5.2}$$

The factor γ is given by:

$$\gamma = \frac{S'}{S' + \langle S\rangle} \tag{5.3}$$

In this equation, the terms S' and $\langle S\rangle$ are given by:

$$S' = \sqrt{\sum_{i,j} 2\langle(S_{ij} - \langle S_{ij}\rangle)(S_{ij} - \langle S_{ij}\rangle)\rangle}$$

$$\langle S\rangle = \sqrt{\sum_{i,j} 2\langle S_{ij}\rangle\langle S_{ij}\rangle}$$

The changes Sullivan *et al.* [2] introduces in these formulas consist of three parts:

- In order to reduce the production of subgrid TKE, the production term by shear P_s is adapted by subtracting the mean shear. In this way, only variations in the shear will induce subgrid TKE.

- The second change to the original LES model is adding an extra mean shear term to the LES equations for u_i, 2.3, resulting in 5.2. By choosing the *mean strain eddy diffusivity K_M* correctly, it is possible to make sure that the mean wind follows to Monin-Obukhov similarity theory.

- The final modification is the introduction of a anisotropy factor γ. Both the new subgrid TKE production term P_s^{sul} and the original subgrid shear term τ_{ij} are multiplied by γ defined in 5.3, resulting in 5.1 5.2. The γ factor consist of two terms: $\langle S\rangle$ is a measure for the mean strain, while S' is a measure for the fluctuations in the resolved strain. When the variations in the strain S' are small, $\gamma \approx 0$. In this case

there will be less subgrid shear in the LES equations, and the production of subgrid TKE will be smaller. Both effects should amplify the production of resolved motions.

The implementation of γ and P_s^{sul} is relatively straightforward, the only remaining question is how to choose a K_M, which only depends on z and can of course change over time. The *mean strain viscosity K_M* is defined in Sullivan *et al.* [2] using Prandtl's mixing length concept:

$$K_M = (l^*)^2 \langle S \rangle \tag{5.4}$$

The mixing length l^* is chosen in such a way, that the Monin-Obukhov theory holds at $z = \Delta z$, the first grid level were $w \neq 0$, see Figure 2.2. The length scale l^* is constant for the whole space, therefore independent of (x, y, z). It is assumed that the momentum flux, or surface stress, stay constant between $z = 0$ and $z = \Delta z$. The surface stress at $z = 0$ is then required to be equal to the sum of the resolved and subgrid momentum fluxes at $z = \Delta z$:

$$u_*^2|_{z=0} = \sqrt{\langle \tau_{uw} \rangle^2 + \langle \tau_{vw} \rangle^2}|_{\Delta z} + \sqrt{\langle \widetilde{u}\widetilde{w} \rangle^2 + \langle \widetilde{v}\widetilde{w} \rangle^2}|_{\Delta z} \tag{5.5}$$

An expression for $\langle \tau_{ij} \rangle$ can be found by taking the slab average of equation 5.2 while assuming $\langle K_m S_{ij} \rangle = \langle K_m \rangle \langle S_{ij} \rangle$. This corresponds to ignoring contributions of the fluctuating strain. This results in the following expression for the slab averaged subgrid shear:

$$\langle \tau_{ij} \rangle = -2(\langle K_m \gamma \rangle + K_M) \langle S_{ij} \rangle \tag{5.6}$$

As $\langle \widetilde{w} \rangle = 0$ per definition, $\langle S_{uw} \rangle = \frac{1}{2} \frac{\partial \langle \widetilde{u} \rangle}{\partial z}$. The same result applies of course to $\langle S_{vw} \rangle$. A second assumption is made regarding the average horizontal wind $U_h = \sqrt{\langle \widetilde{u} \rangle^2 + \langle \widetilde{v} \rangle^2}$ at $z = \Delta z$. Turning of the average horizontal wind is neglected between the surface and Δz, combined with cyclic boundary conditions this results in:

$$\sqrt{(2\langle S_{uw} \rangle)^2 + (2\langle S_{vw} \rangle)^2} = \sqrt{\left(\frac{\partial \langle \widetilde{u} \rangle}{\partial z}\right)^2 + \left(\frac{\partial \langle \widetilde{v} \rangle}{\partial z}\right)^2} \approx \frac{\partial U_h}{\partial z} \tag{5.7}$$

Now Equations 5.6 and 5.7 can be implemented in Equation 5.5, yielding:

$$-(\langle K_m \gamma \rangle + K_M) \frac{\partial U_h}{\partial z}|_{\Delta z} + \sqrt{\langle \widetilde{u}\widetilde{w} \rangle^2 + \langle \widetilde{v}\widetilde{w} \rangle^2}|_{\Delta z} = u_*^2 \tag{5.8}$$

The final step of the derivation is requiring that $\frac{\partial U_h}{\partial z}$ follows the Monin-Obukhov similarity function at $z = \Delta z$, the similarity function is given by:

$$\frac{\partial U_h}{\partial z} = \frac{u_* \phi_m}{\kappa z} \tag{5.9}$$

Substituting Equation 5.9 evaluated on $z = \Delta z$ in Equation 5.8, the mean strain viscosity $K_M|_{\Delta z}$ is obtained:

$$K_M|_{\Delta z} = \frac{u_* \kappa \Delta z}{\phi_m(\Delta z)} - \langle K_m \gamma \rangle - \frac{\kappa \Delta z}{u_* \phi_m(\Delta z)} [\langle uw \rangle^2 + \langle vw \rangle^2]^{1/2} \tag{5.10}$$

From this relation the mixing length l^* can be easily deduced, by multiplying with the Monin-Obukhov similarity function from Formula 5.9 and rewriting it in the following manner:

$$K_M|_{\Delta z} = \underbrace{\left(\frac{(\kappa \Delta z)^2}{(\phi_m(\Delta z))^2} - \frac{\kappa \Delta z}{u_* \phi_m(\Delta z)} \langle K_m \gamma \rangle - \frac{(\kappa \Delta z)^2}{(u_* \phi_m(\Delta z))^2} [\langle uw \rangle^2 + \langle vw \rangle^2]^{1/2} \right)}_{(l^*)^2} \underbrace{\left(\frac{\partial U_h}{\partial z}|_{\Delta z} \right)}_{\langle S \rangle} \tag{5.11}$$

Since l^* is constant in space, is has now been determined in such a way that the Monin-Obukhov relation is obeyed at $z = \Delta z$. The values of K_M at all heights z can now be easily determined using Formula 5.4. In order to prevent forcing of the Monin Obukhov theory by the Sullivan model at the top of the boundary level, the Sullivan model was only used up to $z = z_i/2$, where the boundary layer height z_i was defined as:

$$z_i = \min(|\frac{\partial \langle \widetilde{\theta_v} \rangle}{\partial z}|) \tag{5.12}$$

Above this height, K_M and γ were set to $K_M = 0$ and $\gamma = 1$, which reduces the Sullivan model to the original DALES code.

5.2. SULLIVAN MODEL WITH $\gamma = 1$

From the description of Sullivan's model, it is clear that it seems to consist of two parts which try to reach the same goal. On one hand the factor γ is used to decrease the TKE production by shear and the subgrid shear effect on the resolved motions. On the other hand do the adapted subgrid TKE production term and the added extra mean strain term in the LES equation also decrease subgrid production and stimulate the resolved motions. In order to find out whether both parts are both necessary to obtain a good result, Sullivan's model is also tested with $\gamma = 1$ everywhere. In this way, the whole idea of an extra factor is basically removed from the model, yielding a simpler and computational less expensive method.

5.3. SIMPLER FORMULATION OF K_M

A second adaptation to the original model is tested, which involves a much simpler K_M than Sullivan actually proposed. It is useful to look again at the formulation of the l_*^2 from Formula 5.11, the length scale associated with the mean eddy diffusivity.

$$(l_*)^2 = \frac{(\kappa \Delta z)^2}{(\phi_m(\Delta z))^2} - \frac{\kappa \Delta z}{u_* \phi_m(\Delta z)} \langle K_m \gamma \rangle - \frac{(\kappa \Delta z)^2}{(u_* \phi_m(\Delta z))^2} [\langle uw \rangle^2 + \langle vw \rangle^2]^{1/2} \tag{5.13}$$

The second term on the right hand side is probably very small compared to the first term, as at $z = \Delta z$ mean shear is very dominant, therefore γ is small. Also the third term might be neglected: the resolved shear at the bottom of the atmosphere is small compared to the sub grid shear, as there is little resolved motion. This yield a much simpler length scale and therefore simpler $K_M = (l_*)^2 \langle S \rangle$:

$$(l_*)^2 = \frac{(\kappa \Delta z)^2}{(\phi_m(\Delta z))^2} \tag{5.14}$$

This length scale equals the preliminary result of Equation 2.32, which presents the definition of K_m if the Monin Obukhov theory is exactly met. This is to be expected, as the subgrid and resolved contributions are neglected in this simplification: the only term which can censure the Monin Obukhov theory is now the mean shear, which should therefore incorporate the Monin Obukhov obeying K_M.

5.4. ADAPTATION FOR BUOYANCY FLUXES

For the buoyancy fluxes, the same approach can be taken as for the momentum fluxes to promote resolved motions and diminish the effect of the sub grid. The equation for θ_v in DALES is given by Formula 2.4. To modify this equation according to the method of Sullivan, the parameterization of the subgrid buoyancy flux is changed both in the subgrid TKE equation and in the θ_v equation. In the subgrid TKE equation, similar to Equation 5.1, the buoyancy term becomes:

$$\widetilde{w'\theta_v'} = -K_h \left(\frac{\partial \widetilde{\theta_v}}{\partial z} - \langle \frac{\partial \widetilde{\theta_v}}{\partial z} \rangle \right) \tag{5.15}$$

And in the θ_v equation (compare with 5.2) it is changed to:

$$\widetilde{w'\theta_v'} = -K_h \frac{\partial \widetilde{\theta_v}}{\partial z} - K_H \langle \frac{\partial \widetilde{\theta_v}}{\partial z} \rangle \tag{5.16}$$

The diffusivity K_H should now be chosen in such a way, that the Monin-Obukhov similarity function for heat transport is obeyed, which is:

$$\phi_h = -\frac{\kappa z u_*}{\langle \widetilde{w'\theta_v'} \rangle|_{z=0}} \frac{\langle \partial \widetilde{\theta_v} \rangle}{\partial z} \tag{5.17}$$

As the Monin-Obukhov relation is already met on the first full level $z = \Delta z/2$ because of the boundary conditions, K_H is chosen such that it meets the criteria at $z = \Delta z$, the second full level. $\langle w \rangle = 0$, and if the turbulent

heat flux is assumed constant below Δz, then:

$$\langle \widetilde{w'\theta'_v} \rangle|_{z=0} = \langle \widetilde{w'\theta'_v} \rangle|_{z=\Delta z} + \langle \widetilde{w}\widetilde{\theta_v} \rangle|_{z=\Delta z} \tag{5.18}$$

Combining this equation with the new parameterization in Formula 5.16, yields:

$$\langle \widetilde{w'\theta'_v} \rangle|_{z=0} = \langle -K_h \frac{\partial \widetilde{\theta_v}}{\partial z} - K_H^* \langle \frac{\partial \widetilde{\theta_v}}{\partial z} \rangle \rangle|_{z=\Delta z} + \langle \widetilde{w}\widetilde{\theta_v} \rangle|_{z=\Delta z}$$

$$\approx -(\langle K_h \rangle + K_H^*)\langle \frac{\partial \widetilde{\theta_v}}{\partial z} \rangle + \langle \widetilde{w}\widetilde{\theta_v} \rangle|_{z=\Delta z}$$

In the second step it is assumed that K_h and $\frac{\partial \widetilde{\theta_v}}{\partial z}$ are not correlated. As slab-averaging and taking the derivative can be interchanged, $\langle \frac{\partial \widetilde{\theta_v}}{\partial z} \rangle = \frac{\partial \langle \widetilde{\theta_v} \rangle}{\partial z}$, and the Monin-Obukhov relation can be used:

$$\langle \widetilde{w'\theta'_v} \rangle|_{z=0} = -(\langle K_h \rangle + K_H^*)\frac{\phi_h \langle \widetilde{w'\theta'_v} \rangle|_{z=0}}{\kappa \Delta z u_*} + \langle \widetilde{w}\widetilde{\theta_v} \rangle|_{z=\Delta z}$$

$$K_H|_{\Delta_z} = \frac{\kappa \Delta z u_*}{\phi_h(\Delta_z)} - \langle K_h \rangle - \frac{\kappa \Delta z u_*}{\phi_h(\Delta z)\langle \widetilde{w'\theta'_v} \rangle|_{z=0}}\langle \widetilde{w}\widetilde{\theta_v} \rangle|_{z=\Delta z}$$

For the other heights, an adaption of the Prandtl mixing length concept is used. It is assumed that:

$$K_H = (l_H^*)^2 \langle S \rangle \tag{5.19}$$

Using the Monin-Obukhov function for momentum (Formula 5.9) and the fact that $\phi_m = \phi_h$, the K_H at level $z = \Delta z$ can be written as:

$$K_H|_{\Delta_z} = \underbrace{\left(\frac{(\kappa \Delta z)^2}{(\phi_h(\Delta_z))^2} - \frac{\kappa \Delta z}{u_* \phi_h(\Delta z)}\langle K_h \rangle - \frac{(\kappa \Delta z)^2}{(\phi_h(\Delta z))^2 \langle \widetilde{w'\theta'_v} \rangle|_{z=0}}\langle \widetilde{w}\widetilde{\theta_v} \rangle|_{z=\Delta z} \right)}_{(l_H^*)^2} \underbrace{\left(\frac{\partial U_h}{\partial z} \right)|_{\Delta z}}_{\langle S \rangle} \tag{5.20}$$

As the mixing length is now fixed, Equation 5.19 can now be used to easily calculate the K_H at all heights.

5.5. SUMMARY ON THE DIFFERENT SULLIVAN MODELS

To help read the Results section and make quick reference possible, this section provides the most important formulas, as well as a short summary on the different models. The LES equations in DALES are given by:

$$\frac{\partial \widetilde{u_i}}{\partial t} + \frac{\partial \widetilde{u_j}\widetilde{u_i}}{\partial x_j} = -\frac{\partial \widetilde{\pi}}{\partial x_i} + \frac{\widetilde{\theta_v}}{\theta_0}g\delta_{i3} - \frac{\partial \tau_{ij}}{\partial x_j} + F_i$$

$$\frac{\partial \widetilde{\theta_v}}{\partial t} + \frac{\partial \widetilde{u_j}\widetilde{\theta_v}}{\partial x_j} = -\frac{\partial \widetilde{u'_j \theta'_v}}{\partial x_j}$$

The equation for the subgrid TKE is given by:

$$\frac{\partial e^{1/2}}{\partial t} + \widetilde{u_j}\frac{\partial e^{1/2}}{\partial x_j} = \frac{1}{2e^{1/2}}\left(\frac{g}{\theta_0}\widetilde{w'\theta'_v} - \tau_{ij}\frac{\partial \widetilde{u_i}}{\partial x_j} \right) + K_m \frac{\partial e^{1/2}}{\partial x_j} - \frac{c_\epsilon e}{2\lambda}$$

The main difference between the original DALES formulation and the several alternatives, is the parametrization of the subgrid fluxes τ_{ij} and $\widetilde{w'\theta'_v}$. In Table 5.1 are the different parametrizations listed.

Table 5.1: Overview of the different models tested in this thesis.

Model	LES equation		subgrid TKE equation		K_M	Details
	τ_{ij}	$\widetilde{w'\theta'_v}$	τ_{ij}	$\widetilde{w'\theta'_v}$		
DALES	$-2K_m S_{ij}$	$-K_h\frac{\partial\widetilde{\theta_v}}{\partial z}$	$-2K_m S_{ij}$	$-K_h\frac{\partial\widetilde{\theta_v}}{\partial z}$	not used	Section 2.1
Sullivan	$-2\gamma K_m S_{ij}-2K_M\langle S_{ij}\rangle$	$-K_h\frac{\partial\widetilde{\theta_v}}{\partial z}$	$-2\gamma K_m\left(S_{ij}-\langle S_{ij}\rangle\right)$	$-K_h\frac{\partial\widetilde{\theta_v}}{\partial z}$	Formula 5.11	Section 5.1
Sullivan ($\gamma=1$)	$-2K_m S_{ij}-2K_M\langle S_{ij}\rangle$	$-K_h\frac{\partial\widetilde{\theta_v}}{\partial z}$	$-2K_m\left(S_{ij}-\langle S_{ij}\rangle\right)$	$-K_h\frac{\partial\widetilde{\theta_v}}{\partial z}$	Formula 5.11 with $\gamma=1$	Section 5.2
Sullivan (simplified K_M)	$-2\gamma K_m S_{ij}-2K_M\langle S_{ij}\rangle$	$-K_h\frac{\partial\widetilde{\theta_v}}{\partial z}$	$-2\gamma K_m\left(S_{ij}-\langle S_{ij}\rangle\right)$	$-K_h\frac{\partial\widetilde{\theta_v}}{\partial z}$	$\frac{(\kappa\Delta z)^2}{(\phi_m(\Delta z))^2}\langle S\rangle$	Section 5.3
Sullivan(buoyancy)	$-2\gamma K_m S_{ij}-2K_M\langle S_{ij}\rangle$	$-K_h\frac{\partial\widetilde{\theta_v}}{\partial z}-K_H\langle\frac{\partial\widetilde{\theta_v}}{\partial z}\rangle$	$-2\gamma K_m\left(S_{ij}-\langle S_{ij}\rangle\right)$	$-K_h\left(\frac{\partial\widetilde{\theta_v}}{\partial z}-\langle\frac{\partial\widetilde{\theta_v}}{\partial z}\rangle\right)$	Formula 5.11	Section 5.4

6

RESULTS OF THE SULLIVAN MODEL

In this section the results of the model proposed by Sullivan *et al.* [2] will be presented. The details of the models can be found in Section 5, the important formulas are listed in Section 5.5, together with an overview of all the models which were tested. In order to visualize whether the models have the same resulting profiles for the GABLS case as the high resolution DALES solution, the 4 different models are plotted together with the high resolution solution in Figure 6.1. In order to compare the different models with each other, also the resolved TKE has been plotted, defined as:

$$TKE_{resolved} = \sum_i \langle (\widetilde{u_i} - \langle \widetilde{u_i} \rangle)(\widetilde{u_i} - \langle \widetilde{u_i} \rangle) \rangle \tag{6.1}$$

(a) U_h profiles

(b) Resolved TKE of the U_h profiles
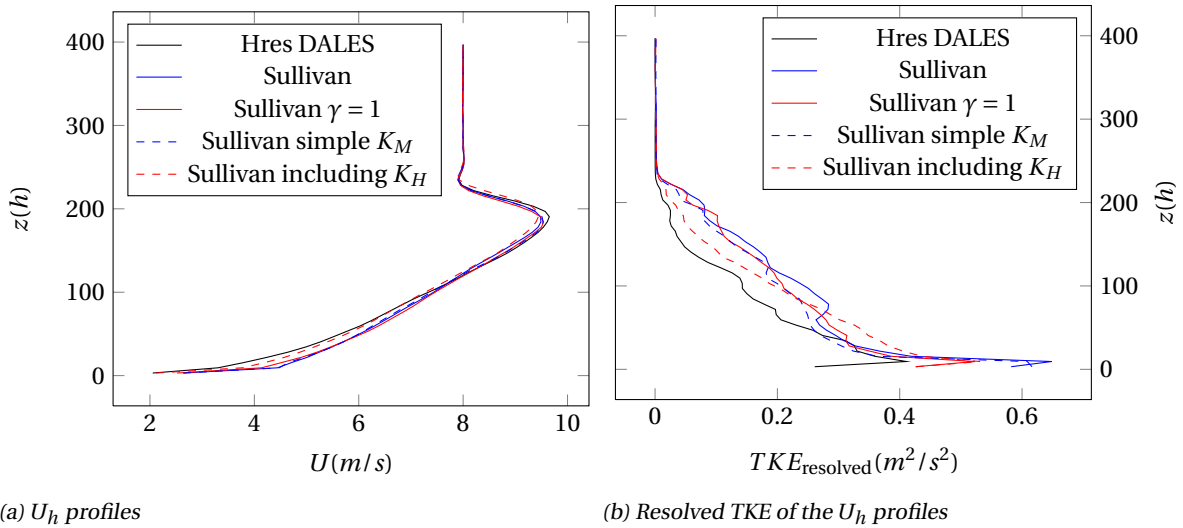
Figure 6.1: Resulting profiles of the different adaptations of Sullivan's model and the original DALES model. The DALES solution is high resolution with $\Delta x = 3.125\,m$, the Sullivan solutions have a grid spacing of $\Delta x = 6.25\,m$

From this Figure 6.1 it is clear that all the adaptations of Sullivan's original idea nicely follow the high resolution result, at least at $\Delta x = 6.25$ m, as the difference between the different graphs is smaller than $\sqrt{TKE_{\bullet textresolved}} = \sqrt{\sigma_U^2}$. However, it appears that at the second grid point there is a small maximum in the derivative of the horizontal speed , which every model has. This is located at the second half level $z = \frac{3}{2}\Delta z$, see 2.2. This is the first level where u and v are defined above the level $z = \Delta z$ where the K_M is fixed to obey Monin Obukhov. This might indicate an error in either the implementation of the Sullivan model, or an imperfection in the implementation of the boundary condition in the original DALES code.

How do the Sullivan models perform when the grid size is changed? Again, the height of the nocturnal jet is used as a reference point, compared to the results of the original DALES code. The results of these simulations

are plotted in Figure 6.2. The Sullivan adaptations behave differently from the original DALES code: the nocturnal jet height does not grow with the grid size, but converges to a constant value. Unfortunately, this value is not at the expected height of 190 m from the high resolution solution, but it is located at ≈ 140 m. However, Figure 4.4b shows that this is indeed the height at which also the simple 1D model converses for $\alpha = 5$. So the Sullivan solutions do exactly coincide with the Monin Obukhov theory.
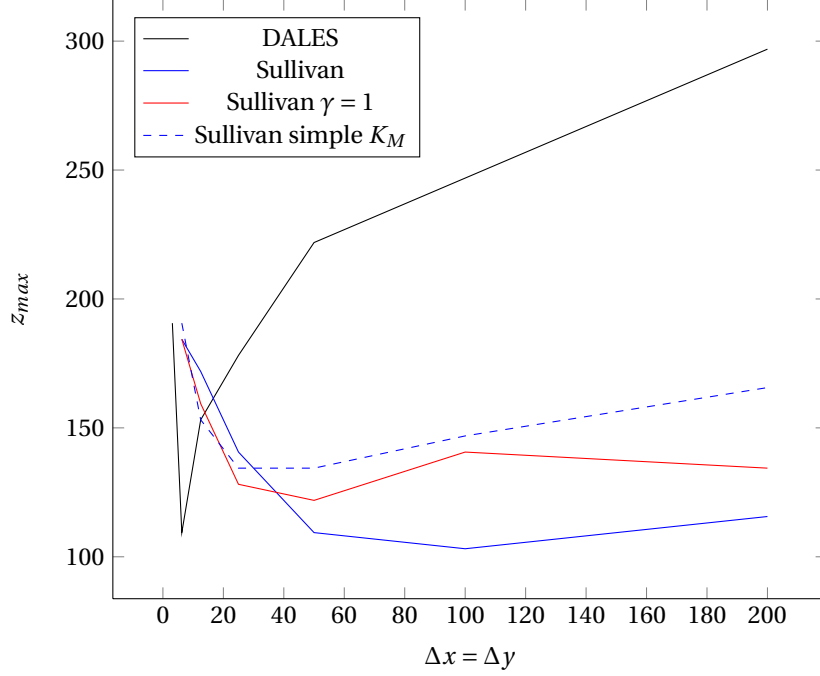
Figure 6.2: *Height of the nocturnal jet versus the horizontal grid resolution in the original DALES code and the different Sullivan models*

In Figure 6.3 the resulting Monin-Obukhov similarity functions are plotted for one illustrating grid size of $\Delta x = 25m$. From the four figures, it is clear that the implementations of Sullivan's model all yield great results for the similarity functions. The Prandtl number is indeed one, and the $\phi_{m,h}$ coincide nicely with the $1 + 5z/\Lambda$ graph. In Appendix G results for other Δx can be found, which also show that the Sullivan models follow the Monin Obukhov theory very well. Only when Δx becomes really large (100 or 200 m), the similarity functions diverges from the expected $1 + 5z/\Lambda$.

Compared with the Hres DALES result, the TKE profiles are remarkable. For the original Sullivan model, the TKE profiles of the highest and lowest resolution run are plotted in Figure 6.4. There is still a difference between the big and small horizontal grid sizes. As could be expected from the DALES results, the resolved TKE dominates when Δx is small, and the subgrid TKE dominates when Δx is large. Whereas the total TKE increased with Δx using the original DALES code, the total TKE *decreases* with Δx with the Sullivan models. However, the total TKE remains in the same order of magnitude between the different low resolution runs with the Sullivan code ($\Delta x = 50, 100, 200$ m, Appendix G.1), which could explain why the height of the nocturnal jet (Figure 6.2) does converge.

Can these differences between the original DALES code and the Sullivan model be understood from the changes made in the Sullivan model? In order to answer this question, it is useful to look the different shear terms in the original DALES and new Sullivan LES equation, see 5.5. The different shear terms are given by:

$$\tau_{subgrid} = \sqrt{\langle \tau_{uw} \rangle^2 + \langle \tau_{vw} \rangle^2}$$
$$\tau_{resolved} = \sqrt{\langle \widetilde{u}\widetilde{w} \rangle^2 + \langle \widetilde{v}\widetilde{w} \rangle^2} \tag{6.2}$$
$$\tau_{total} = \tau_{subgrid} + \tau_{resolved}$$

(a) Original Sullivan model, $\Delta x = 25$ m

(b) Sullivan model (simple K_M), $\Delta x = 25$ m

(c) Sullivan model with $\gamma = 1$, $\Delta x = 25$ m

(d) Sullivan model (including K_H), $\Delta x = 25$ m
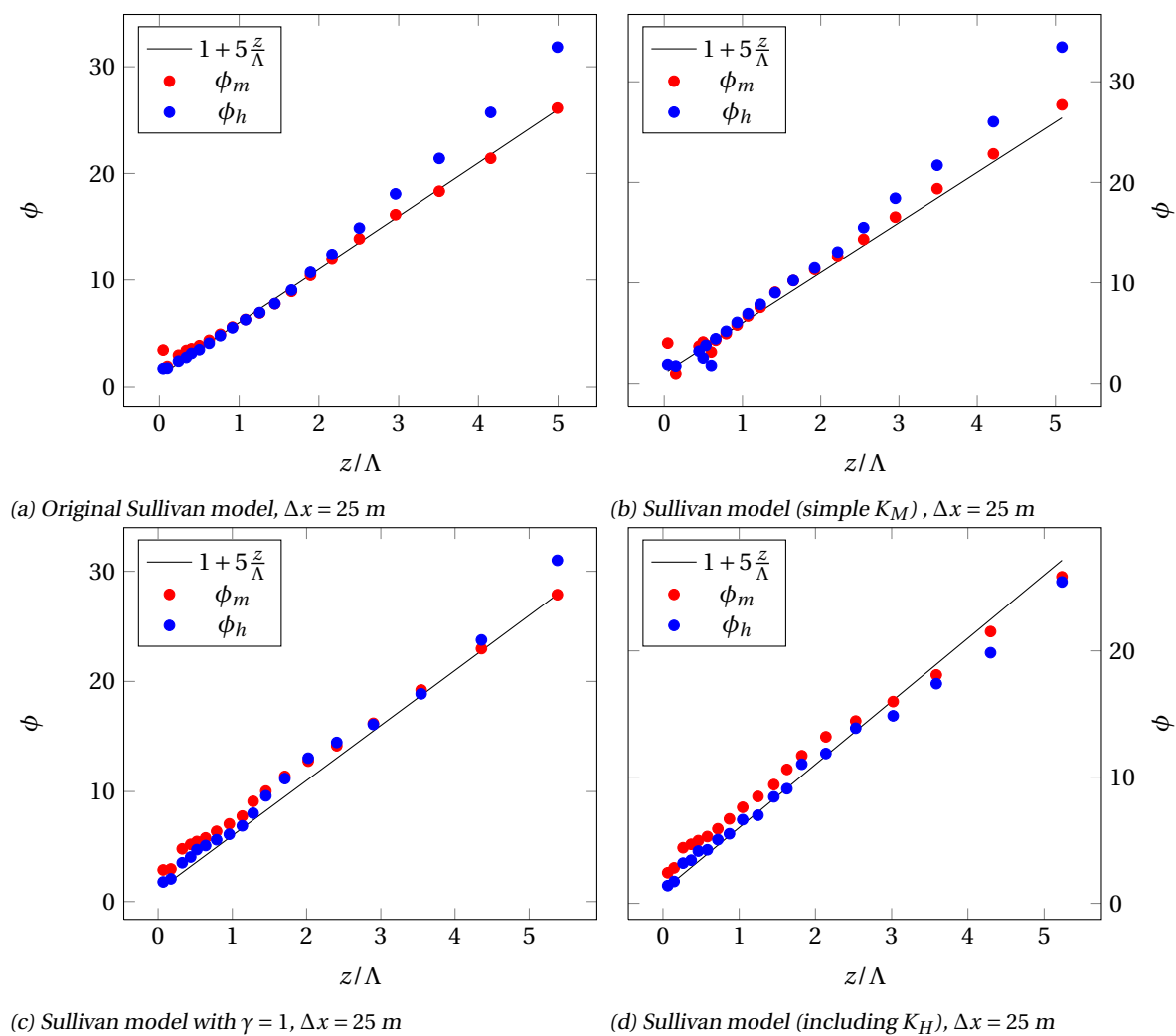
Figure 6.3: Monin-Obukhov similarity functions for the Sullivan results of the GABLS case

(a) $\Delta x = 6.25$ m

(b) $\Delta x = 200$ m
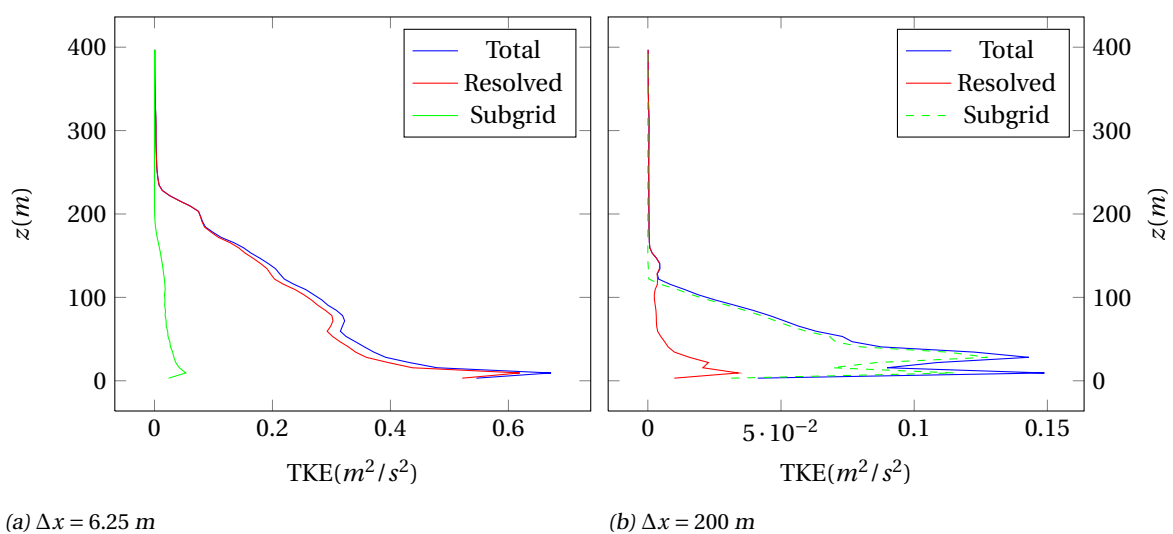
Figure 6.4: Vertical distribution of turbulent kinetic energy for two Sullivan simulations of the GABLS case

As described in 5, the Sullivan model introduces a new shear term in the LES equation. At the same time, the subgrid shear term is multiplied by the factor γ. The new terms are thus given by:

$$\tau_{subgrid} = \sqrt{\langle \gamma \tau_{uw} \rangle^2 + \langle \gamma \tau_{vw} \rangle^2}$$
$$\tau_{Sullivan} = \sqrt{(K_M \langle S_{uw} \rangle)^2 + (K_M \langle S_{vw} \rangle)^2}$$
$$\tau_{total} = \tau_{subgrid} + \tau_{resolved} + \tau_{Sullivan}$$

(6.3)

As an illustration, the shear profiles of the original DALES model and the Sullivan model are plotted, both with a grid size of $\Delta x = 25$ m, in Figure 6.5. While the shear in DALES in completely dominated by the subgrid contribution, in the Sullivan model especially the resolved and "Sullivan" shear $\tau_{Sullivan}$ play an important role. The subgrid shear is only quite big at the surface, which is expected.

How does the Sullivan model function? Right above the surface, $z \approx 30$ m in the figures, the mean shear $\langle S \rangle$ is quite big. This decreases the production of subgrid TKE, resulting in smaller amount of subgrid TKE on this level, which can be seen in Figure 6.4. Less subgrid TKE means smaller $K_{m,h}$, and therefore less subgrid shear as compared to the Hres DALES result. At this point, there is some Sullivan shear to ensure obedience to the Monin Obukhov theory. Because the mean shear does not damp velocity fluctuations as the subgrid shear does, resolved motions can be formed. For runs with low $\Delta x < 50$, the simulation becomes dominated by the resolved solutions, and not the subgrid solutions as the original DALES code. This appears to be the real reason for consistency with the Monin Obukhov theory: the problem is not dominated any more by the subgrid parametrization.

From Figure 6.5 it seems that the functioning of the Sullivan model is as follows. The Sullivan shear term is only quite big just above the surface, apparently creating resolved motions. Through this mechanism, the simulation becomes dominated by the resolved solutions, and not the subgrid solutions as the original DALES code. This appears to be the real reason for consistency with the Monin Obukhov theory: the problem is not dominated any more by the subgrid parametrization.
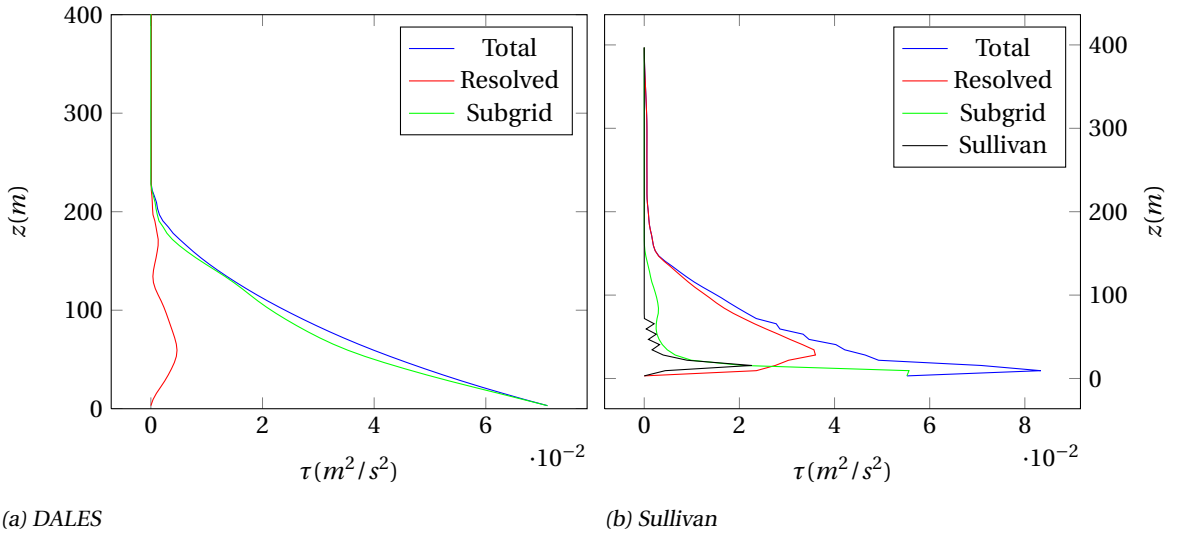
(a) DALES

(b) Sullivan

Figure 6.5: Vertical distribution of shear for the DALES and Sullivan code with a grid size of $\Delta x = 25$ m

6.1. Results for an unstable boundary layer

In order to test whether the Sullivan model performs equally well in unstable atmospheric conditions, also some test have been done using a Convective Boundary Layer case. In this artificial case is initiated with a geostrophic wind speed of 8 $\frac{m}{s}$ in the x-direction. The initial θ_v profile is 290 K for the first 300 m, above a slight gradient of 8.2 $\frac{K}{km}$. Constant velocity and θ_v were set at the ground level. In Figure 6.6 the results of this analysis has been plotted. From analyzing the variation of both profiles, it is clear that the original Sullivan

models produces comparable results as the original DALES model. These plots have only been added to give a brief inside in whether there would be big difference between the Sullivan model and the original LES code, no further research has been done in unstable boundary layer.

(a) U_h profiles

(b) Variance of the U_h profiles
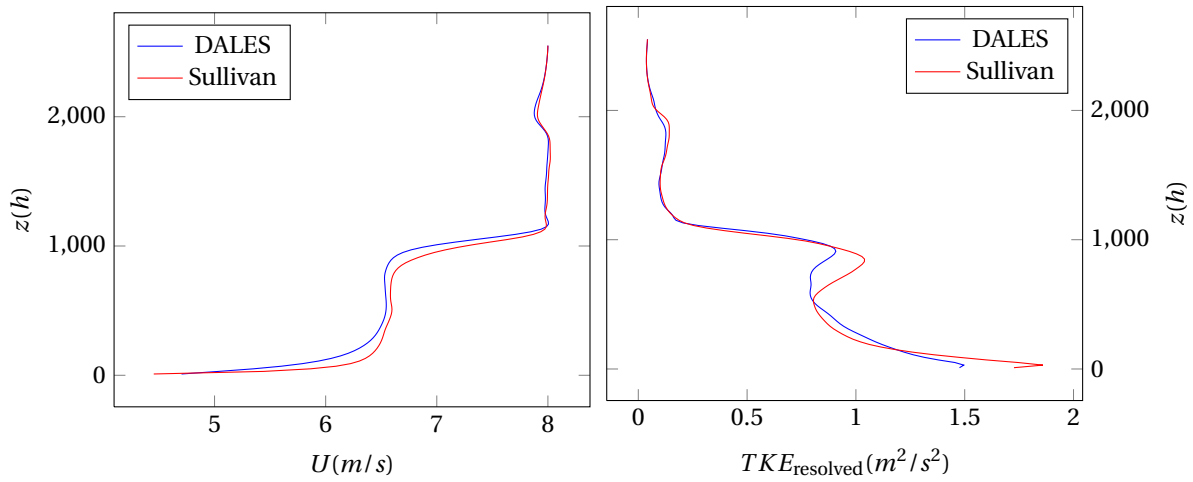
Figure 6.6: Resulting profiles of the CBL case for the DALES and original Sullivan model.

7

DISCUSSION AND CONCLUSION

7.1. SUMMARY

In this thesis the functioning of the LES model with the prognostic subgrid TKE equation in the stable boundary layer has been studied using the GABLS case. The results show that for a horizontal grid size $\Delta x > 3.125$ m, the LES solution becomes dominated by the subgrid parametrization. It can be derived that the subgrid TKE and therefore the eddy diffusivities in that case scale with the grid size, which was proven qualitatively by experiments. It was also shown that the subgrid dominated solutions did not follow the Monin-Obukhov similarity theory: the turbulent Prandtl number was not the expected value, and the slope of the similarity functions depended on the grid size.

In order to overcome these issues with simulating the stable boundary layer, the model proposed by Sullivan *et al.* [2] was implemented. Due to the new model formulation, production of subgrid TKE is surpressed whenever the mean shear is large, which ensures less subgrid shear and therefore more production of resolved motions. An introduced mean shear term in the LES equations ensured that the solutions followed the Monin-Obukhov theory. Several adaptations of Sullivan's model have been researched, the results were quite similar. All the adaptations improved the LES results: the because of the increased production of resolved motions, the results were not subgrid dominated for $\Delta x < 100$ m. This also ensured the correct similarity functions. However, the Sullivan models were not completely robust to grid size changes.

7.2. COMPARISON OF DIFFERENT MODEL ADAPTATIONS

Several adaptations of the LES code have been proposed and tested, what would be the best option? Important characteristics for a good subgrid model are of course the following:

- A new subgrid model of the code should produce (statistically) the same results as the high resolution DALES run.

- The results should, for stable circumstances, obey the Monin-Obukhov similarity theory

- The results should be robust for changes in the grid size.

- As the DALES code worked fine for unstable atmospheric conditions, the new subgrid code should not influence these results.

As shown in the DALES Results Chapter 4 , the original DALES code does not comply with the first three requirements for the stable situation, especially when the subgrid parametrization dominates the solution, The results change with the grid size, and also the Monin-Obukhov similarity theory is not followed any more. First, several simple solutions for these problems have been tested. Changing the definitions of the subgrid constants $c_{h,\epsilon}$ did improve the compliance with the similarity theory, as long as the horizontal grid size was not too large. Trying to create an anisotropic $K_{m,h}$ however, did not improve the model at all, although it was shown that anisotropy in the grid cells was part of the problem.

A second series of test was done on the model by Sullivan *et al.* [2] and several adaptations. These models all performed well, there was not much difference between the original model, the implementation with a simpler mean strain diffusivity K_M, the model without the factor γ and the model with a extra buoyancy term. Although these models were not completely robust to grid size changes, the results seemed to converge for higher grid sizes. Also the Monin-Obukhov theory was obeyed, even at extreme grid sizes.

7.2.1. ROBUSTNESS FOR GRIDSIZE CHANGES

As shown in the previous section and in the Results chapters, almost every model is sensitive to the change in horizontal grid size. In order to illustrate this, all the graphs of height of the nocturnal jet versus the horizontal grid have been plotted in Figure 7.1. It has been shown in Section 4.2 that part of this behaviour is due to an anisotropic grid, but this explains not all. While other problems of the DALES code can be solved with different subgrid implementations, the dependency on horizontal grid size remains a problem.
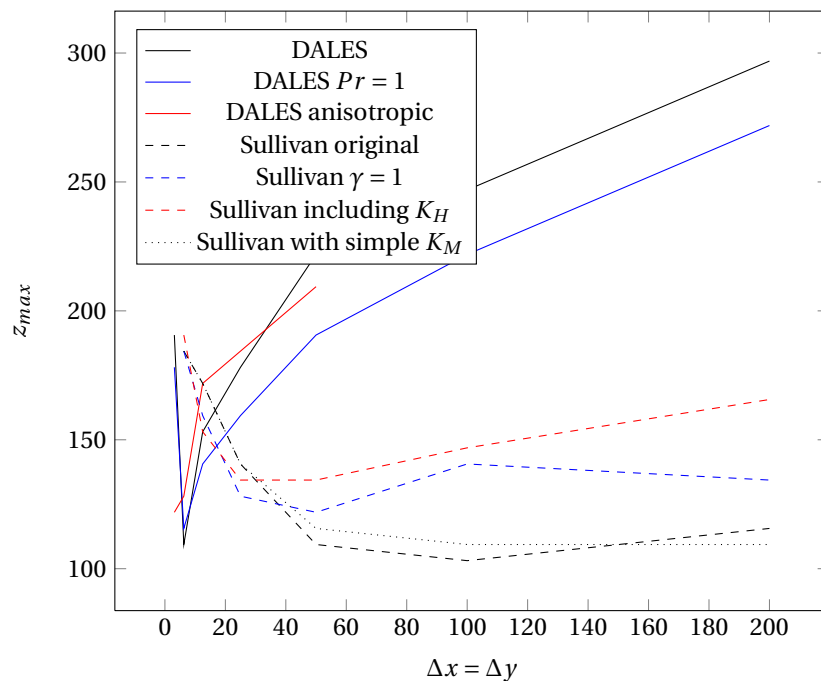
Figure 7.1: Height of the nocturnal jet versus the horizontal grid resolution in the original DALES code, adaptations of the DALES code and the different Sullivan models

Why is this the case? First, it is important to remember that the whole LES framework is based on the division between resolving large scale ($> \Delta$) turbulence and parameterizing small scale turbulence. In normal simulations this is fine, as the results will be completely dominated by the resolved calculations. In the GABLS case however with grid size bigger than a few meter, and all other simulations of the stable boundary layer, most of the turbulence is in fact subgrid scale: the parameterization determines the results of the simulation.

The results varying with grid size are then easy to understand. In the simulations of the GABLS case with the highest resolutions, all models produce resolved motion dominated results. For grid sizes greater than $\Delta x = 50m$, all models produce subgrid based results. Between those to grid sizes, there must be a change from the reliable resolved solutions to the parameterized subgrid solutions, which do not produce the same results. Figure 7.1 shows nicely the difference in resulting nocturnal jet height between the original codes and the Sullivan model: the Sullivan model and adaptations converge when subgrid is dominated ($\Delta x > 50$), whereas the DALES code does not.

7.2.2. RUNTIME OF DIFFERENT MODELS

For practical implementation, also the runtime of the different models is important. If a model is slightly better than the baseline, but at a much higher CPU time, it might not be an improvement for practical imple-

mentions. In Table 7.1 are the average run times of all model formulations.

Model name	Average run time (10^3 s)
DALES	18
DALES $Pr_t = 1$ adapted	58
DALES anisotropic $K_{m,h}$	56
Sullivan original	14
Sullivan without γ	13
Sullivan with simple K_M	14
Sullivan including buoyancy term	13

Table 7.1: Runtime of 9 hours GABLS case for the different codes (s).

It is striking to see that all Sullivan based models have a lower run time than the original DALES code, although a lot more calculations need to be performed. This is due to the fact that the Sullivan code generally runs with a bigger time step for numerical integration, which is calculated in the code based on numerical stability criteria.

However, not too much emphasis should be put on the numbers in Table 7.1. Run times of different runs with the same code experienced big differences of sometimes > 100% . Also the difference between the original DALES code and the DALES code with $Pr_t = 1$ and anisotropic $K_{m,h}$ is too big to be explained by just the simple changes done. Furthermore, the computer cluster *Cirrus* is constantly updated, and the different experiments have not been done at the same time.

When using parallel computing to run the codes, another aspect needs to be taken into account. Averaging over the whole horizontal domain, which is done extensively in the Sullivan model, cost a lot of time, as different processors need to communicate with one another. Although this increased time is not visible in the results presented here, it is a big problem with the GPU version of the code.

7.3. Outlook

The results of this thesis suggest that implementing the model of Sullivan into DALES would be an improvement, resulting in better solutions if modeling stable boundary layers with a large grid size and not interfering with the good results in the unstable boundary layer. As several variants were tested, which all performed equally well, the simplest variant, with $\gamma = 1$ and a simple definition of the new mean shear diffusivity K_M is probably best. However, there are still some issues which need to be resolved.

First, the physical idea behind the model. As presented in this thesis, Sullivan's model is an engineered way to let the LES results fit the measured and proposed Monin Obukhov functions. The DALES equations can be derived directly from the Navier Stokes equations, and the production of subgrid TKE corresponds therefore with the transport of kinetic energy from the larger resolved motions. As in the Sullivan model different terms are subtracted in the subgrid TKE and the LES u_i equations, this symmetry is broken. In this paper it has been shown that the effect of these extra terms is only in the lower part of the boundary layer and induces resolved motions, at which point the subgrid model is again of lesser importance. However, it remains that an unphysical asymmetry is present in the equations. It would perhaps be an idea to reformulate the normal eddy diffusivities $K_{m,h}$ in a manner comparable to Sullivan's idea, instead of linking them the subgrid TKE.

A second issue involves the slab averaging done in the new subgrid model. For the GABLS case it is fine to average over the whole domain, but this is not right to do when LES is used on a much bigger scale. As Schalkwijk [4] showed, LES might be used in the future for weather predictions with a computational domain of a whole country, at which point slab averaging over the whole domain would not do. When the Sullivan model will be implemented at this scale, other possibilities need to be researched. A very pragmatic idea would be to average per core used, as this is computational probably most efficient. However, this would not make much sense physically, as the physical architecture of the computer should not influence the results of the LES simulation. A better way is to average over grid cells which are linked in space and are "alike" in atmospheric conditions. How to define "alike" would be a interesting research question.

BIBLIOGRAPHY

[1] R. J. Beare, M. K. Macvean, A. A. Holtslag, J. Cuxart, I. Esau, J.-C. Golaz, M. A. Jimenez, M. Khairoutdinov, B. Kosovic, D. Lewellen, *et al.*, *An intercomparison of large-eddy simulations of the stable boundary layer*, Boundary-Layer Meteorology **118**, 247 (2006).

[2] P. P. Sullivan, J. C. McWilliams, and C.-H. Moeng, *A subgrid-scale model for large-eddy simulation of planetary boundary-layer flows*, Boundary-Layer Meteorology **71**, 247 (1994).

[3] T. Heus, C. Van Heerwaarden, H. Jonker, A. Pier Siebesma, S. Axelsen, K. Dries, O. Geoffroy, A. Moene, D. Pino, S. De Roode, *et al.*, *Formulation of the dutch atmospheric large-eddy simulation (dales) and overview of its applications*, Geoscientific Model Development **3**, 415 (2010).

[4] J. Schalkwijk, *Toward Turbulence-Resolving Weather and Climate Simulation*, Ph.D. thesis, TU Delft, Delft University of Technology (2015).

[5] A. Monin and A. Obukhov, *Basic laws of turbulent mixing in the surface layer of the atmosphere*, Contrib. Geophys. Inst. Acad. Sci. USSR **151**, 163 (1954).

[6] J. C. Wyngaard, *Toward numerical modeling in the "terra incognita"*, Journal of the Atmospheric Sciences **61**, 1816 (2004).

[7] R. B. Stull, *An introduction to boundary layer meteorology*, Vol. 13 (Springer Science & Business Media, 1988).

[8] J. W. Deardorff, *Stratocumulus-capped mixed layers derived from a three-dimensional model*, Boundary-Layer Meteorology **18**, 495 (1980).

[9] J. A. Businger, J. C. Wyngaard, Y. Izumi, and E. F. Bradley, *Flux-profile relationships in the atmospheric surface layer*, Journal of the Atmospheric Sciences **28**, 181 (1971).

[10] P. Baas, S. R. de Roode, and G. Lenderink, *The scaling behaviour of a turbulent kinetic energy closure model for stably stratified conditions*, Boundary-layer meteorology **127**, 17 (2008).

[11] F. Nieuwstadt, *The turbulent structure of the stable, nocturnal boundary layer*, Journal of the Atmospheric Sciences **41**, 2202 (1984).

[12] J. R. Garratt, *The atmospheric boundary layer* (Cambridge university press, 1994).

[13] P. G. Duynkerke and S. R. Roode, *Surface energy balance and turbulence characteristics observed at the sheba ice camp during fire iii*, Journal of Geophysical Research: Atmospheres (1984–2012) **106**, 15313 (2001).

[14] J. Smagorinsky, *General circulation experiments with the primitive equations: I. the basic experiment**, Monthly weather review **91**, 99 (1963).

[15] B. Kosovic and J. A. Curry, *A large eddy simulation study of a quasi-steady, stably stratified atmospheric boundary layer*, Journal of the Atmospheric Sciences **57**, 1052 (2000).

[16] M. Khairoutdinov, *Private communication*, (2010).

A

DERIVATION OF THE DALES SUBGRID EQUATION

The subgrid TKE equation is given by:

$$\frac{\partial e}{\partial t} + \widetilde{u_j}\frac{\partial e}{\partial x_j} = \frac{\widetilde{\theta_v'w'}}{\theta_0}g - \frac{\partial \widetilde{\pi'u_j'}}{\partial x_j} - \tau_{ij}\frac{\partial \widetilde{u_i}}{\partial x_j} - \frac{\partial \widetilde{e'u_j'}}{\partial x_j} - \epsilon \tag{A.1}$$

For the unknown turbulent production terms $\widetilde{w'\theta_v'}$, τ_{ij} and the turbulent fluxes $\widetilde{\pi'u_j'}$ and $\widetilde{e'u_j'}$, the following parametrisation are used:

$$\tau_{ij} = -K_m\left(\frac{\partial \widetilde{u_i}}{\partial x_j} + \frac{\partial \widetilde{u_j}}{\partial x_i}\right) = -2K_m S_{ij}$$

$$\widetilde{\theta_v'u_j'} = -K_h\frac{\partial A\widetilde{\theta_l} + B\widetilde{q_t}}{\partial x_j} = -K_h\frac{\partial \widetilde{\theta_v}}{\partial x_j} \equiv -K_h\frac{\theta_0}{g}N^2 \tag{A.2}$$

$$\widetilde{\pi'u_j'} + \widetilde{e'u_j'} = -K_m\frac{\partial e}{\partial x_j}$$

By substituting Equations A.2 into Equation A.1, and taking $\epsilon = \frac{c_\epsilon}{\lambda}e^{3/2}$ the following can be found:

$$\frac{\partial e}{\partial t} + \widetilde{u_j}\frac{\partial e}{\partial x_j} = -K_h N^2 - \frac{\partial}{\partial x_j}\left(-K_m\frac{\partial e}{\partial x_j}\right) - \tau_{ij}\frac{\partial \widetilde{u_i}}{\partial x_j} - \epsilon \tag{A.3}$$

How is this implemented in the DALES code? Two important computational steps are taken:

- As the K_m and K_h terms depend on $\sqrt{e}$, it is useful to define the whole subgrid TKE equation in this variable. Using the product rule for differentiation:

$$\frac{\partial e}{\partial t} = 2e^{1/2}\frac{\partial e^{1/2}}{\partial t} \tag{A.4}$$

This holds of course also for differentiation with respect to x_j, and therefore the both sides of the subgrid TKE equation can be divided by $2e^{1/2}$.

- The total shear term in the subgrid TKE equation is modeled as:

$$\widetilde{u_i'u_j'}\frac{\partial \widetilde{u_i}}{\partial x_j} = -K_m\left(\frac{\partial \widetilde{u_j}}{\partial x_i} + \frac{\partial \widetilde{u_i}}{\partial x_j}\right)\frac{\partial \widetilde{u_i}}{\partial x_j} = -2K_m S_{ij}\frac{\partial \widetilde{u_i}}{\partial x_j} \tag{A.5}$$

41

By writing out all the terms of $S_{ij}\frac{\partial \widetilde{u_i}}{\partial x_j}$ it can be seen that this equation can be rewritten to a more simpler one, saving cpu memory. The resulting formulation is:

$$\left(\frac{\partial \widetilde{u_j}}{\partial x_i} + \frac{\partial \widetilde{u_i}}{\partial x_j}\right)\frac{\partial \widetilde{u_i}}{\partial x_j} = \frac{1}{2}\left(\frac{\partial \widetilde{u_j}}{\partial x_i} + \frac{\partial \widetilde{u_i}}{\partial x_j}\right)^2 = 2\sum_{i,j} S_{ij}^2 \equiv S^2 \tag{A.6}$$

Combining these steps, yields the following formulation for the subgrid TKE equation:

$$\frac{\partial e^{1/2}}{\partial t} + \widetilde{u_j}\frac{\partial e^{1/2}}{\partial x_j} = \frac{1}{2e^{1/2}}(\underbrace{-K_h N^2}_{P_b} + \underbrace{K_m S^2}_{P_s}) + K_m\frac{\partial e^{1/2}}{\partial x_j} - \frac{c_\epsilon e}{2\lambda} \tag{A.7}$$

B

THE 1D MODEL FOR STABLE ATMOSPHERIC BOUNDARY LAYER

In this appendix, the derivation and implementation of the 1D model for the stable boundary layer will be given. From the results of the DALES run, it becomes clear the buoyancy force and the transport terms in the LES equations can be neglected. The term F_i is given by the Coriolis force:

$$
\begin{aligned}
F_x &= 2\Omega \sin\psi\, v = f v \\
F_y &= -2\Omega \sin\psi\, u = -f u
\end{aligned}
$$

(B.1)

The $\Omega = \frac{2\pi}{24*3600} \frac{m}{s}$ is the earth's angular velocity and $\psi = 72°$ is the latitude in the GABLS case. The simplified equations are now given by:

$$
\begin{aligned}
\frac{\partial u}{\partial t} &= f v - \frac{\partial p}{\partial x} - \frac{\partial \tau_{uw}}{\partial w} \\
\frac{\partial v}{\partial t} &= -f u - \frac{\partial p}{\partial y} - \frac{\partial \tau_{vw}}{\partial w} \\
\frac{\partial \theta_v}{\partial t} &= -\frac{\partial \overline{w\theta_v}}{\partial z}
\end{aligned}
$$

(B.2)

If there is no turbulence in a steady state atmosphere, the pressure term and Coriolis term should cancel, resulting in the geostrophic wind:

$$
\begin{aligned}
\frac{\partial p}{\partial x} &= f v_{geo} \\
\frac{\partial p}{\partial y} &= -f u_{geo}
\end{aligned}
$$

(B.3)

In the GABLS case, $u_{geo} = 8\frac{m}{s}$ and $v_{geo} = 0$. For the eddy diffusion terms the down gradient diffusion from Formula 2.9 and 2.10 can be used. As there is no z velocity in this simple model, the parametrization for momentum simplifies to:

$$
\tau_{uw,vw} = -K_m \frac{\partial u, v}{\partial z}
$$

(B.4)

In order to obtain a closure scheme for the $K_{m,h}$ terms that obeys the Monin-Obukhov similarity theory, Formula 2.34 is used with $Pr_t = 1$. Combining parametrisations with the simplified LES equation, the following

43

system should be solved by numerical integration:

$$Ri_g = \frac{\frac{g}{\theta_0}\frac{\partial \theta_v}{\partial z}}{\left(\frac{\partial u}{\partial z}\right)^2 + \left(\frac{\partial v}{\partial z}\right)^2}$$

$$K_{m,h} = (\kappa z)^2 (1 - \alpha Ri_g)^2 \sqrt{\left(\frac{\partial u}{\partial z}\right)^2 + \left(\frac{\partial v}{\partial z}\right)^2}$$

$$\frac{\partial u}{\partial t} = fv - fv_{geo} - \frac{\partial}{\partial z}\left(-K_m \frac{\partial u}{\partial z}\right)$$

$$\frac{\partial v}{\partial t} = -fu + fu_{geo} - \frac{\partial}{\partial z}\left(-K_m \frac{\partial v}{\partial z}\right)$$

$$\frac{\partial \theta_v}{\partial t} = -\frac{\partial}{\partial z}\left(-K_h \frac{\partial \theta_v}{\partial z}\right)$$

(B.5)

The actual code is programmed in MatLab 2014b and is added here for reference:

```
clc; clear all; close all;

% Integration parameters
H=400; %m
T=3600*9; %s
dz=6.25; %m
dt=0.25; %s
z=(0:dz:H)';
n=length(z);
steps=round(T/dt);
zh=(z(2:end)+z(1:end-1))/2;

% Physical parameters
f=1e-4; %1/s
K=1; %m^2/s
Ug=8; %m/s
Vg=0; %m/s
Tg=263.5; %K
T0=265;
 alpha=5;
Pr=1;
kappa=0.4;

% Initialisation
u0=Ug*ones(n,1); u0(1)=0;
v0=zeros(n,1);
u=u0;
v=v0;
Km=zeros(n-1,1);
Kh=Km; S2=Km; N2=Km;

% Extended initialisation th
[ho100, h100 ]=min(abs(z-100));
th=v0;
th(1)=Tg(1);
th(2:h100)=T0*ones(h100-1,1);
th(h100+1:n)=T0+0.01*(z(h100+1:n)-(ho100+1));
th0=th;

% Surface cooling
Tg=linspace(263.5,263.5-9*0.25,steps);

for i=1:steps

    %The formulation of K_m
    S2=((u0(2:end)-u0(1:end-1))/dz).^2+((v0(2:end)-v0(1:end-1))/dz).^2;
    N2=9.81/Tg(i)*(th0(2:end)-th0(1:end-1))/dz;
```

```matlab
    Rig=N2./(S2+1e-6);

    for k=1:n-1
        if Rig(k)<(Pr/alpha)
            Km(k)=(1-alpha * Rig(k)/Pr).^2 * (kappa* zh(k)).^2 * sqrt (S2(k));
        else Km(k)=1e-4;
        end
    end
    Kh=Pr*Km;

    % Fluxes
    uw=-Km.*(u0(2:end)-u0(1:end-1))/dz;
    vw=-Km.*(v0(2:end)-v0(1:end-1))/dz;
    wthv=-Kh.*(th0(2:end)-th0(1:end-1))/dz;

    % Integration
    u(1)=0; v(1)=0; th(1)=Tg(i);
    u(2:end-1)=u0(2:end-1)+dt*( f*(v0(2:end-1)-Vg)-(uw(2:end)-uw(1:end-1))/dz);
    v(2:end-1)=v0(2:end-1)+dt*(-f*(u0(2:end-1)-Ug)-(vw(2:end)-vw(1:end-1))/dz);
    th(2:end-1)=th0(2:end-1)+dt*(-(wthv(2:end)-wthv(1:end-1))/dz);
    u(end)=u(end-1);
    v(end)=v(end-1);
    th(end)=th(end-1);

    %Reset
    u0=u;
    v0=v;
    th0=th;

    if rem(i,(steps/36))==0
        pause(0.5)
        plot(sqrt(u.^2+v.^2),z)

        subplot(2,2,1)
        plot(u,z,v,z,sqrt(u.^2+v.^2),z)
        xlabel('U_s')
        ylabel('z')
        legend('u','v','U_s')
        subplot(2,2,2)
        plot(th,z)
        xlabel('\theta_v')
        ylabel('z')
        subplot(2,2,3)
        plot(uw,zh,vw,zh)
         xlabel('$\bar{uw}$','Interpreter','LaTex')
        ylabel('z')
        legend({'$\bar{uw}$','$\bar{vw}$'},'Interpreter','LaTex')
        subplot(2,2,4)
        plot(wthv,zh)
         xlabel('$\bar{w\theta_v}$','Interpreter','LaTex')
        ylabel('z')

    end

end
```

C

SETTING OF DALES

Here a NAMoptions file is presented, used to select different run options of DALES.

```
RUN
iexpnr          =   000                 lwarmstart  =   .false.
startfile       =   'initd06h00m000.017'  runtime   =   32400
trestart        =   3600                dtmax       =   10
ladaptive       =   .true.              irandom     =   43
randthl         =   0.1                 randqt      =   2.5e-5
nsv             =   1


DOMAIN
imax            =   64                  jtot        =   64
kmax            =   64                  xsize       =   400.
ysize           =   400.                xlat        =   73.
xlon            =   0.                  xday        =   0.
xtime           =   0.


PHYSICS
ps              =   101500.00           thls        =   265.
lmoist          =   .false.             lcoriol     =   .true.
iradiation      =   0                   ltimedep    =   .true.


NAMSURFACE
albedoav        =   0.24                wtsurf      =   -0.04
wqsurf          =   0.                  isurf       =   2
lsmoothflux     =   .false.             ustin       =   -999
z0              =   0.2


NAMRADSTAT
dtav            =   60                  timeav      =   600.
lstat           =   .true.
```

```
DYNAMICS
llsadv          =   .false.   lqlnr      =   .false.
cu              =   7.        cv         =   0.
iadv_mom        =   5         iadv_tke   =   5
iadv_thl        =   5         iadv_qt    =   5
iadv_sv         =   5

NAMSUBGRID
ldelta1         =   .false.   cn         =   0.76

NAMBUDGET
lbudget         =   .true.    dtav       =   60.
timeav          =   600.

NAMCHECKSIM
tcheck          =   6

NAMTIMESTAT
ltimestat       =   .true.    dtav       =   60

NAMGENSTAT
lstat           =   .true.    dtav       =   60
timeav          =   600

NAMSTATTEND
dtav            =   60        ltend      =   .true.
timeav          =   600.
```

---

[1]If .ldelta. is switched to true, $\lambda = \Delta$. If switched false, as done here, $\lambda = \min\left(\Delta, c_n \sqrt{e}/N\right)$

<div style="text-align: right">

D

</div>

S<small>IMULATION</small> <small>IDENTIFICATION</small>

In this section, the simulation run numbers of the experiments described in this thesis can be found for reference. All the simulations can be found in the directory */nfs/livedata/victor/Les/Experiments/Gabls1*. The important simulations can be found here, in this directory is also an extensive *readme* file. All the folders contain a series of simulation where only the total horizontal domain is changed. Each simulation includes a folder with the Fortran files of the exact code used.

Table D.1: Reference table for the experiment numbers used in this thesis

Model	Directory	Description
Original DALES	V512_V518	Original DALES code
DALES with $c_{h,\epsilon}$ adapted	V486_V492	DALES code with $c_{h,\epsilon}$ as described in Formula 4.8
DALES with anisotropic $K_{m,h}$	V493_V499	Anisotrope $K_{m,h}$ following Section 4.2
Original DALES, Δz=12.5 m	V519_V526	Original DALES code with adapted Δz
Original DALES, Δz=25 m	V527_V534	Original DALES code with adapted Δz
Original Sullivan code	V452_V457	Original model described by Sullivan *et al.* [2]
Sullivan with $\gamma = 1$	V473_V478	Sullivan model with $\gamma = 1$ everywhere
Sullivan with simple K_M	V458_V463	Different definition of K_M following Section 5.3
Sullivan with buoyancy adaptation	V467_V472	Buoyancy fluxes as in 5.4
Original Sullivan, Δz=12.5 m	V535_V541	Original Sullivan code with adapted Δz
Original Sullivan, Δz=25 m	V542_V548	Original Sullivan code with adapted Δz

A week before the deadline of this thesis, an error was found in the boundary conditions modelling of the original DALES code. This affected mainly the TKE budgets, give rise to a big TKE transport term. The runs with DALES with the grid sizes $\Delta x = 6.25$ m up to $\Delta x = 50$ m were redone using this new code and using a height of 800 m with 128 grid points in the vertical direction: twice as high as the other simulations, but with the same Δz. However, only the results up to a height of 400 m are presented.

E

RESULTS OF THE GABLS CASE WITH THE HIGH RESOLUTION DALES CODE

In this appendix the details of the high resolution reference run of the GABLS case with DALES can be found.

(a) U_s profile

(b) θ_v profile
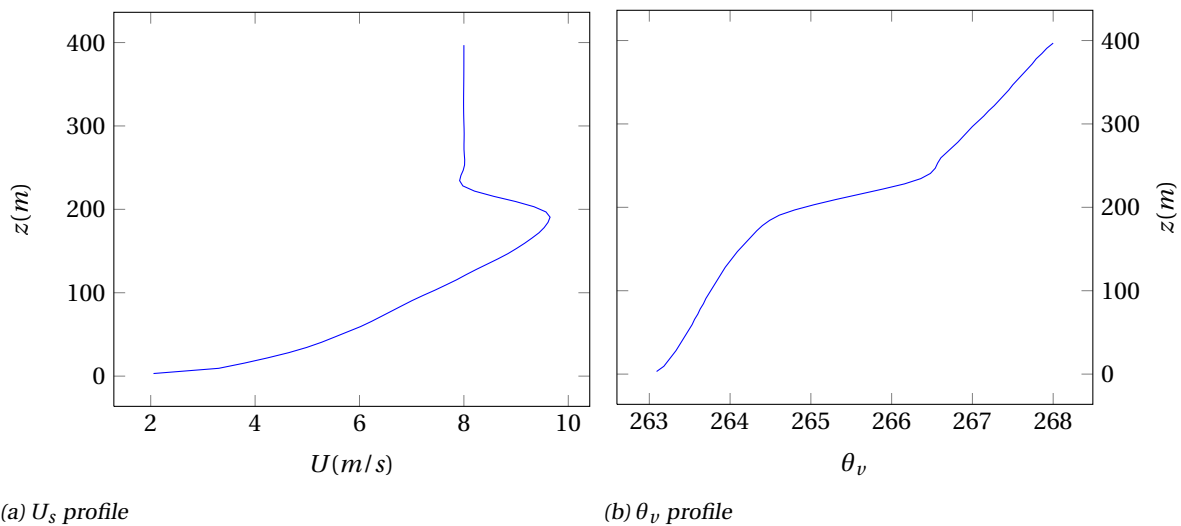
Figure E.1: Profiles high resolution GABLS case
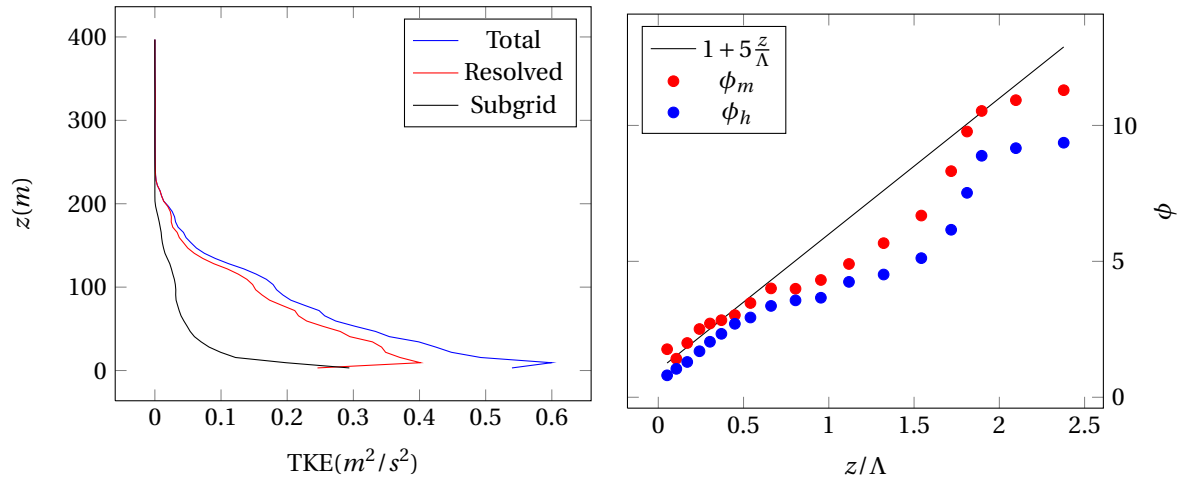
(a) TKE profiles, high resolution

(b) Similarity functions, high resolution run

Figure E.2: TKE profile and similarity functions, high resolution GABLS case
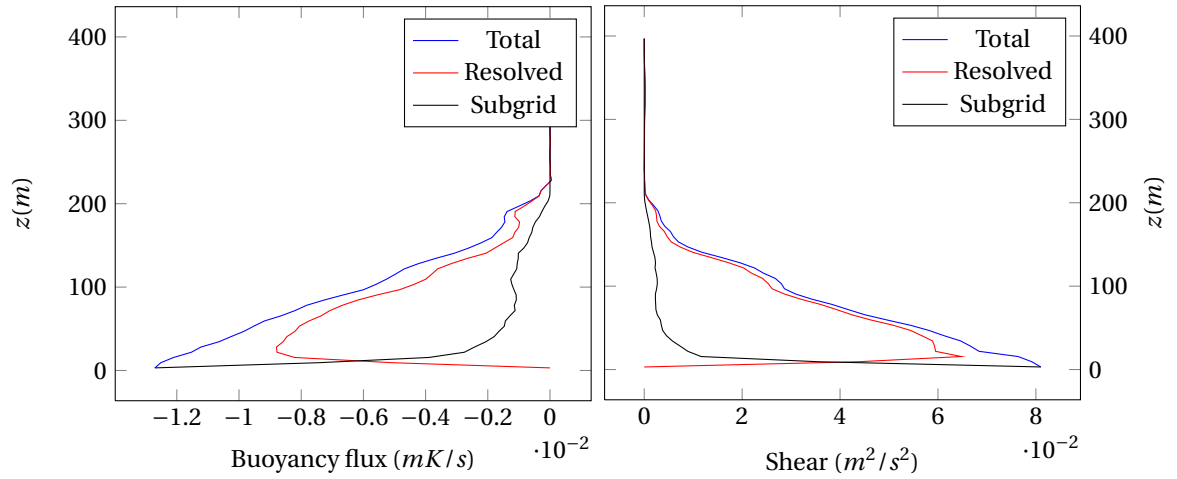
(a) Buoyancy fluxes

(b) Shear profiles

Figure E.3: Buoyancy and momentum fluxes, high resolution GABLS case

F

ORIGINAL DALES MODEL AND ADAPTATIONS

In presenting the similarity functions in the different DALES models, some data point around the height of the nocturnal jet are omitted. Because the fluxes are very small here, the Monin-Obukhov length or similarity functions can blow up or become negative due to rounding errors, yielding uninterpretable plots. For this reason, only data point at a lower height have been presented. Especially the anisotropic DALES model suffered from this effect.

F.1. ORIGINAL DALES

The results of the original DALES code, of which the important details are described in 2.1. Further information can be found in [3].
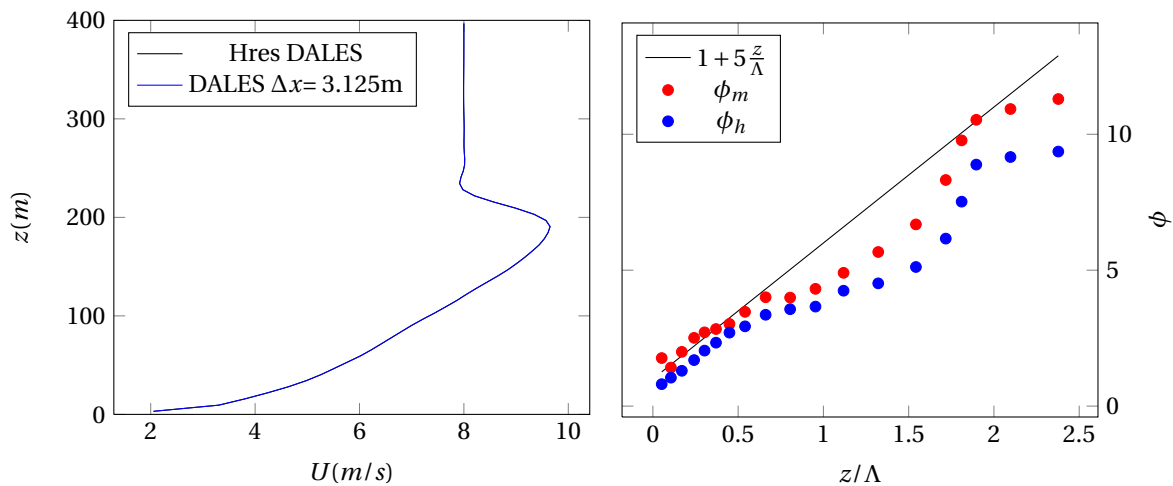
(a) U_s profile, $\Delta x = 3.125m$

(b) Similarity functions, $\Delta x = 3.125m$

Figure F.1: U_s profile and similarity functions, DALES with $\Delta x = 3.125m$
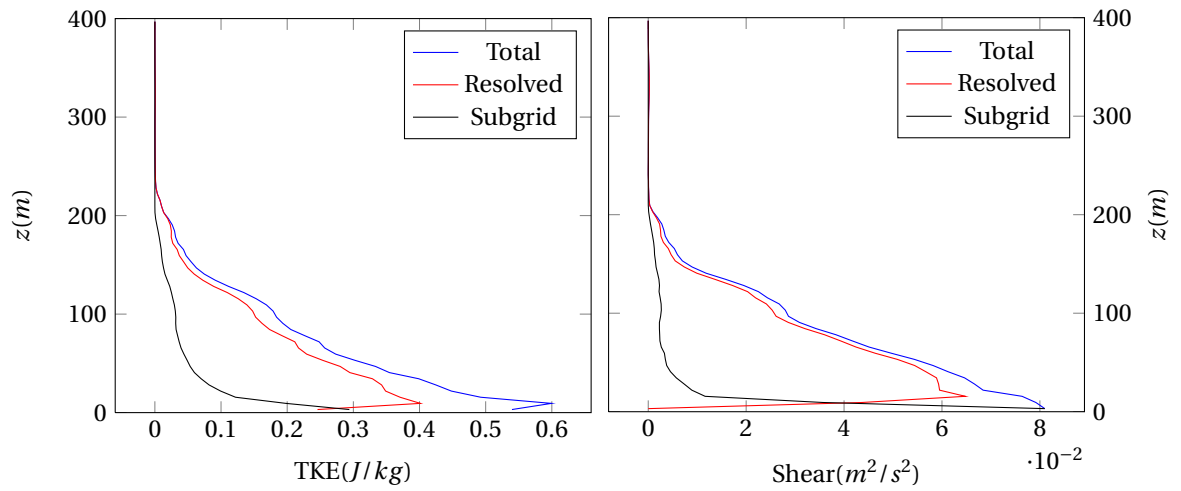
(a) TKE profiles, Δx 3.125m

(b) Shear profiles, Δx 3.125m
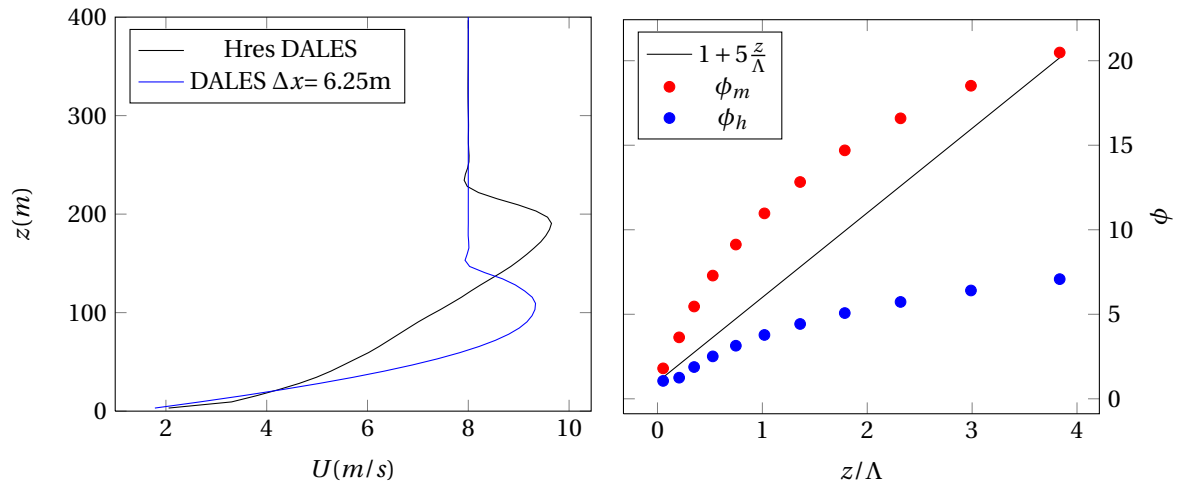
Figure F.2: TKE and shear profile, DALES with Δx = 3.125m

(a) U_s profile, Δx = 6.25m

(b) Similarity functions, Δx = 6.25m

Figure F.3: U_s profile and similarity functions, DALES with Δx = 6.25m

(a) TKE profiles, Δx 6.25m

(b) Shear profiles, Δx 6.25m
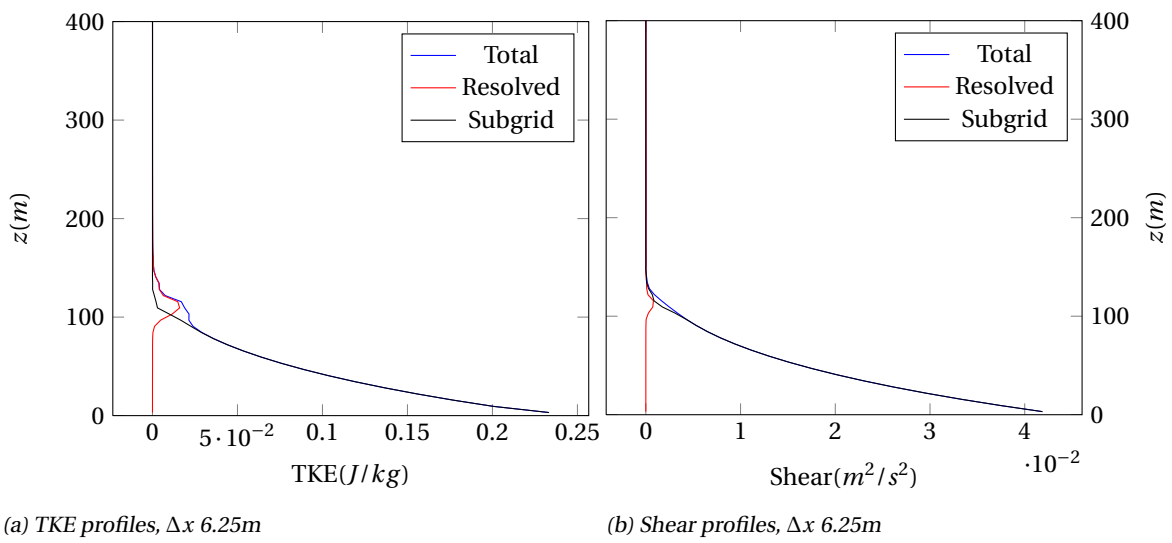
Figure F.4: TKE and shear profile, DALES with Δx = 6.25m

(a) U_s profile, Δx = 12.5m

(b) Similarity functions, Δx = 12.5m
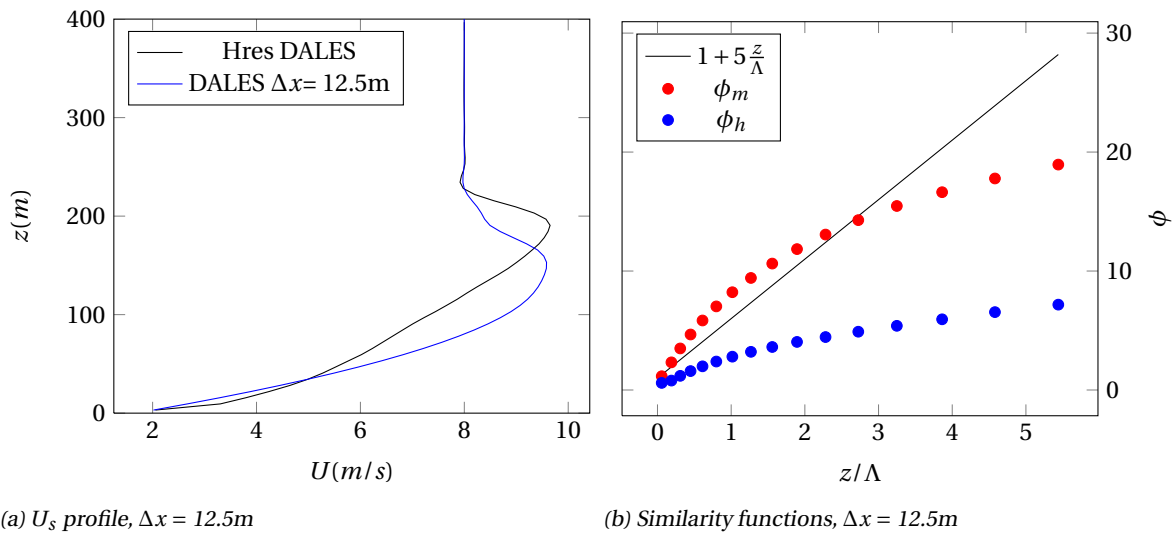
Figure F.5: U_s profile and similarity functions, DALES with Δx = 12.5m

(a) TKE profiles, Δx 12.5m

(b) Shear profiles, Δx 12.5m

Figure F.6: TKE and shear profile, DALES with Δx = 12.5m

(a) U_s profile, Δx = 25m

(b) Similarity functions, Δx = 25m

Figure F.7: U_s profile and similarity functions, DALES with Δx = 25m

(a) TKE profiles, Δx 25m

(b) Shear profiles, Δx 25m

Figure F.8: TKE and shear profile, DALES with Δx = 25m
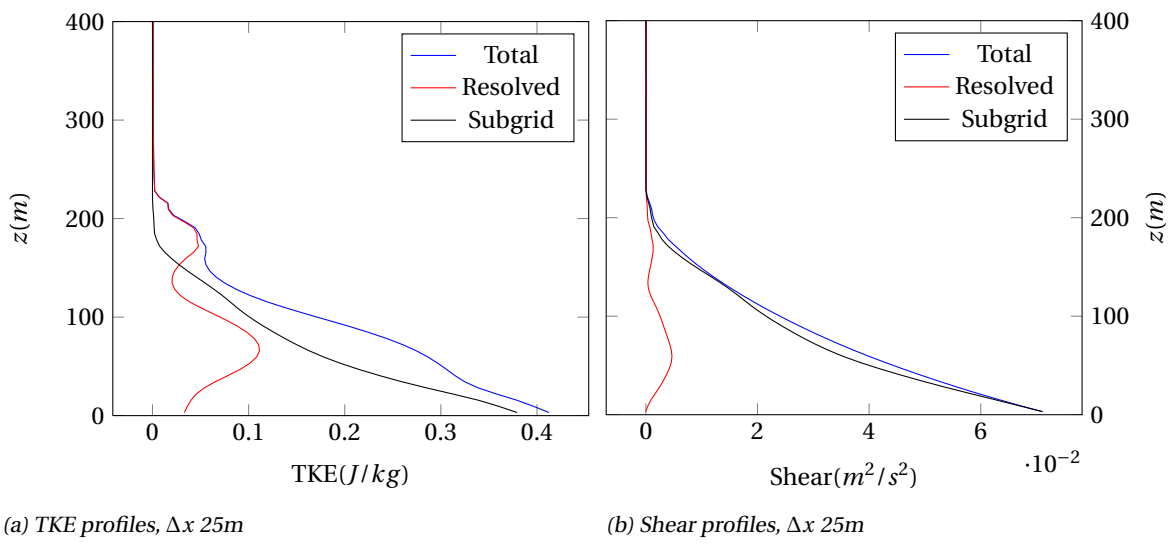
(a) U_s profile, Δx = 50m

(b) Similarity functions, Δx = 50m
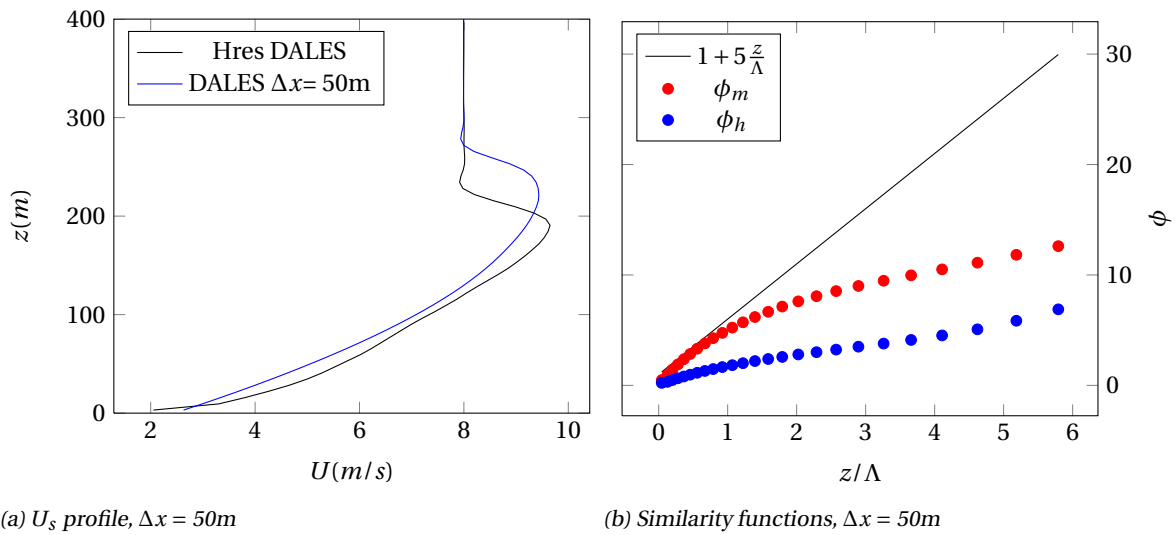
Figure F.9: U_s profile and similarity functions, DALES with Δx = 50m
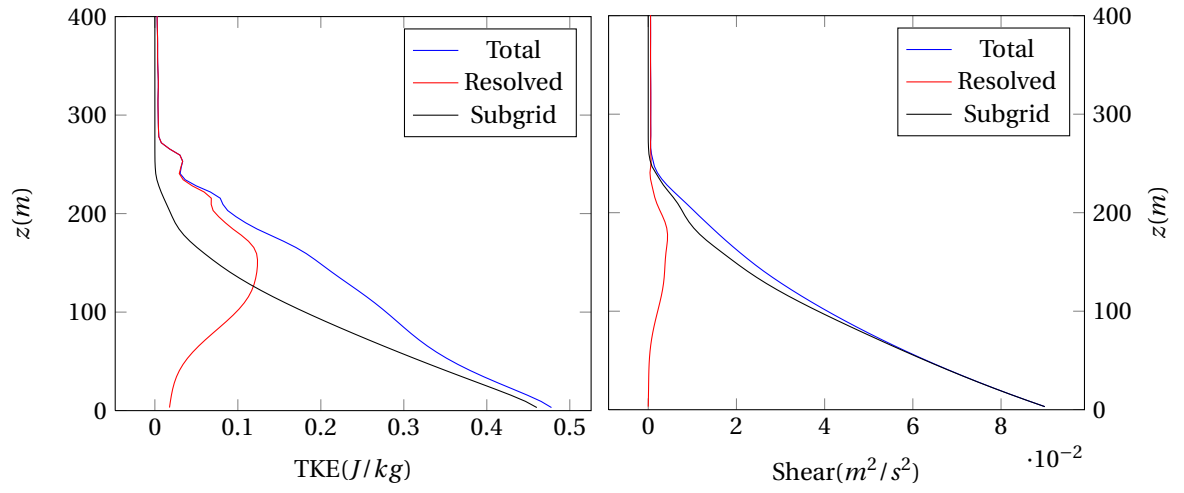
(a) TKE profiles, Δx 50m

(b) Shear profiles, Δx 50m

Figure F.10: TKE and shear profile, DALES with Δx = 50m

(a) U_s profile, Δx = 100m

(b) Similarity functions, Δx = 100m

Figure F.11: U_s profile and similarity functions, DALES with Δx = 100m

(a) TKE profiles, Δx 100m

(b) Shear profiles, Δx 100m

Figure F.12: TKE and shear profile, DALES with Δx = 100m

(a) U_s profile, Δx = 200m

(b) Similarity functions, Δx = 200m

Figure F.13: U_s profile and similarity functions, DALES with Δx = 200m

(a) TKE profiles, Δx 200m

(b) Shear profiles, Δx 200m

Figure F.14: TKE and shear profile, DALES with Δx = 200m

F.2. DALES WITH ADAPTED SUBGRID COEFFICIENTS

In this variant of the DALES code, adaptations are made in such a way that the subgrid model constants $c_{h,\epsilon}$ do not depend any more on the grid size Δ, yielding $Pr_t = 1$. They are now given by:

$$c_h = (c_{h,1})c_m$$

$$c_\epsilon = c_{\epsilon,1} + c_{\epsilon,2}$$

(a) U_s profile, Δx = 6.25m

(b) Similarity functions, Δx = 6.25m

Figure F.15: U_s profile and similarity functions, DALES with adapted $c_{h,\epsilon}$, with Δx = 6.25m

(a) TKE profiles, Δx 6.25m

(b) Shear profiles, Δx 6.25m

Figure F.16: TKE and shear profile, DALES with adapted $c_{h,\epsilon}$, with $\Delta x = 6.25m$

(a) U_s profile, Δx = 12.5m

(b) Similarity functions, Δx = 12.5m

Figure F.17: U_s profile and similarity functions, DALES with adapted $c_{h,\epsilon}$, with $\Delta x = 12.5m$

(a) TKE profiles, Δx 12.5m
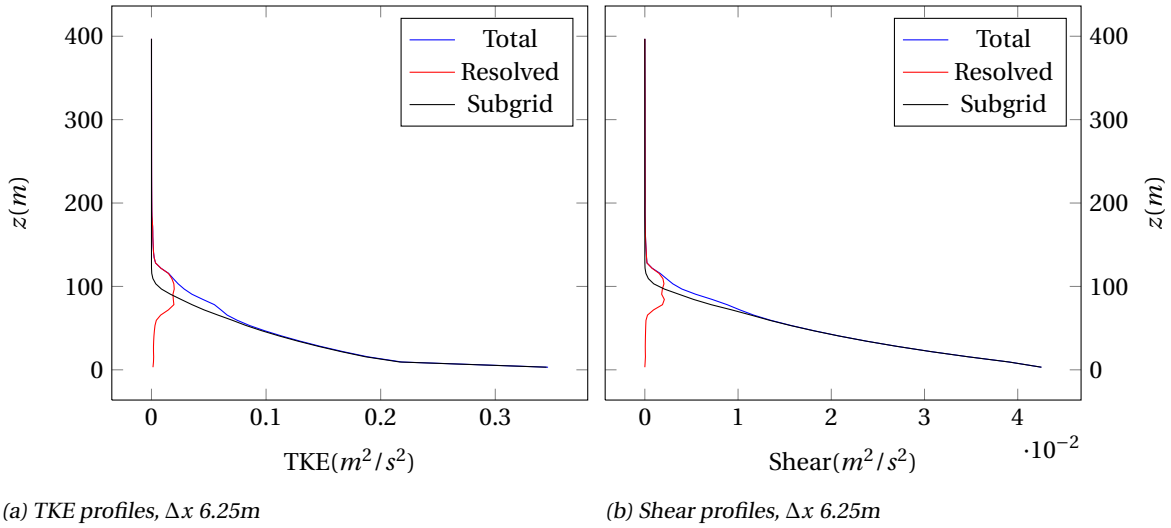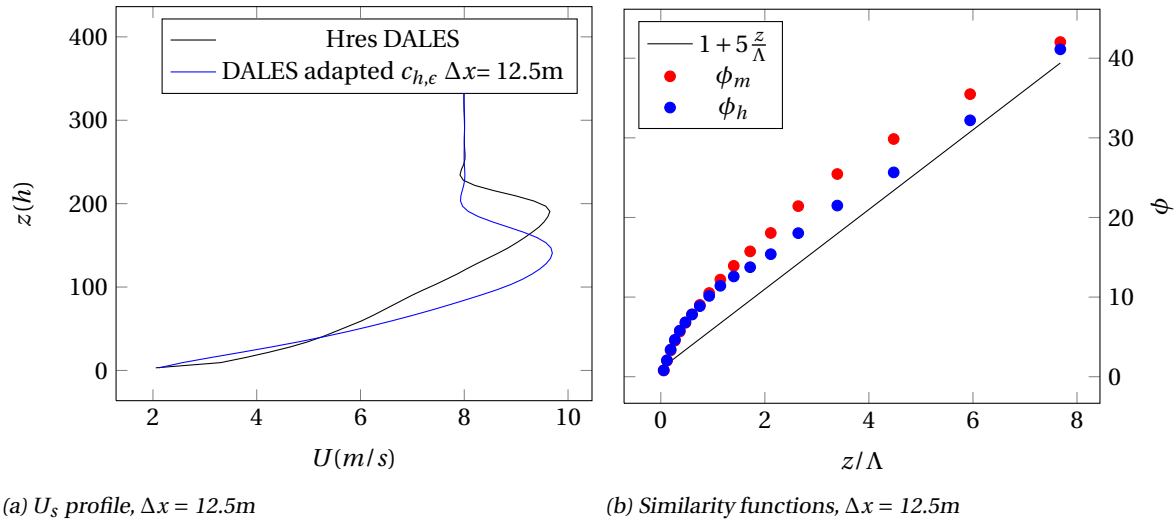
(b) Shear profiles, Δx 12.5m
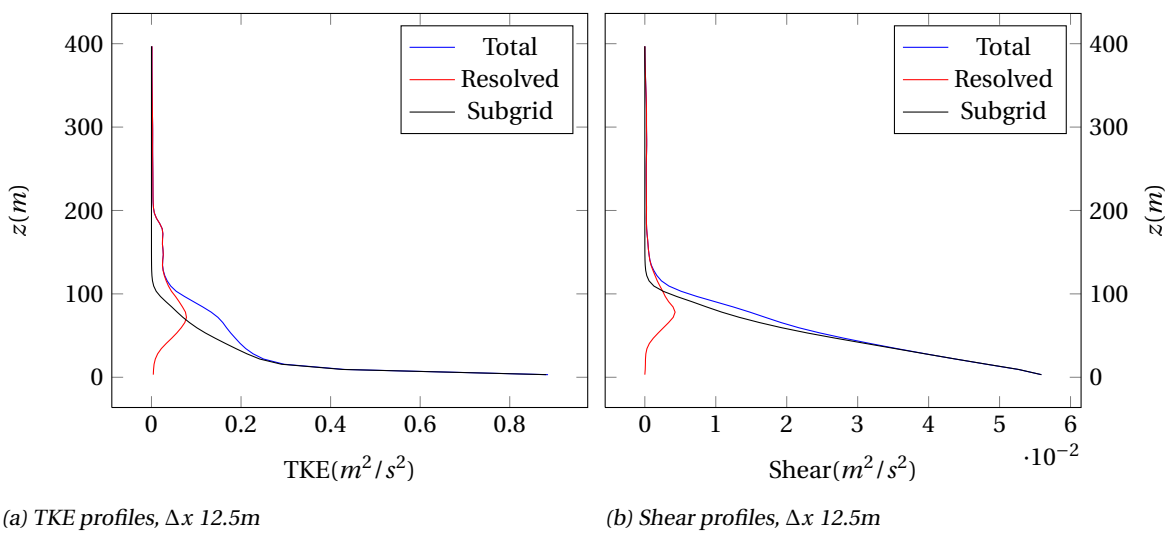
Figure F.18: TKE and shear profile, DALES with adapted $c_{h,\epsilon}$, with $\Delta x = 12.5m$
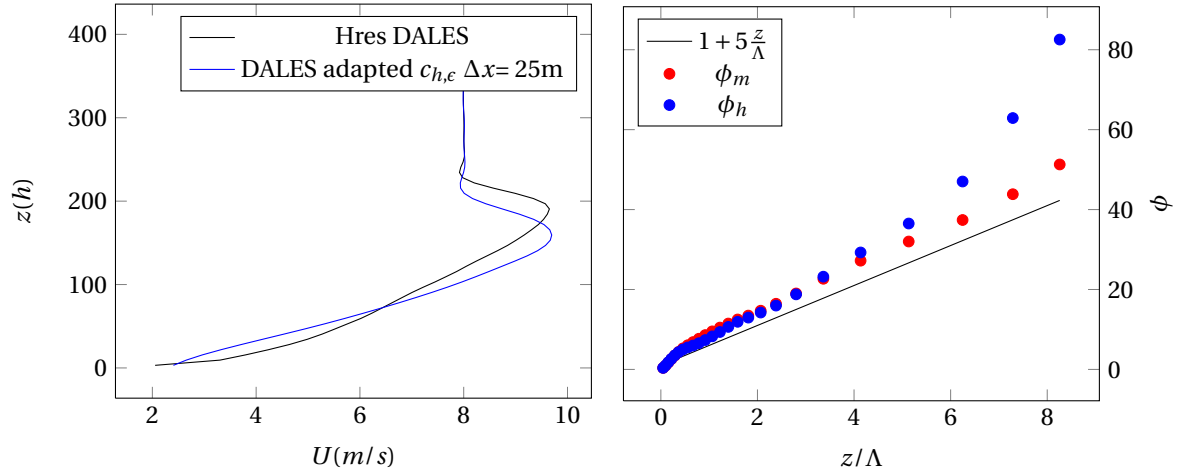
(a) U_s profile, $\Delta x = 25m$

(b) Similarity functions, $\Delta x = 25m$

Figure F.19: U_s profile and similarity functions, DALES with adapted $c_{h,\epsilon}$, with $\Delta x = 25m$

(a) TKE profiles, Δx 25m

(b) Shear profiles, Δx 25m

Figure F.20: TKE and shear profile, DALES with adapted $c_{h,\epsilon}$, with $\Delta x = 25m$

(a) U_s profile, $\Delta x = 50m$

(b) Similarity functions, $\Delta x = 50m$

Figure F.21: U_s profile and similarity functions, DALES with adapted $c_{h,\epsilon}$, with $\Delta x = 50m$

(a) TKE profiles, Δx 50m

(b) Shear profiles, Δx 50m

Figure F.22: TKE and shear profile, DALES with adapted $c_{h,\epsilon}$, with $\Delta x = 50m$

(a) U_s profile, $\Delta x = 100m$

(b) Similarity functions, $\Delta x = 100m$

Figure F.23: U_s profile and similarity functions, DALES with adapted $c_{h,\epsilon}$, with $\Delta x = 100m$

(a) TKE profiles, Δx 100m
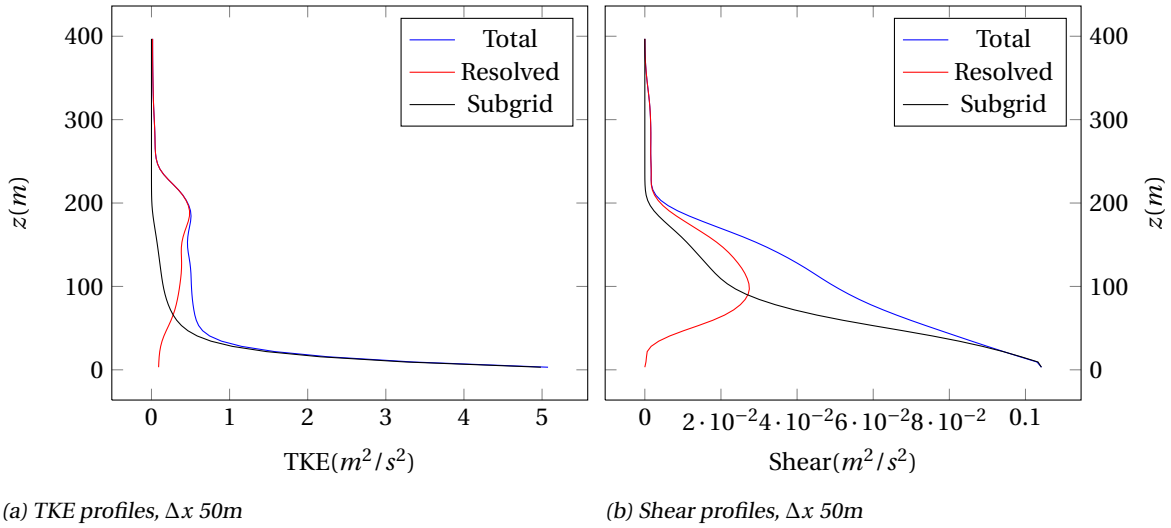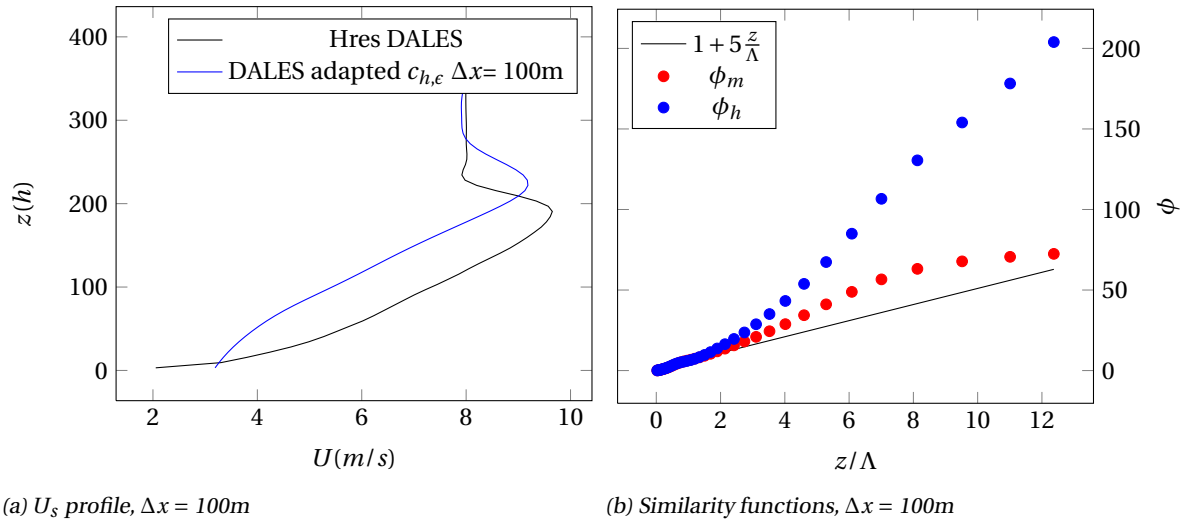
(b) Shear profiles, Δx 100m
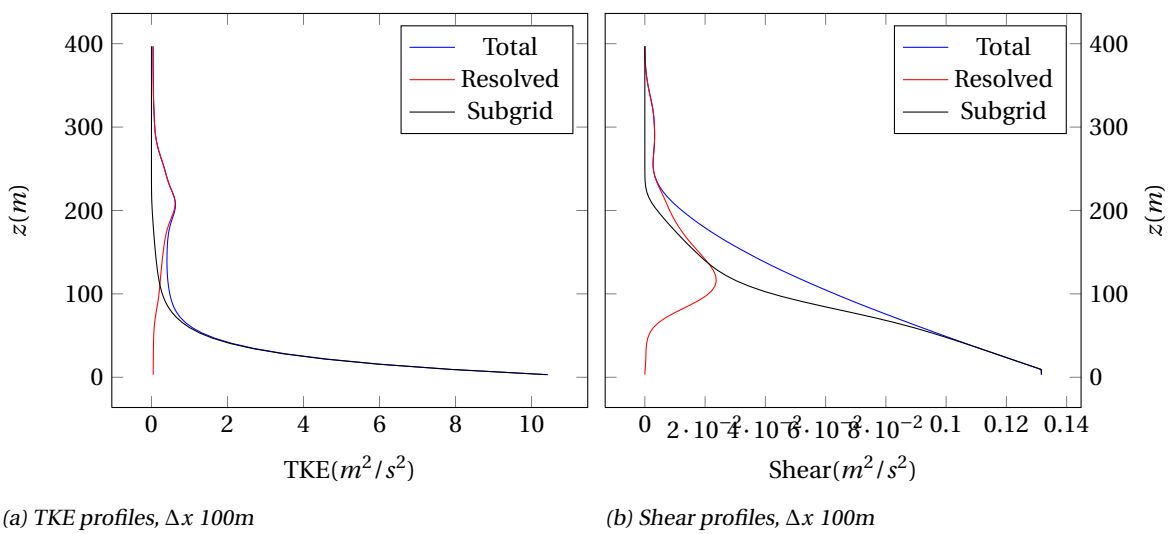
Figure F.24: TKE and shear profile, DALES with adapted $c_{h,\epsilon}$, with $\Delta x = 100m$

(a) U_s profile, $\Delta x = 200m$

(b) Similarity functions, $\Delta x = 200m$

Figure F.25: U_s profile and similarity functions, DALES with adapted $c_{h,\epsilon}$, with $\Delta x = 200m$
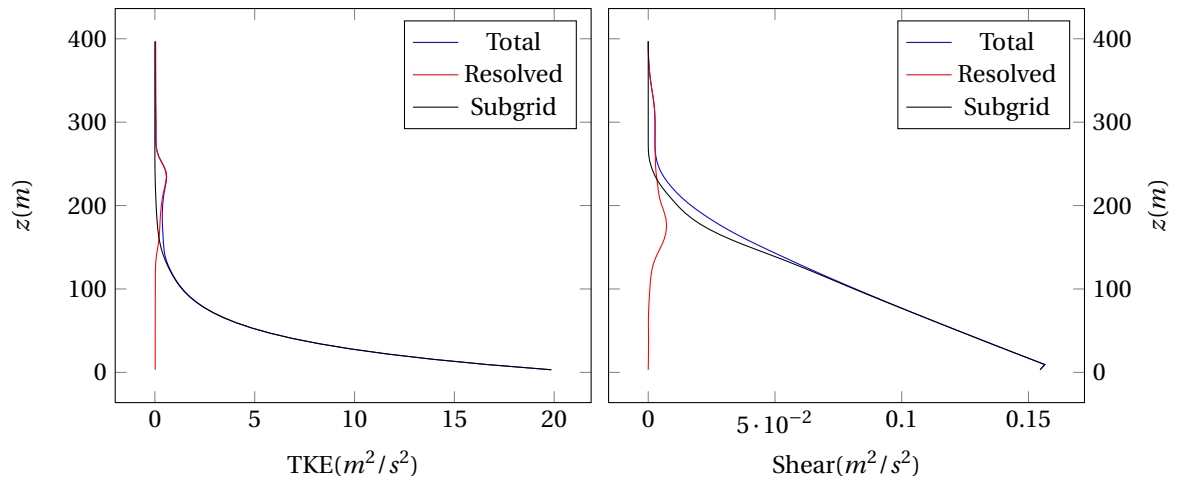
(a) TKE profiles, $\Delta x\ 200m$

(b) Shear profiles, $\Delta x\ 200m$

Figure F.26: TKE and shear profile, DALES with adapted $c_{h,\epsilon}$, with $\Delta x = 200m$

F.3. DALES WITH ANISOTROPIC EDDY DIFFUSIVITIES

In this model, the $K_{m,h}$ coefficients are made different for eddy diffusion in the three different directions (x, y, z). This is done by changing the definition of $\Delta = \Delta z$. When there is diffusion in horizontal direction, the substitution $K_{m,h} = \frac{\Delta x \Delta y}{(\Delta z)^2}$ in done.
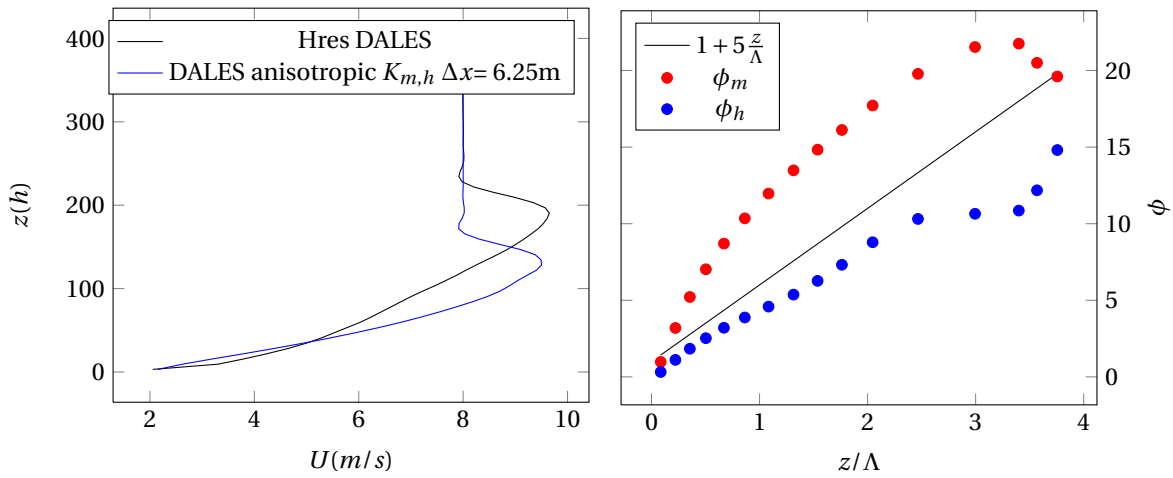
(a) U_s profile, $\Delta x = 6.25m$

(b) Similarity functions, $\Delta x = 6.25m$

Figure F.27: U_s profile and similarity functions, DALES with anisotropic $K_{m,h}$, with $\Delta x = 6.25m$
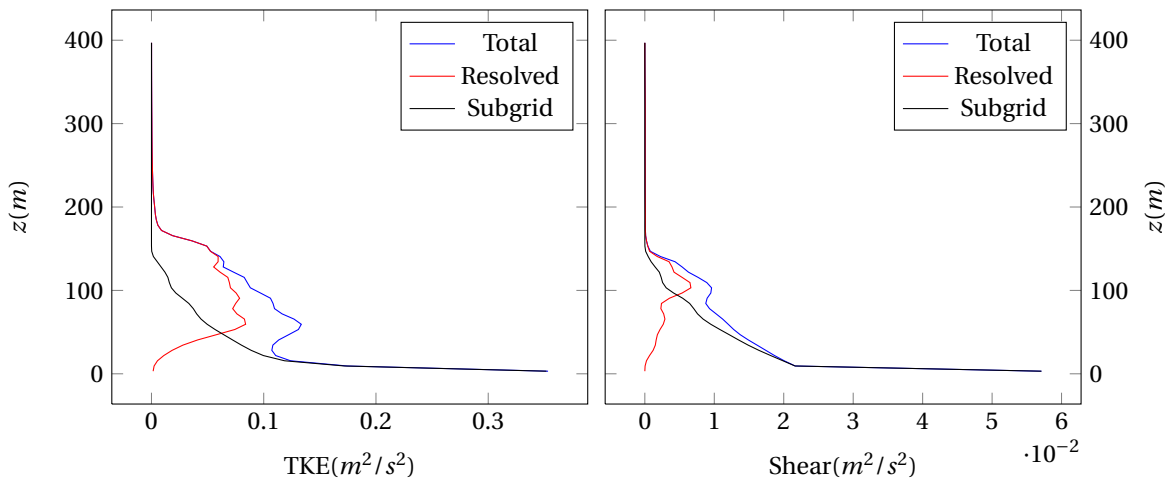
(a) TKE profiles, Δx 6.25m

(b) Shear profiles, Δx 6.25m

Figure F.28: TKE and shear profile, DALES with anisotropic $K_{m,h}$, with $\Delta x = 6.25m$
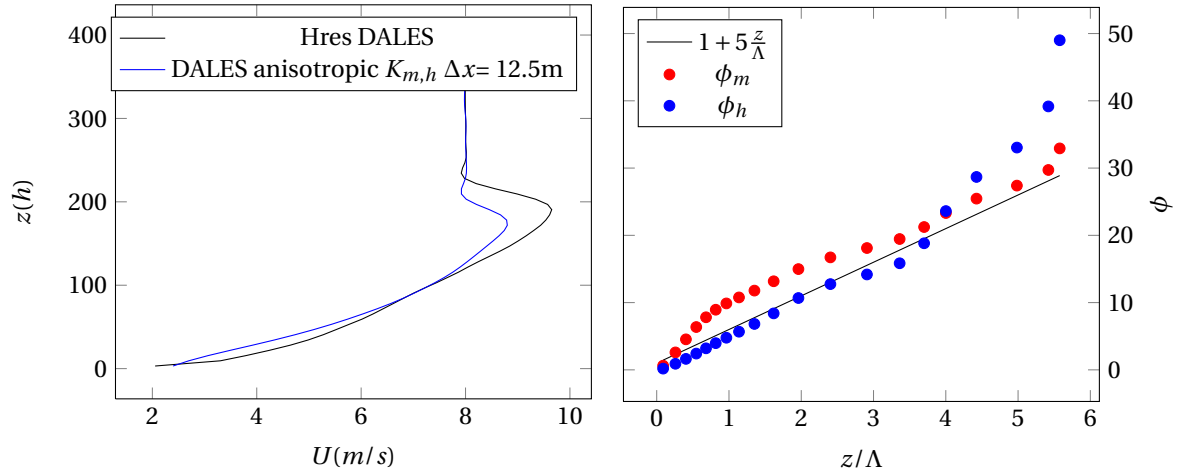
(a) U_s profile, $\Delta x = 12.5m$

(b) Similarity functions, $\Delta x = 12.5m$

Figure F.29: U_s profile and similarity functions, DALES with anisotropic $K_{m,h}$, with $\Delta x = 12.5m$
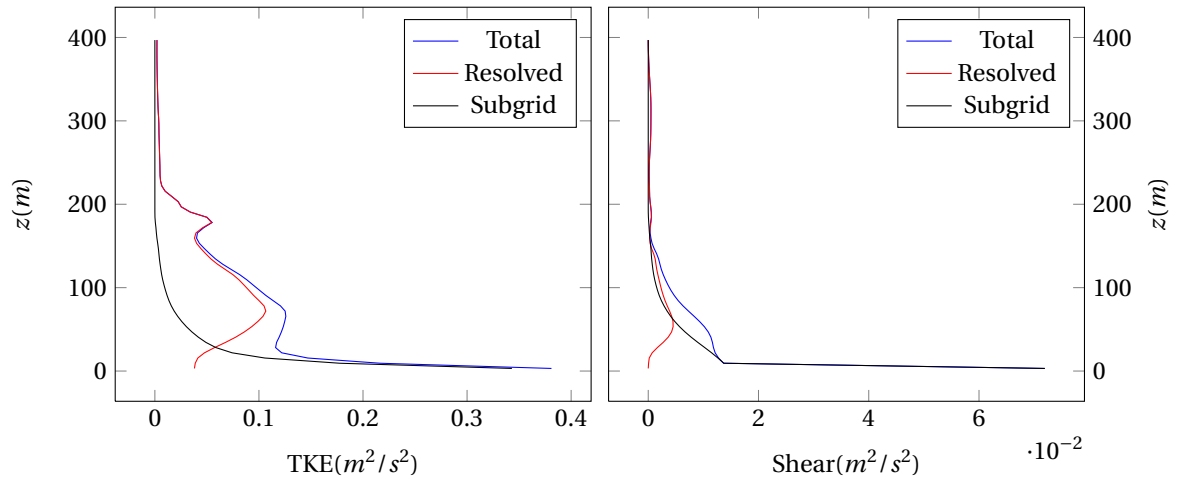
(a) TKE profiles, Δx 12.5m

(b) Shear profiles, Δx 12.5m

Figure F.30: TKE and shear profile, DALES with anisotropic $K_{m,h}$, with $\Delta x = 12.5m$
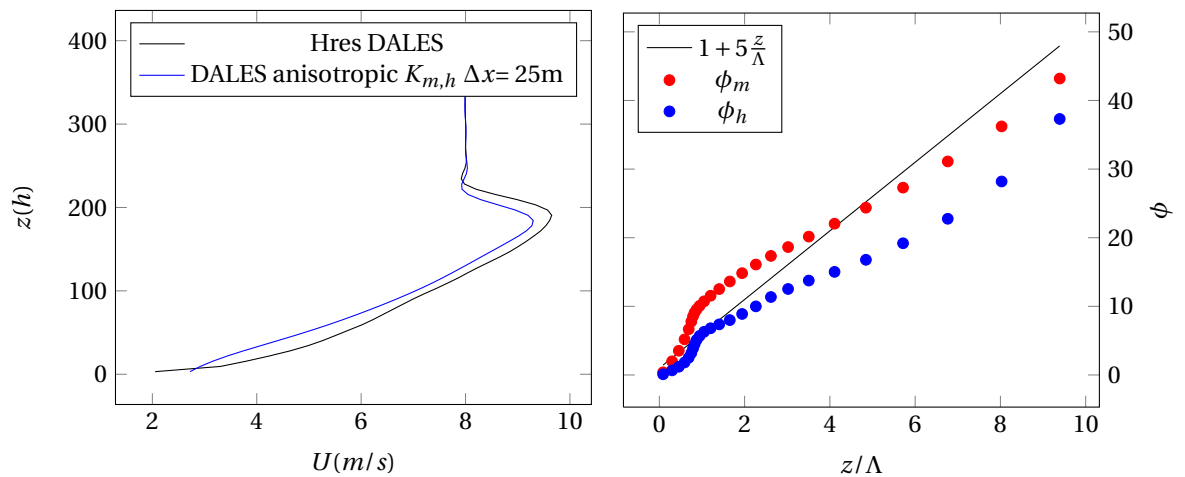
(a) U_s profile, $\Delta x = 25m$

(b) Similarity functions, $\Delta x = 25m$

Figure F.31: U_s profile and similarity functions, DALES with anisotropic $K_{m,h}$, with $\Delta x = 25m$
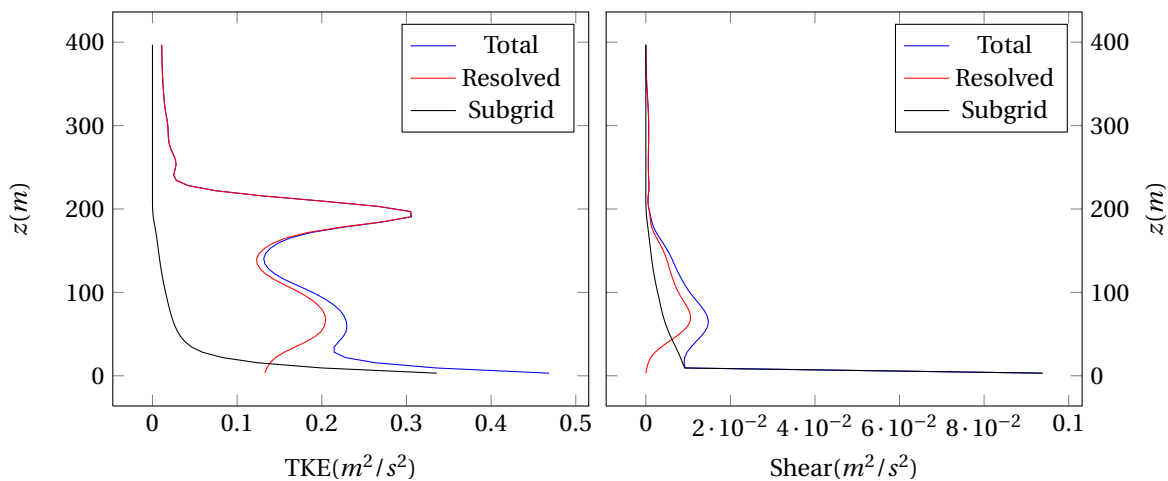
(a) TKE profiles, Δx 25m

(b) Shear profiles, Δx 25m

Figure F.32: TKE and shear profile, DALES with anisotropic $K_{m,h}$, with $\Delta x = 25m$
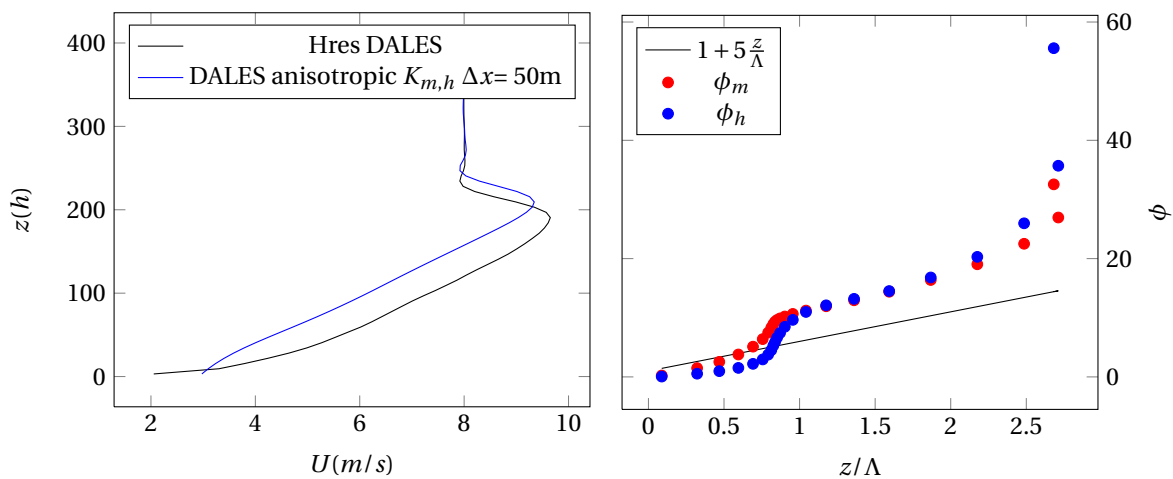
(a) U_s profile, $\Delta x = 50m$

(b) Similarity functions, $\Delta x = 50m$

Figure F.33: U_s profile and similarity functions, DALES with anisotropic $K_{m,h}$, with $\Delta x = 50m$
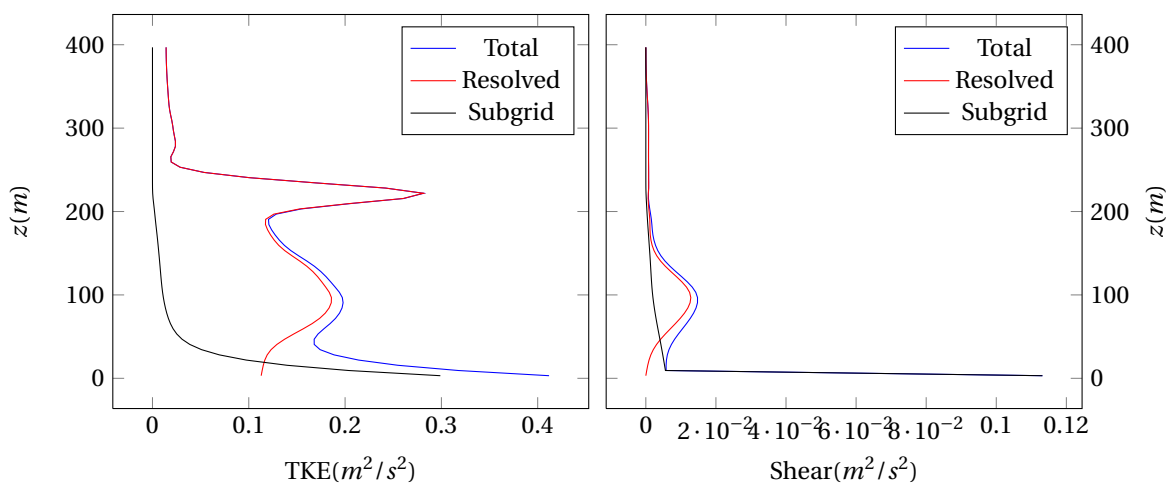
(a) TKE profiles, Δx 50m

(b) Shear profiles, Δx 50m

Figure F.34: TKE and shear profile, DALES with anisotropic $K_{m,h}$, with $\Delta x = 50m$
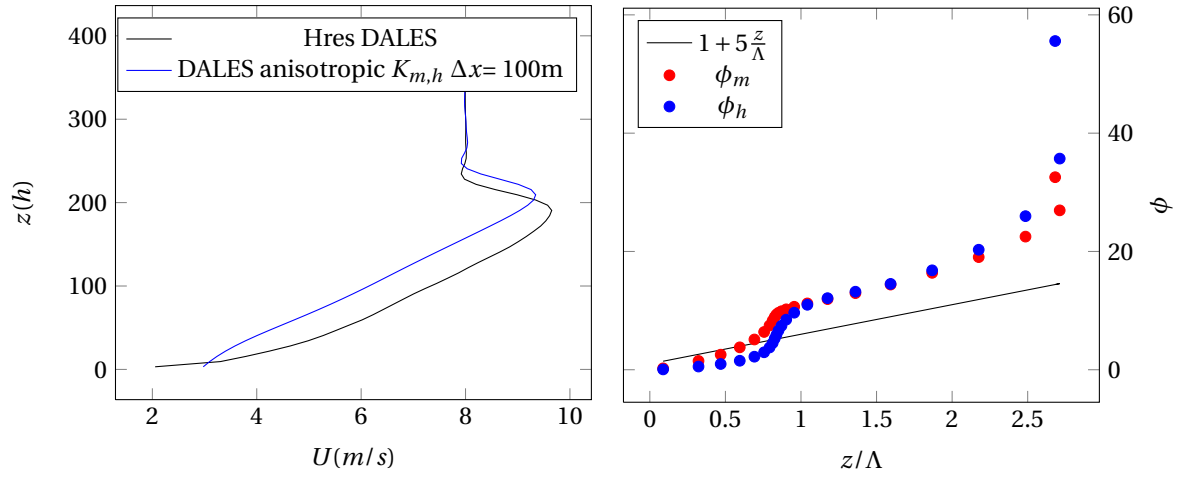
(a) U_s profile, $\Delta x = 100m$

(b) Similarity functions, $\Delta x = 100m$

Figure F.35: U_s profile and similarity functions, DALES with anisotropic $K_{m,h}$, with $\Delta x = 100m$
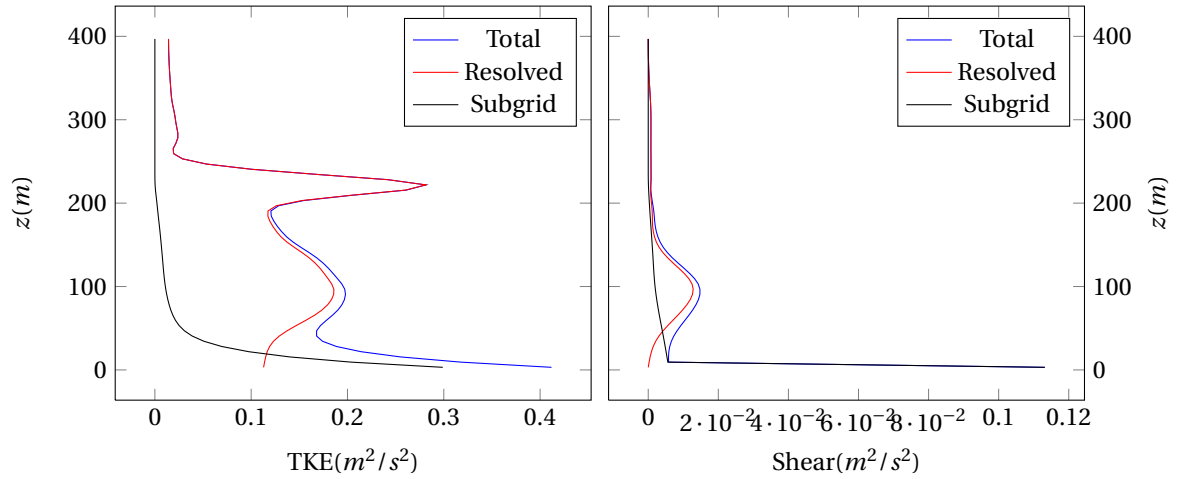
(a) TKE profiles, Δx 100m

(b) Shear profiles, Δx 100m

Figure F.36: TKE and shear profile, DALES with anisotropic $K_{m,h}$, with $\Delta x = 100m$

G

SULLIVAN'S MODEL AND ADAPTATIONS

G.1. ORIGINAL SULLIVAN MODEL
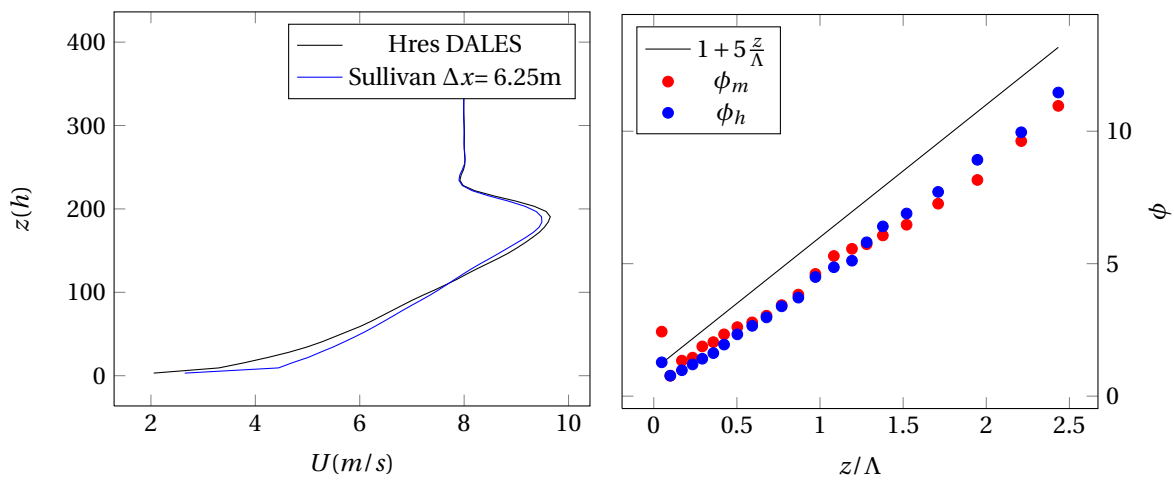
(a) U_s profile, $\Delta x = 6.25m$

(b) Similarity functions, $\Delta x = 6.25m$

Figure G.1: U_s profile and similarity functions, Sullivan model with $\Delta x = 6.25m$
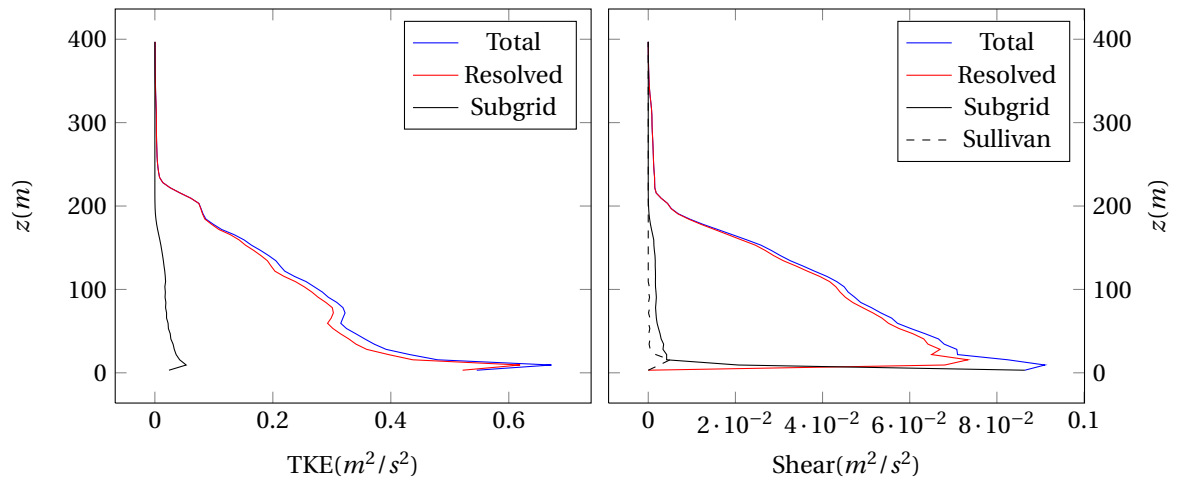
(a) TKE profiles, Δx 6.25m

(b) Shear profiles, Δx 6.25m

Figure G.2: TKE and shear profile, Sullivan model with Δx = 6.25m
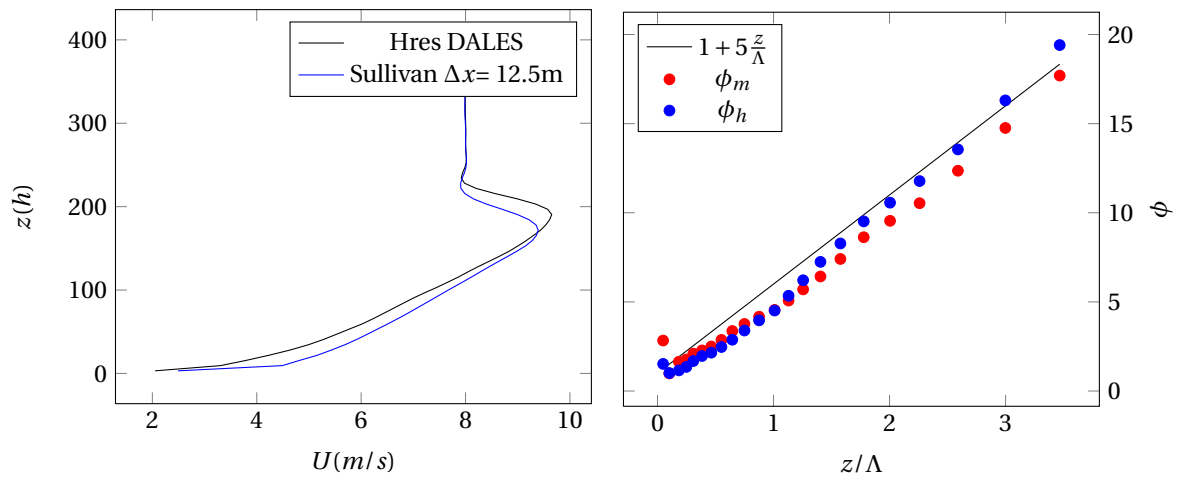
(a) U_s profile, Δx = 12.5m

(b) Similarity functions, Δx = 12.5m

Figure G.3: U_s profile and similarity functions, Sullivan model with Δx = 12.5m
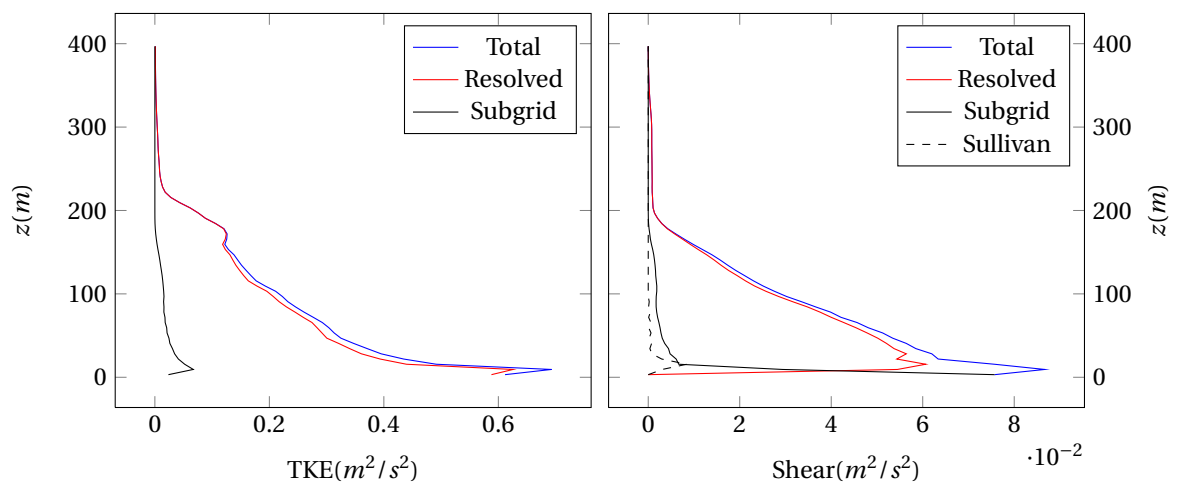
(a) TKE profiles, Δx 12.5m

(b) Shear profiles, Δx 12.5m

Figure G.4: TKE and shear profile, Sullivan model with Δx = 12.5m
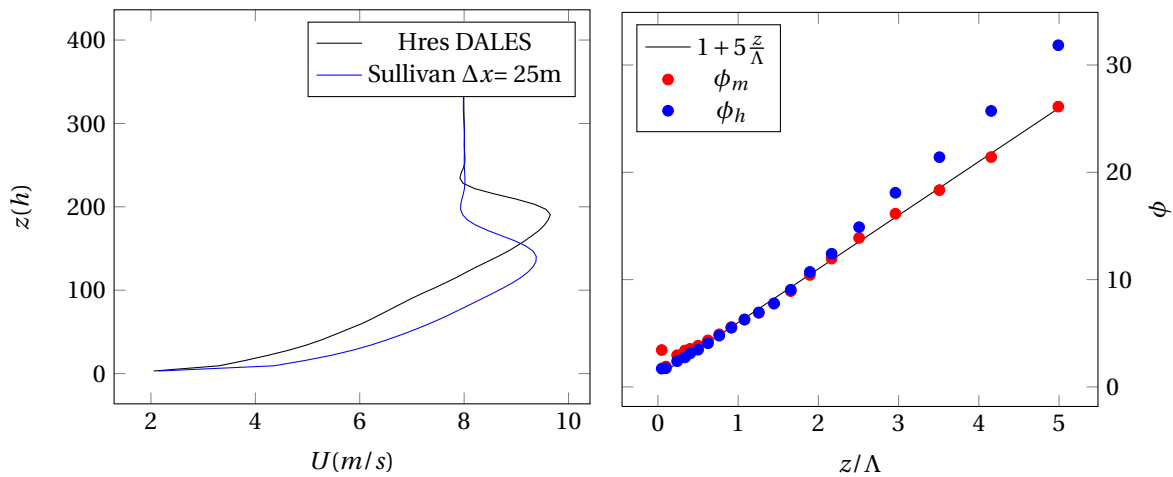
(a) U_s profile, $\Delta x = 25m$

(b) Similarity functions, $\Delta x = 25m$

Figure G.5: U_s profile and similarity functions, Sullivan model with $\Delta x = 25m$
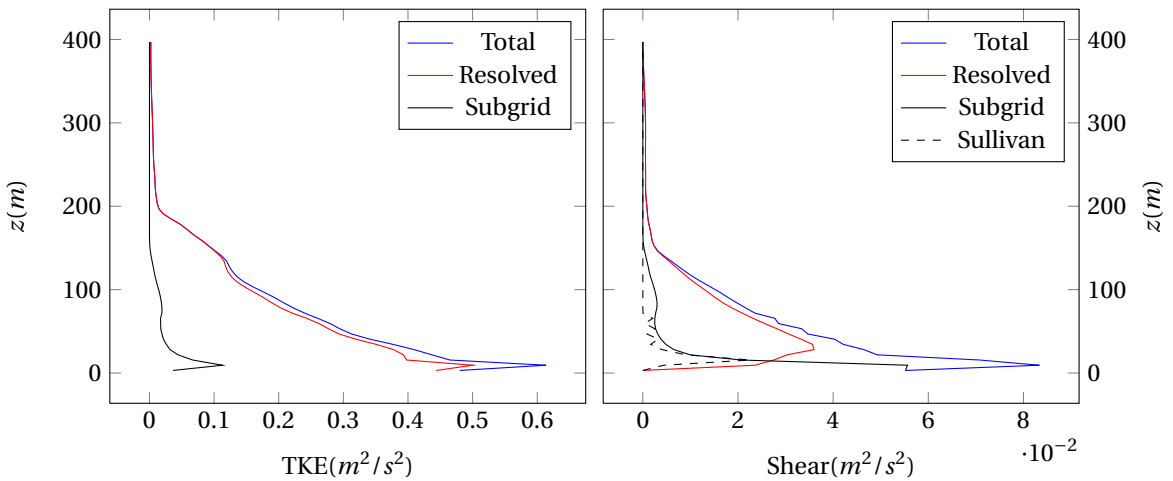
(a) TKE profiles, Δx 25m

(b) Shear profiles, Δx 25m

Figure G.6: TKE and shear profile, Sullivan model with $\Delta x = 25m$
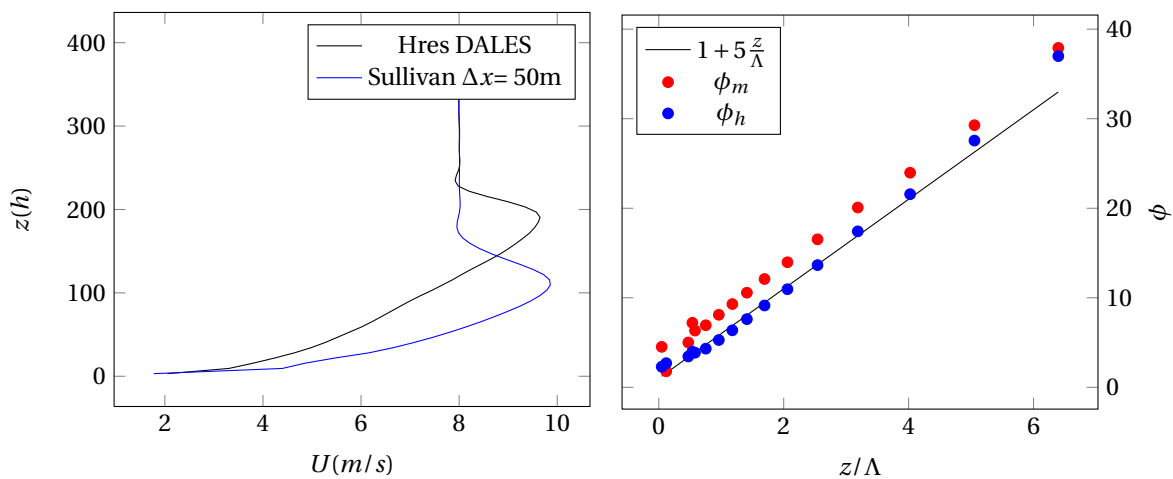
(a) U_s profile, $\Delta x = 50m$

(b) Similarity functions, $\Delta x = 50m$

Figure G.7: U_s profile and similarity functions, Sullivan model with $\Delta x = 50m$
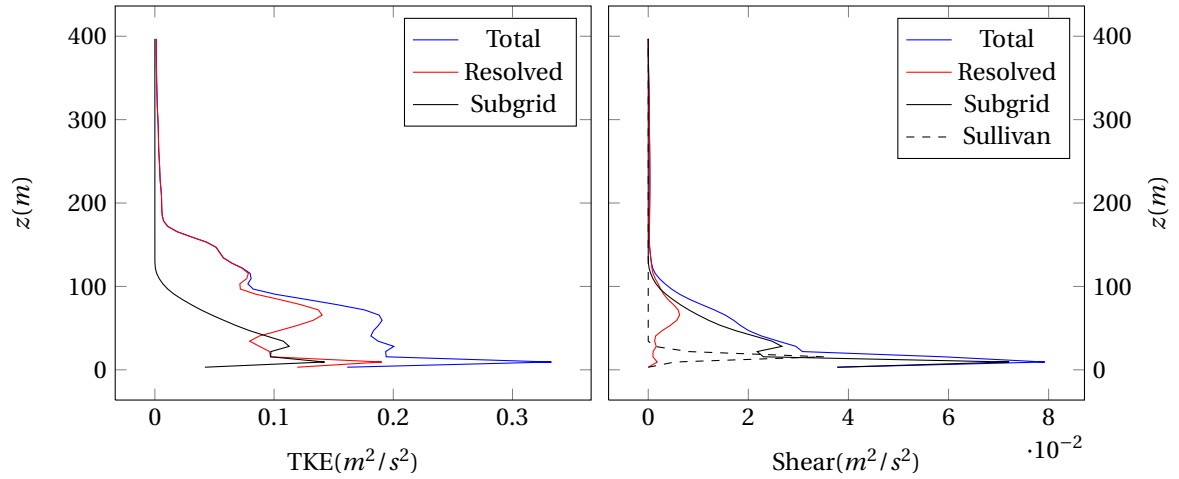
(a) TKE profiles, Δx 50m

(b) Shear profiles, Δx 50m

Figure G.8: TKE and shear profile, Sullivan model with Δx = 50m
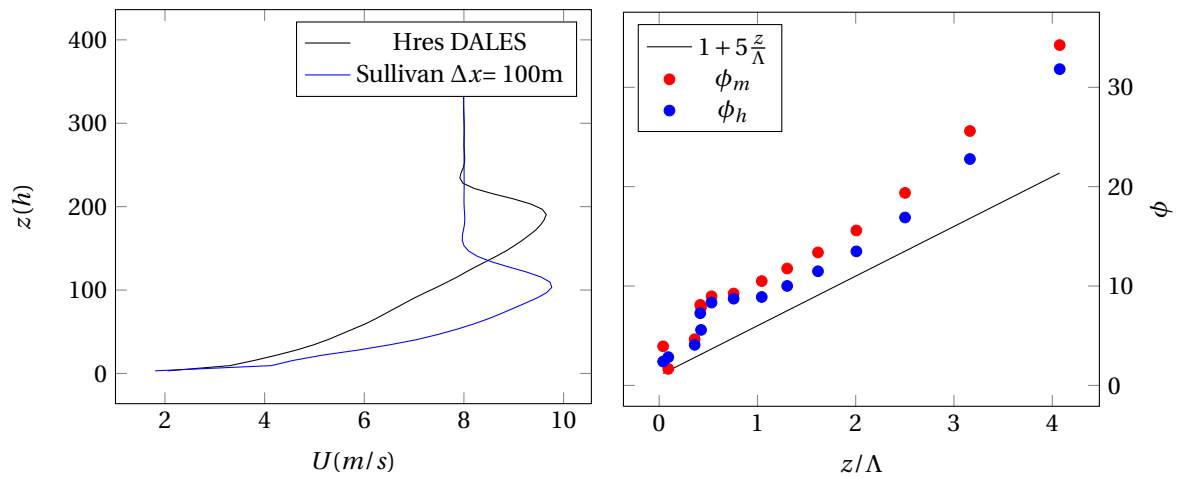
(a) U_s profile, Δx = 100m

(b) Similarity functions, Δx = 100m

Figure G.9: U_s profile and similarity functions, Sullivan model with Δx = 100m
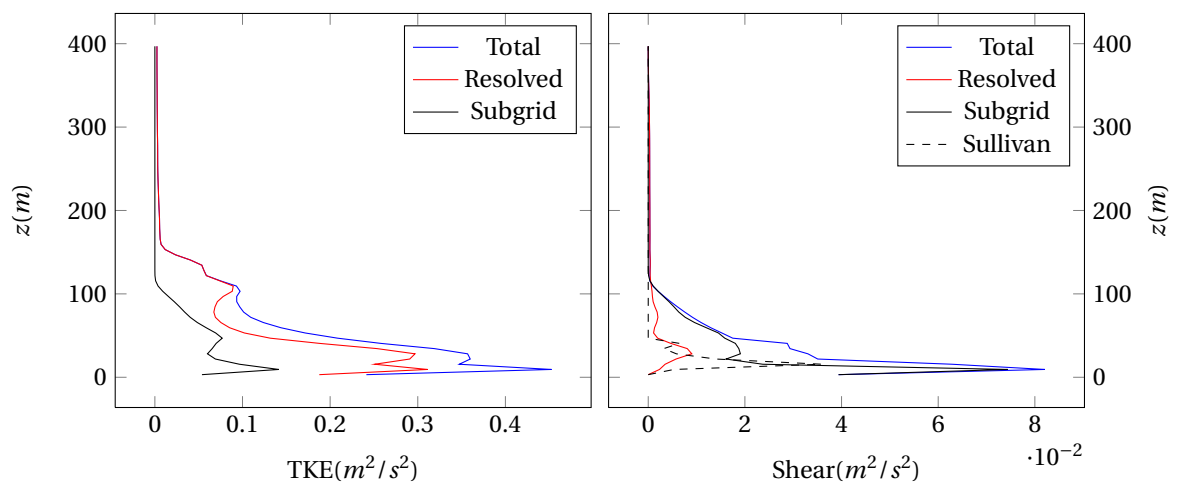
(a) TKE profiles, Δx 100m

(b) Shear profiles, Δx 100m

Figure G.10: TKE and shear profile, Sullivan model with Δx = 100m
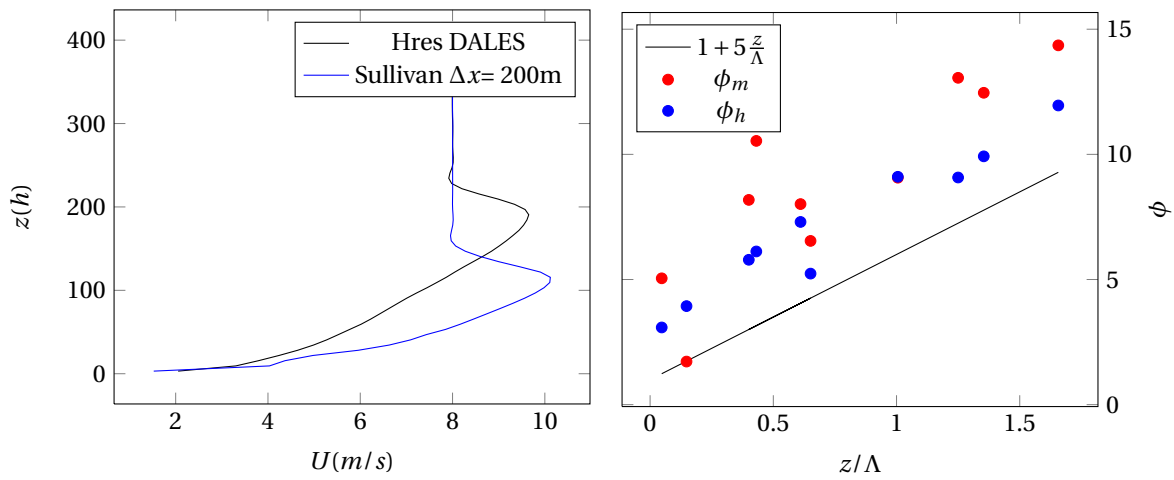
(a) U_s profile, $\Delta x = 200m$

(b) Similarity functions, $\Delta x = 200m$

Figure G.11: U_s profile and similarity functions, Sullivan model with $\Delta x = 200m$
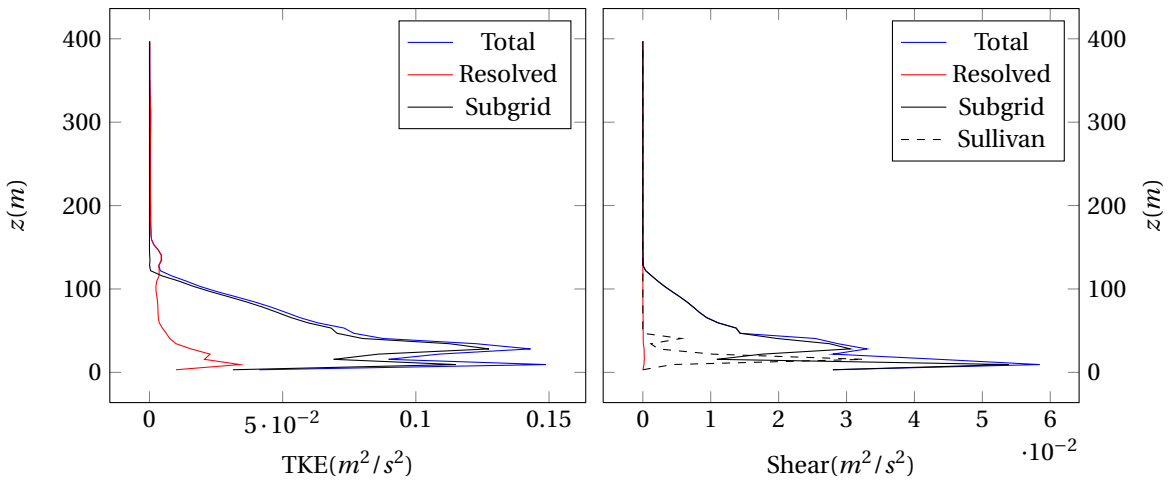
(a) TKE profiles, Δx 200m

(b) Shear profiles, Δx 200m

Figure G.12: TKE and shear profile, Sullivan model with $\Delta x = 200m$

G.2. Sullivan model with $\gamma = 1$

The Sullivan model with $\gamma = 1$ everywhere.
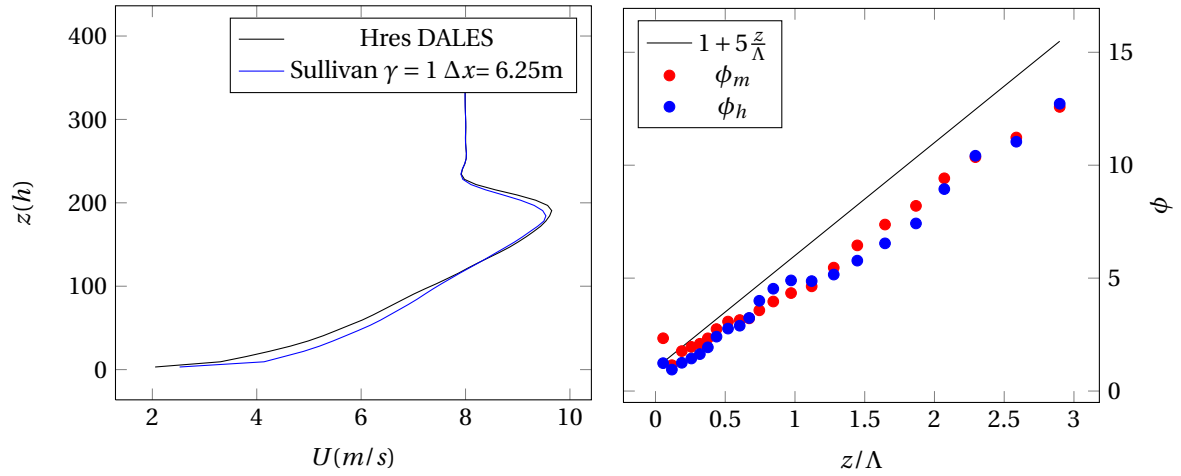
(a) U_h profile, $\Delta x = 6.25m$

(b) Similarity functions, $\Delta x = 6.25m$

Figure G.13: U_s profile and similarity functions, Sullivan model with $\gamma = 1$, with $\Delta x = 6.25m$
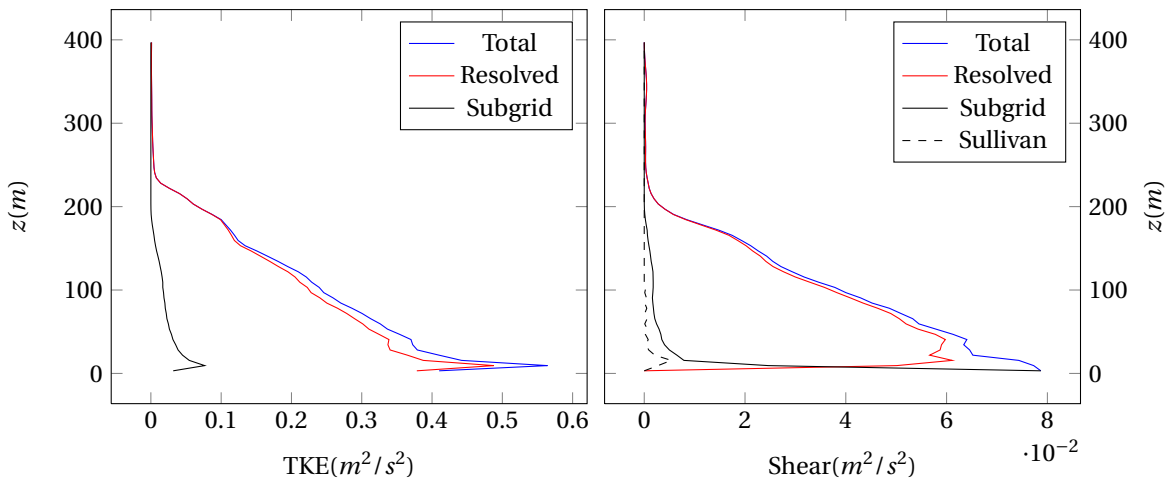
(a) TKE profiles, Δx 6.25m

(b) Shear profiles, Δx 6.25m

Figure G.14: TKE and shear profile, Sullivan model with $\gamma = 1$, with $\Delta x = 6.25m$
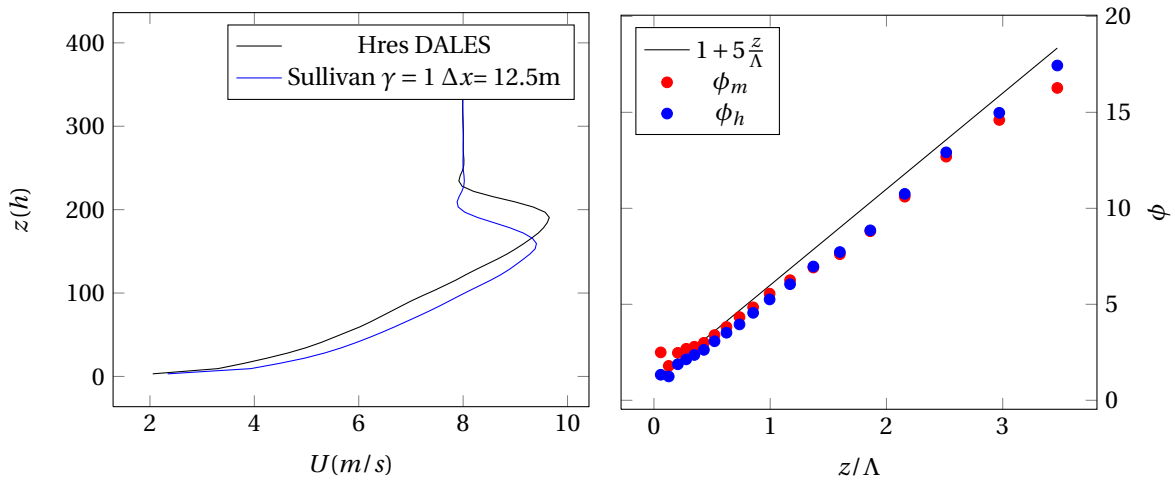
(a) $U_h profile$, $\Delta x = 12.5m$

(b) Similarity functions, $\Delta x = 12.5m$

Figure G.15: U_s profile and similarity functions, Sullivan model with $\gamma = 1$, with $\Delta x = 12.5m$
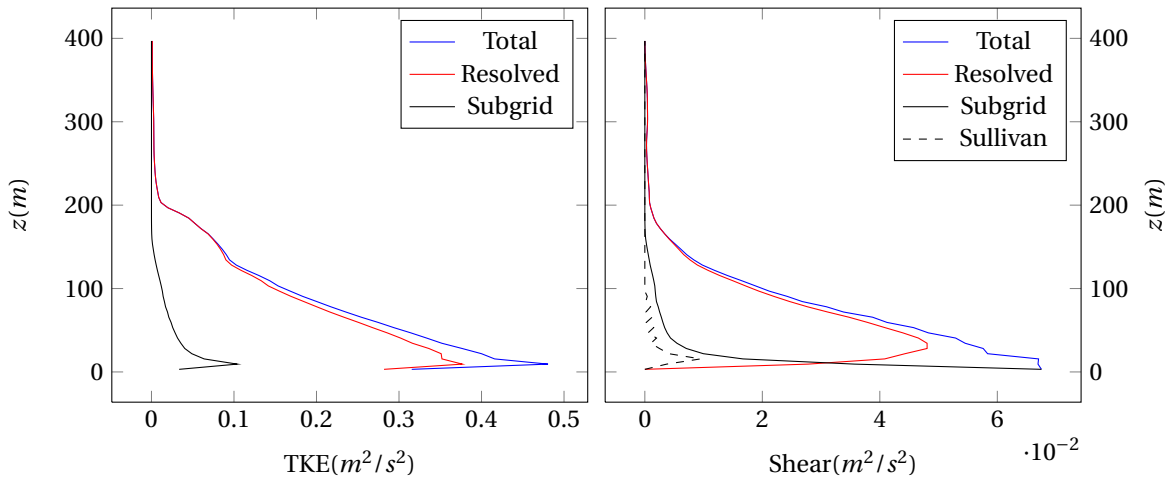
(a) TKE profiles, Δx 12.5m

(b) Shear profiles, Δx 12.5m

Figure G.16: TKE and shear profile, Sullivan model with $\gamma = 1$, with $\Delta x = 12.5m$
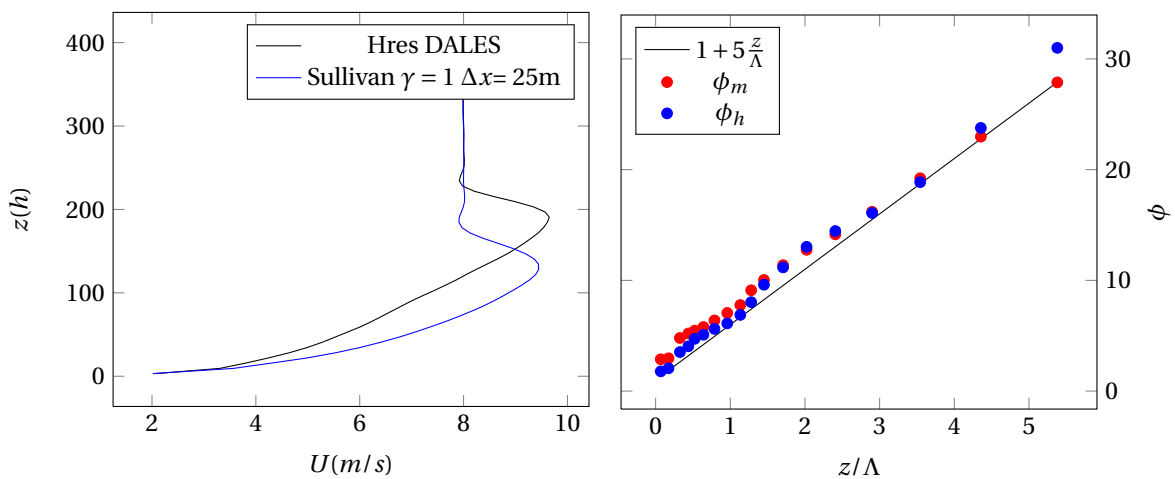
(a) $U_h profile$, $\Delta x = 25m$

(b) Similarity functions, $\Delta x = 25m$

Figure G.17: U_s profile and similarity functions, Sullivan model with $\gamma = 1$, with $\Delta x = 25m$
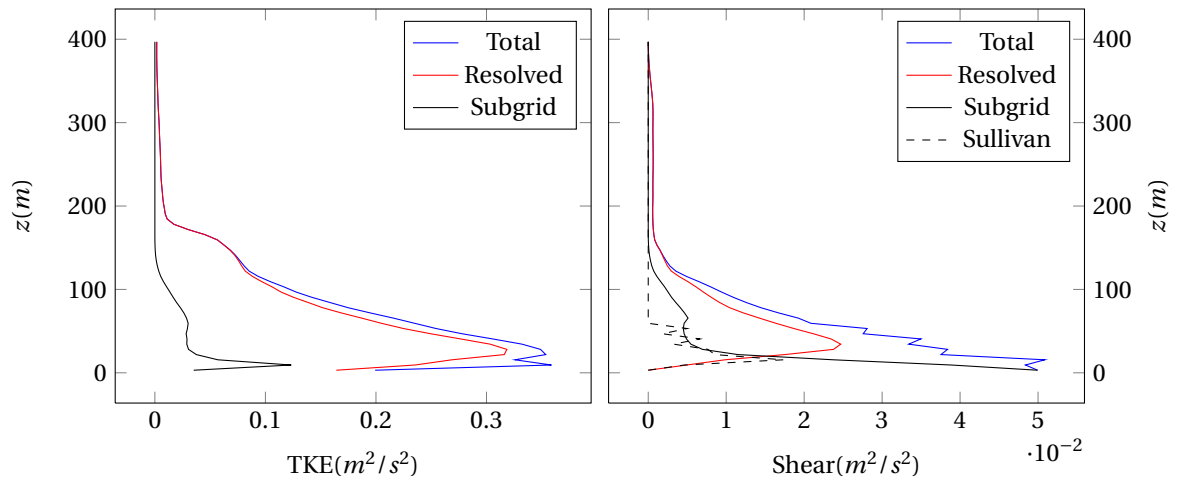
(a) TKE profiles, Δx 25m

(b) Shear profiles, Δx 25m

Figure G.18: TKE and shear profile, Sullivan model with $\gamma = 1$, with $\Delta x = 25m$
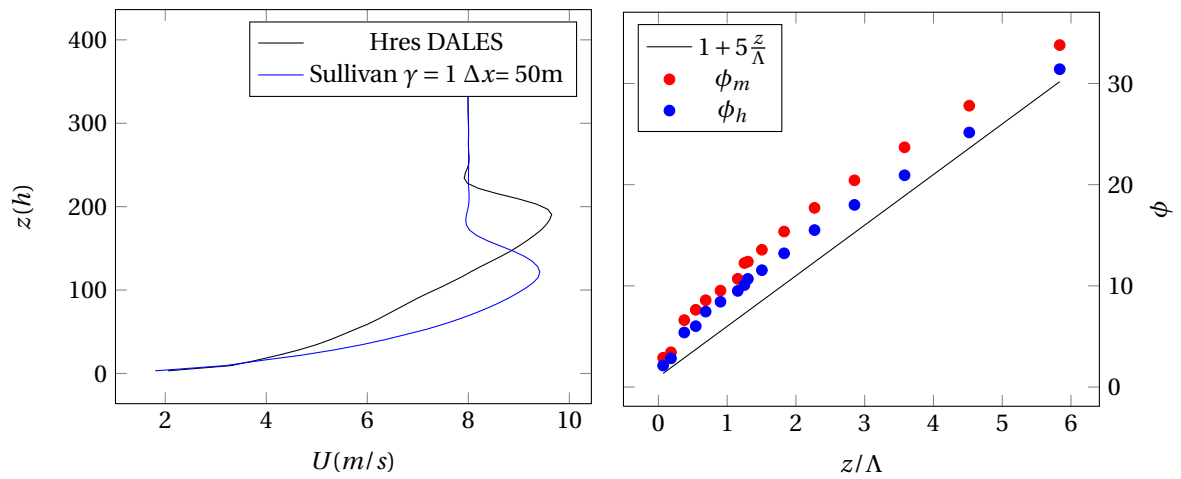
(a) $U_h profile$, $\Delta x = 50m$

(b) Similarity functions, $\Delta x = 50m$

Figure G.19: U_s profile and similarity functions, Sullivan model with $\gamma = 1$, with $\Delta x = 50m$
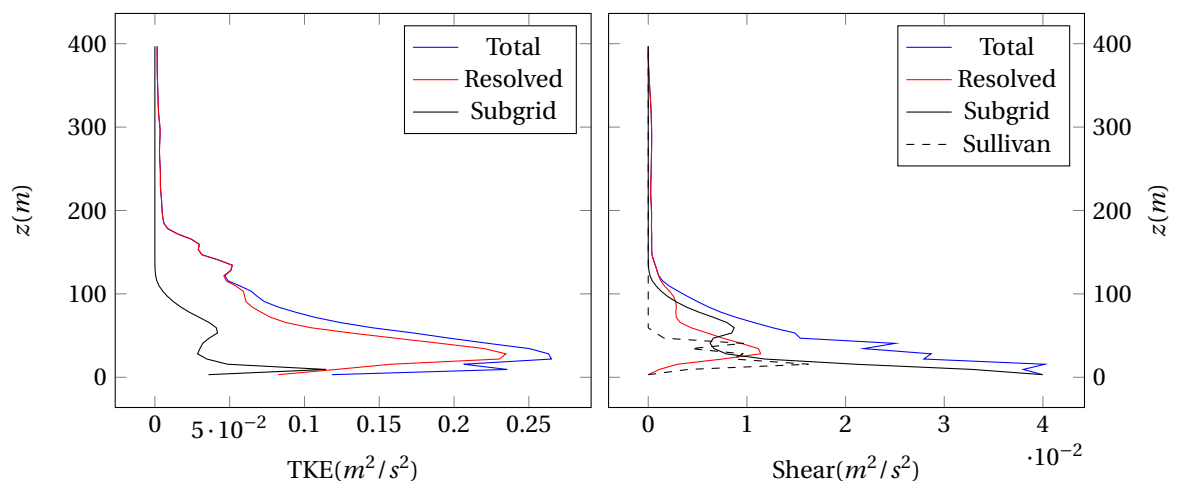
(a) TKE profiles, Δx 50m

(b) Shear profiles, Δx 50m

Figure G.20: TKE and shear profile, Sullivan model with $\gamma = 1$, with $\Delta x = 50m$
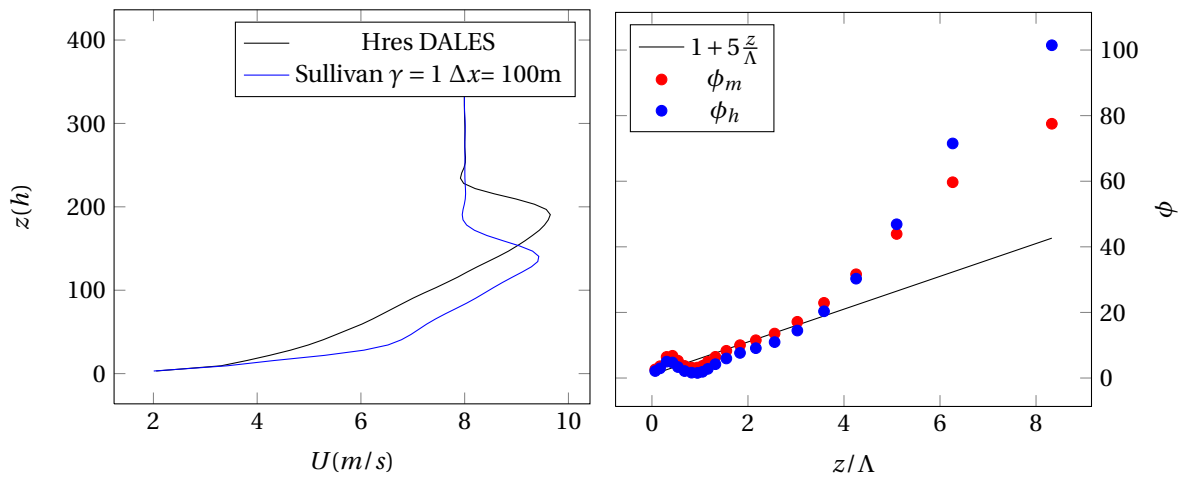
(a) $U_h profile$, $\Delta x = 100m$

(b) Similarity functions, $\Delta x = 100m$

Figure G.21: U_s profile and similarity functions, Sullivan model with $\gamma = 1$, with $\Delta x = 100m$
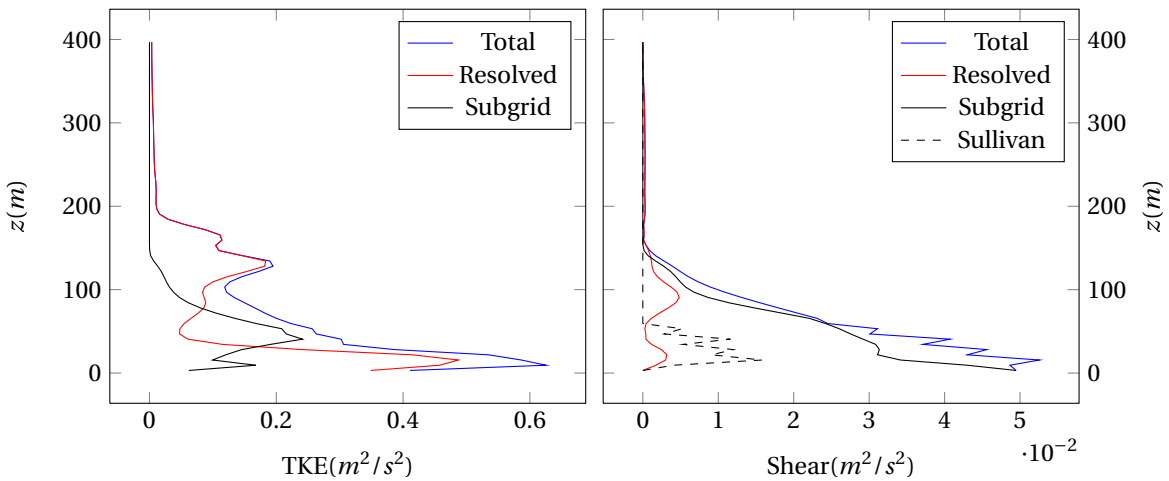
(a) TKE profiles, Δx 100m

(b) Shear profiles, Δx 100m

Figure G.22: TKE and shear profile, Sullivan model with $\gamma = 1$, with $\Delta x = 100m$
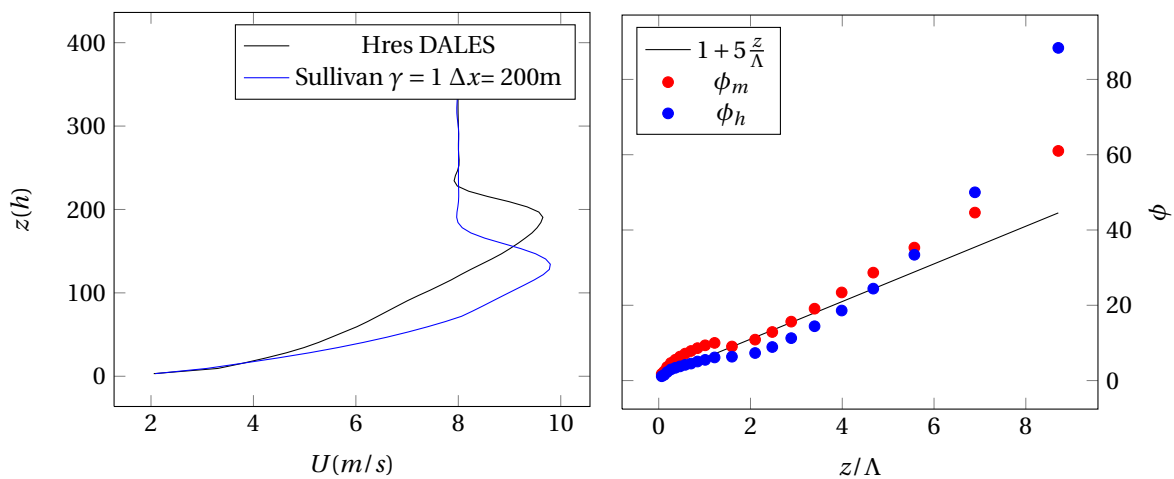
(a) $U_h profile$, $\Delta x = 200m$

(b) Similarity functions, $\Delta x = 200m$

Figure G.23: U_s profile and similarity functions, Sullivan model with $\gamma = 1$, with $\Delta x = 200m$
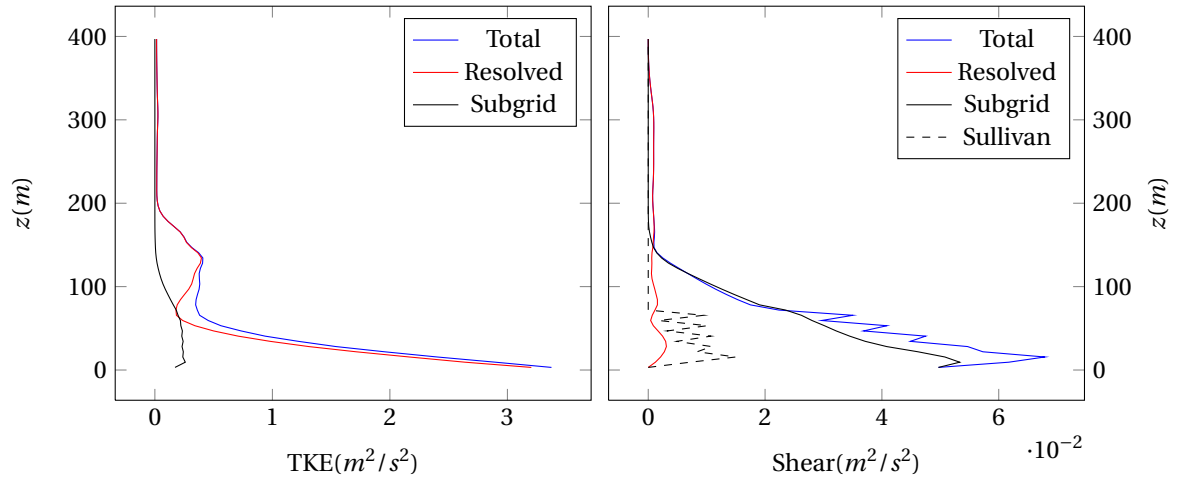
(a) TKE profiles, Δx 200m

(b) Shear profiles, Δx 200m

Figure G.24: TKE and shear profile, Sullivan model with $\gamma = 1$, with $\Delta x = 200m$

G.3. SULLIVAN MODEL WITH SIMPLE MEAN SHEAR EDDY DIFFUSIVITY

The Sullivan model, with K_H given by:

$$K_H = \frac{(\kappa \Delta z)^2}{(\phi_m(\Delta z))^2}\sqrt{2\langle S_{ij}\rangle\langle S_{ij}\rangle} \qquad \text{(G.1)}$$
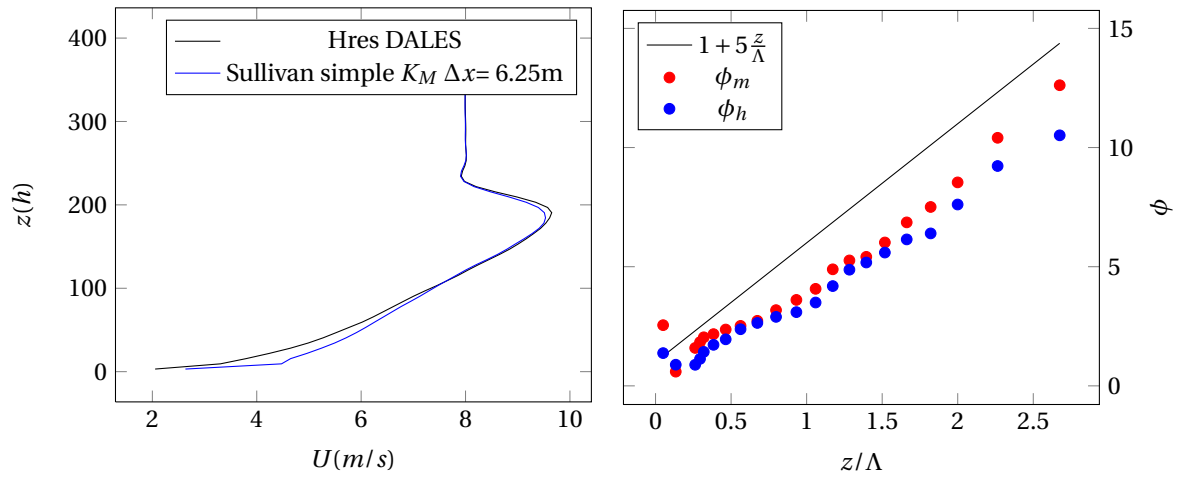
(a) U_h profile, $\Delta x = 6.25m$

(b) Similarity functions, $\Delta x = 6.25m$

Figure G.25: U_h profile and similarity functions, Sullivan model with simple K_M, with $\Delta x = 6.25m$

(a) TKE profiles, Δx 6.25m

(b) Shear profiles, Δx 6.25m
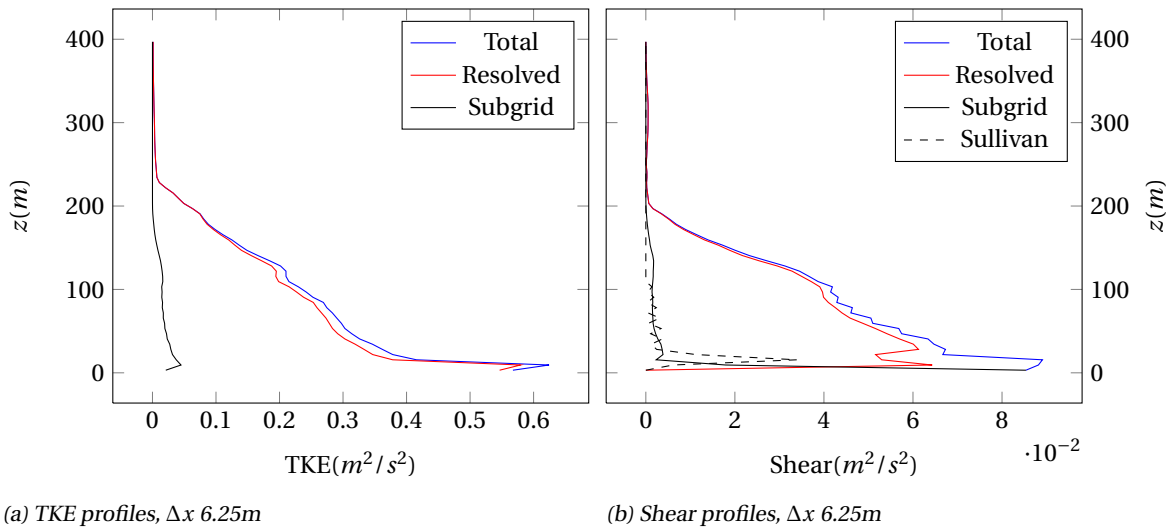
Figure G.26: TKE and shear profile, Sullivan model with simple K_M, with Δx = 6.25m

(a) U_h profile, Δx = 12.5m

(b) Similarity functions, Δx = 12.5m
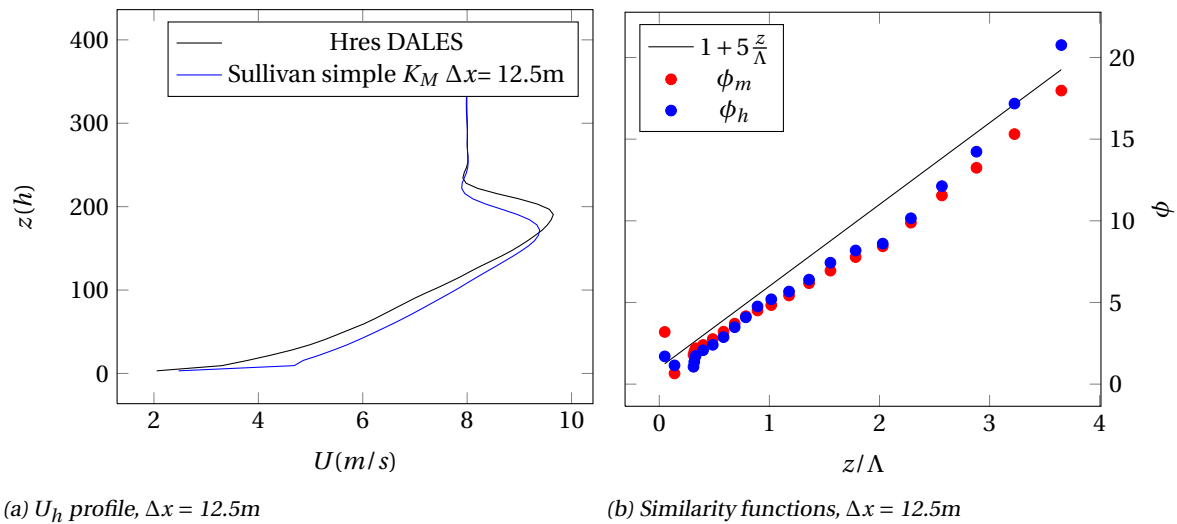
Figure G.27: U_h profile and similarity functions, Sullivan model with simple K_M, with Δx = 12.5m

(a) TKE profiles, Δx 12.5m

(b) Shear profiles, Δx 12.5m
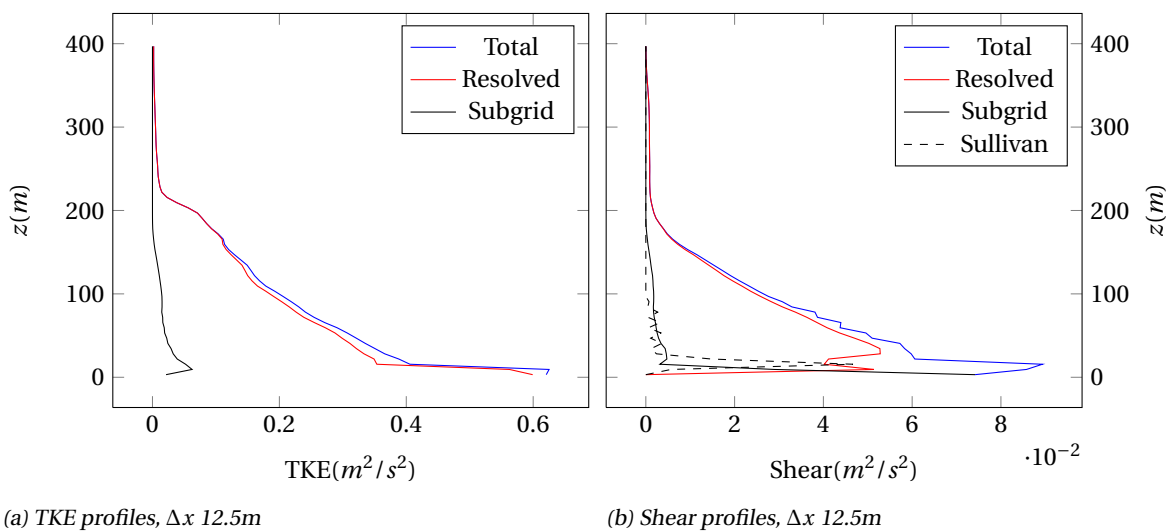
Figure G.28: TKE and shear profile, Sullivan model with simple K_M, with Δx = 12.5m
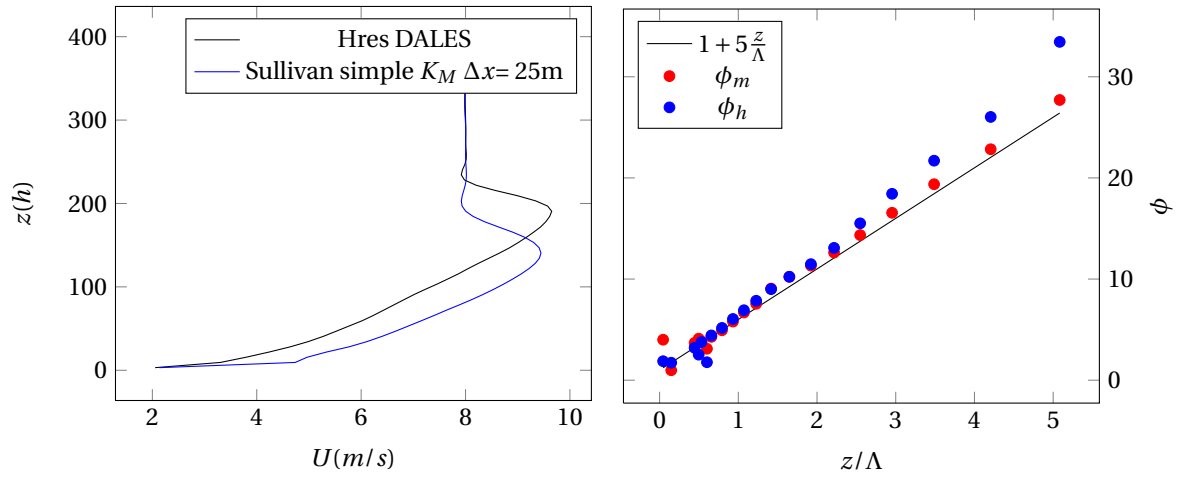
(a) U_h profile, $\Delta x = 25m$

(b) Similarity functions, $\Delta x = 25m$

Figure G.29: U_h profile and similarity functions, Sullivan model with simple K_M, with $\Delta x = 25m$
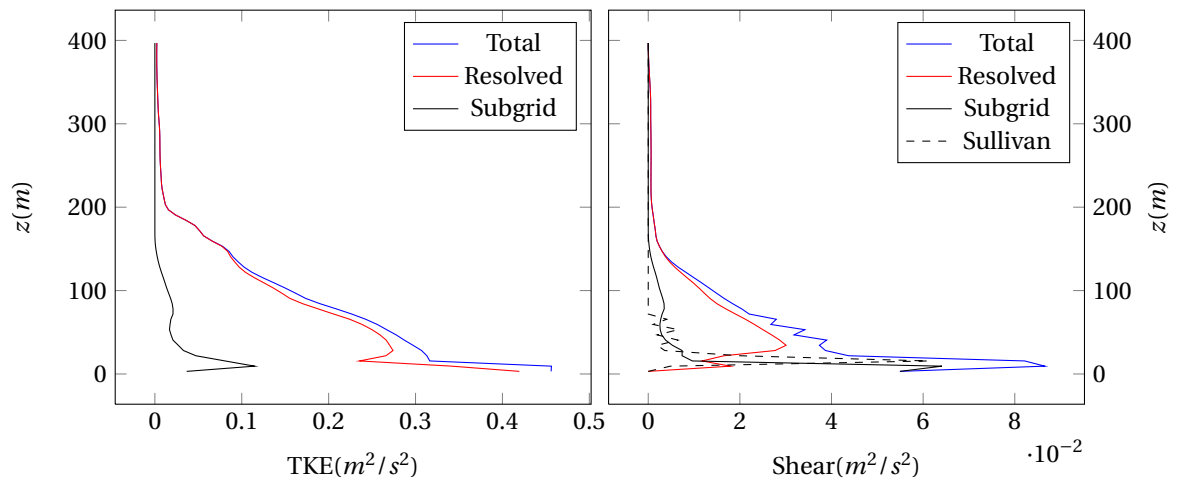
(a) TKE profiles, Δx 25m

(b) Shear profiles, Δx 25m

Figure G.30: TKE and shear profile, Sullivan model with simple K_M, with $\Delta x = 25m$
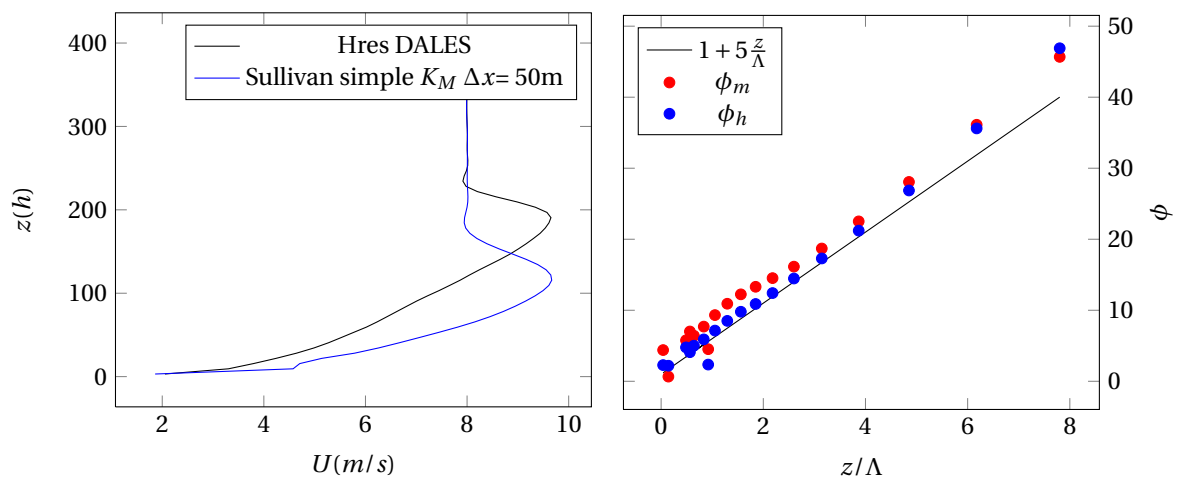
(a) U_h profile, $\Delta x = 50m$

(b) Similarity functions, $\Delta x = 50m$

Figure G.31: U_h profile and similarity functions, Sullivan model with simple K_M, with $\Delta x = 50m$

(a) TKE profiles, Δx 50m

(b) Shear profiles, Δx 50m
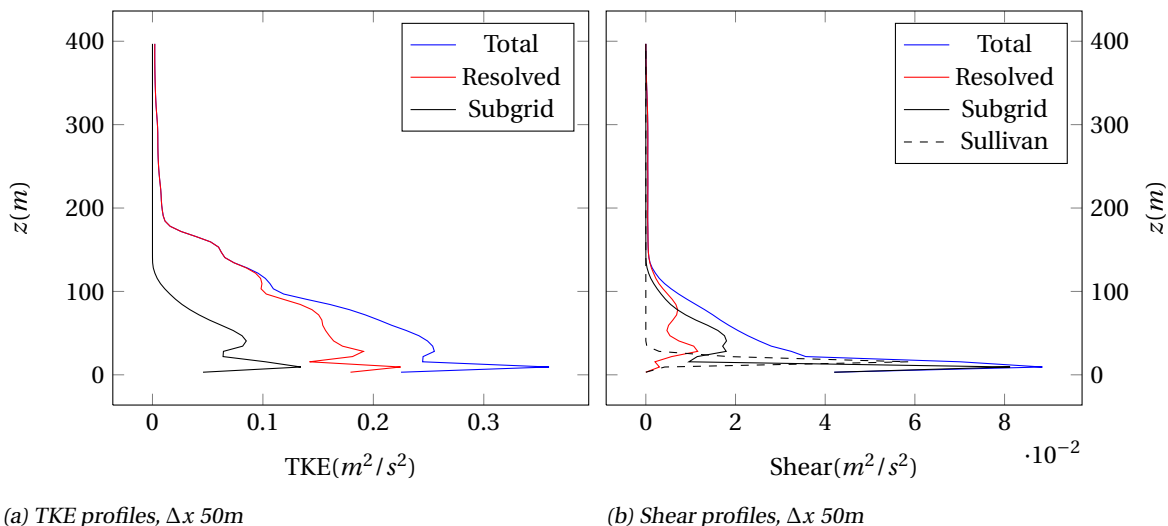
Figure G.32: TKE and shear profile, Sullivan model with simple K_M, with $\Delta x = 50m$

(a) U_h profile, Δx = 100m

(b) Similarity functions, Δx = 100m
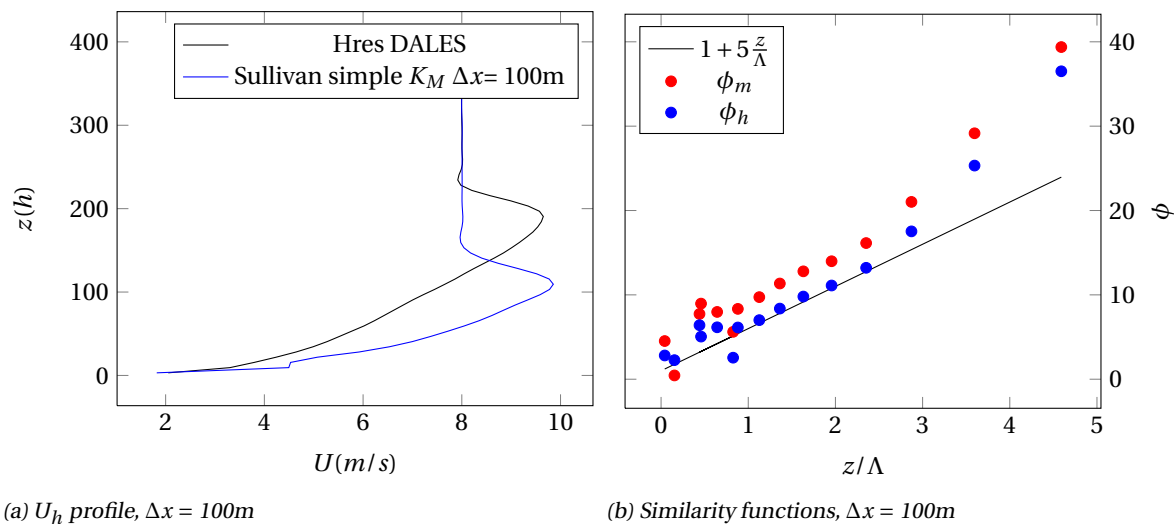
Figure G.33: U_h profile and similarity functions, Sullivan model with simple K_M, with $\Delta x = 100m$

(a) TKE profiles, Δx 100m

(b) Shear profiles, Δx 100m
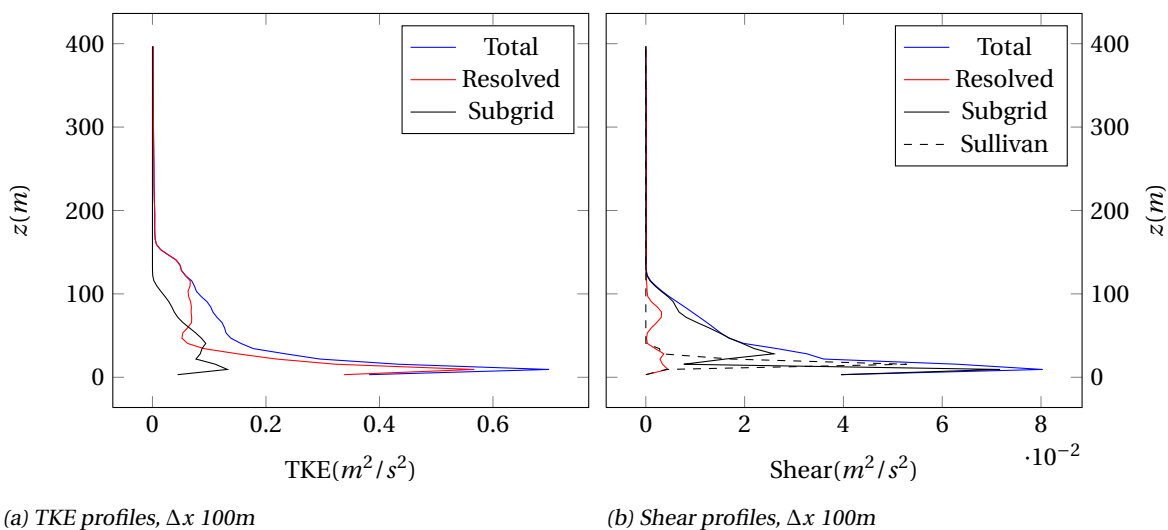
Figure G.34: TKE and shear profile, Sullivan model with simple K_M, with $\Delta x = 100m$
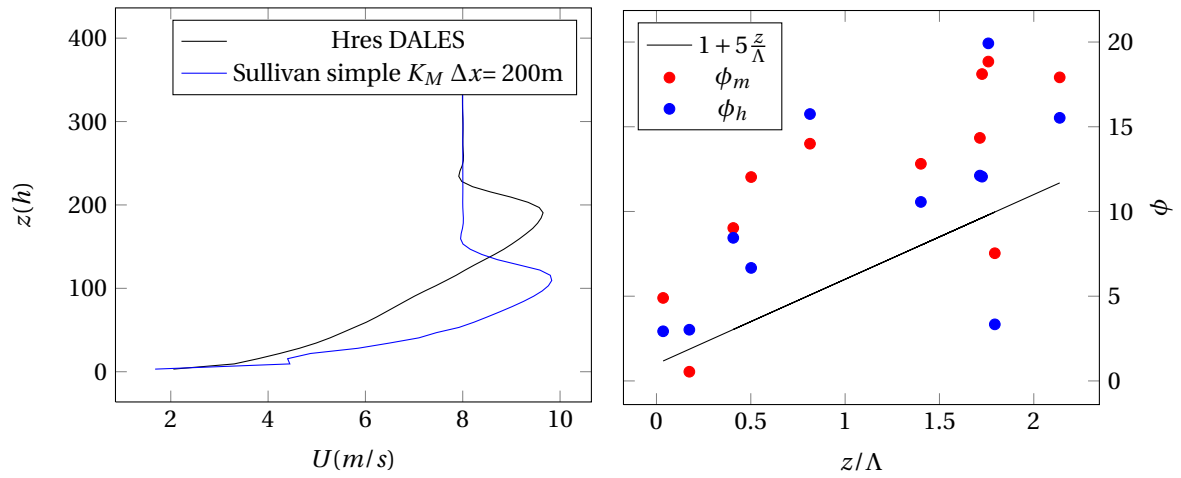
(a) U_h profile, $\Delta x = 200m$

(b) Similarity functions, $\Delta x = 200m$

Figure G.35: U_h profile and similarity functions, Sullivan model with simple K_M, with $\Delta x = 200m$
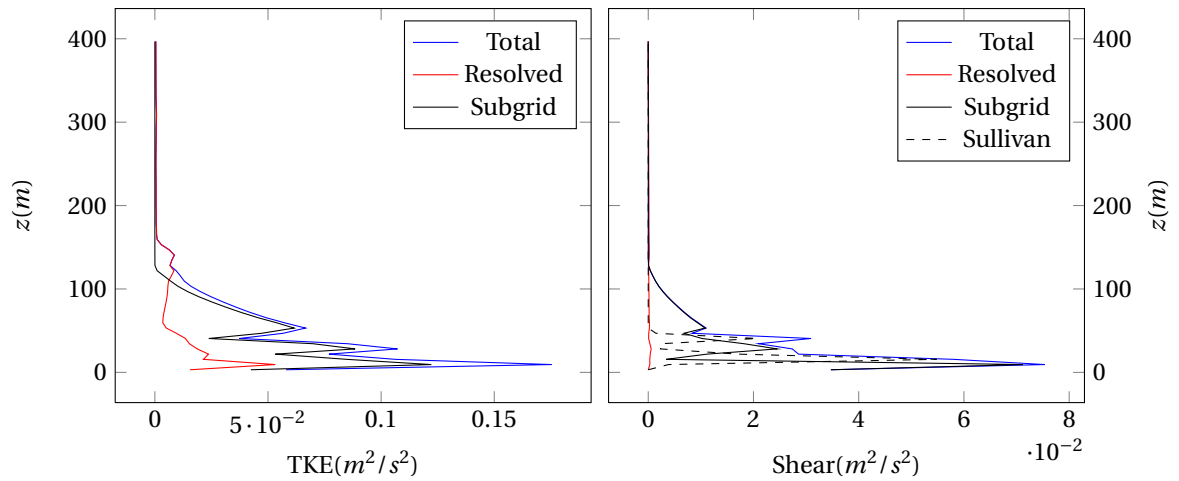
(a) TKE profiles, Δx 200m

(b) Shear profiles, Δx 200m

Figure G.36: TKE and shear profile, Sullivan model with simple K_M, with $\Delta x = 200m$

G.4. SULLIVAN MODEL WITH ADAPTED HEAT EDDY DIFFUSION

The combination of the original model by Sullivan, and the adaption to the eddy heat diffusion described in Section 5.4.
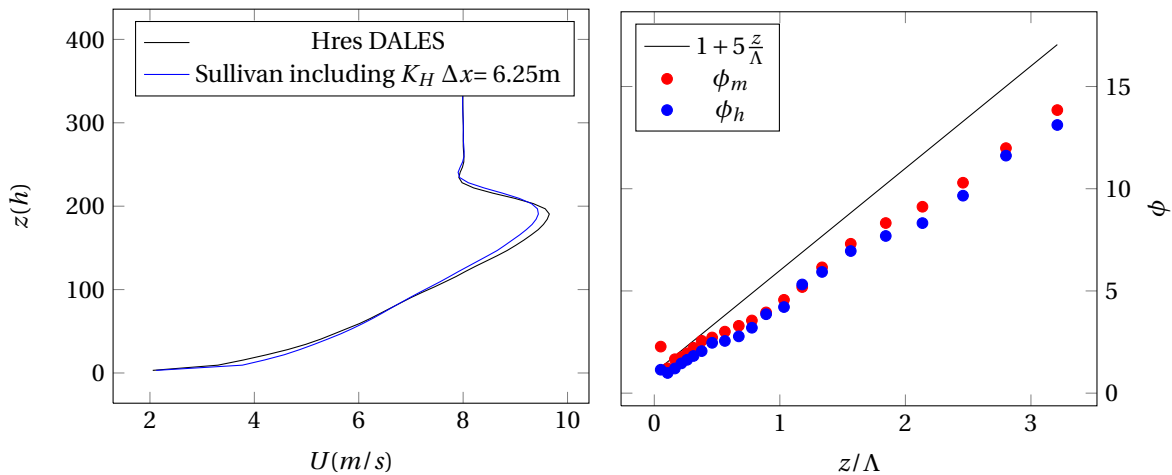
(a) U_h profile, $\Delta x = 6.25m$

(b) Similarity functions, $\Delta x = 6.25m$

Figure G.37: U_h profile and similarity functions, Sullivan model with K_H, with $\Delta x = 6.25m$
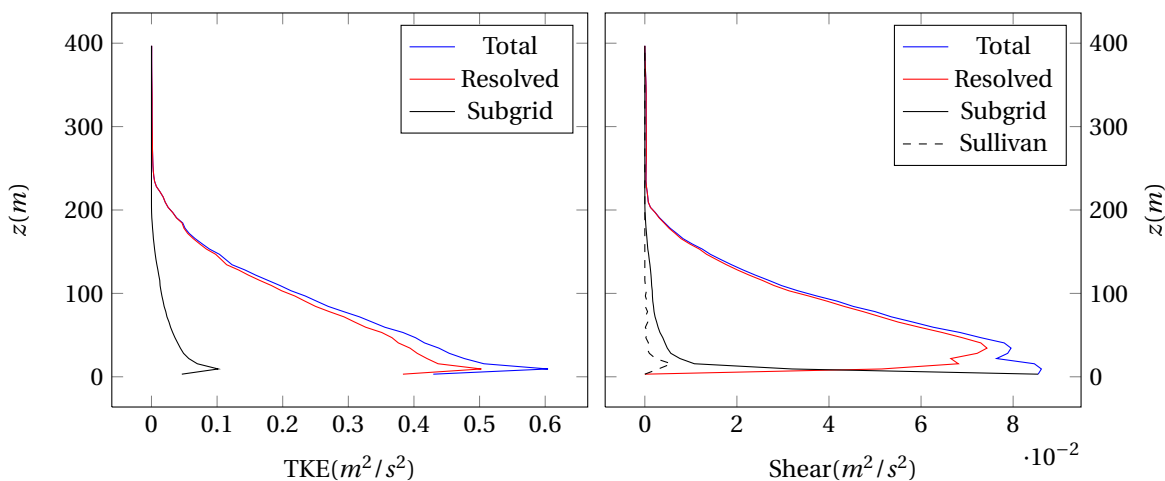
(a) TKE profiles, Δx 6.25m

(b) Shear profiles, Δx 6.25m

Figure G.38: TKE and shear profile, Sullivan model with K_H, with $\Delta x = 6.25m$
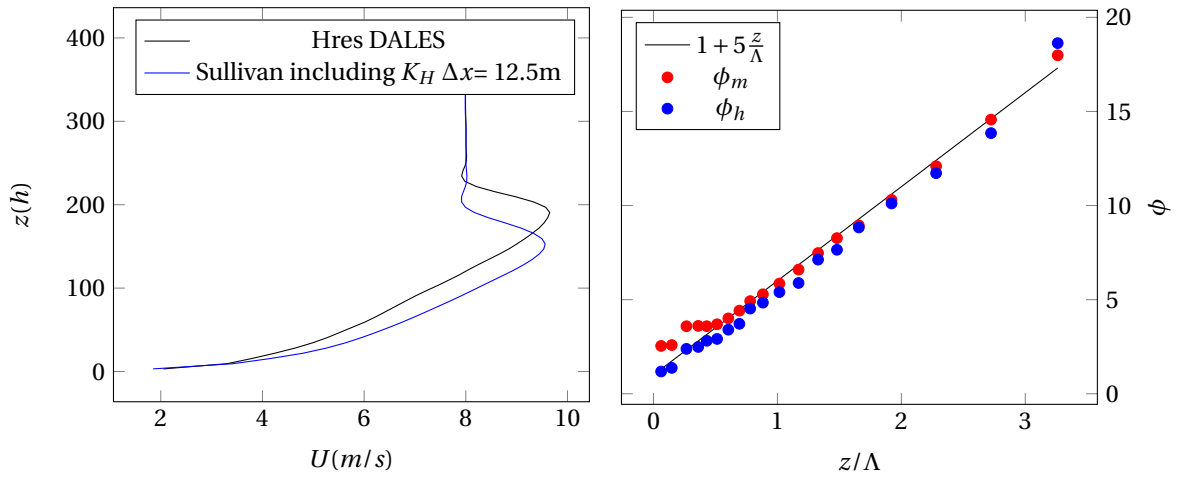
(a) U_h profile, $\Delta x = 12.5m$

(b) Similarity functions, $\Delta x = 12.5m$

Figure G.39: U_h profile and similarity functions, Sullivan model with K_H, with $\Delta x = 12.5m$
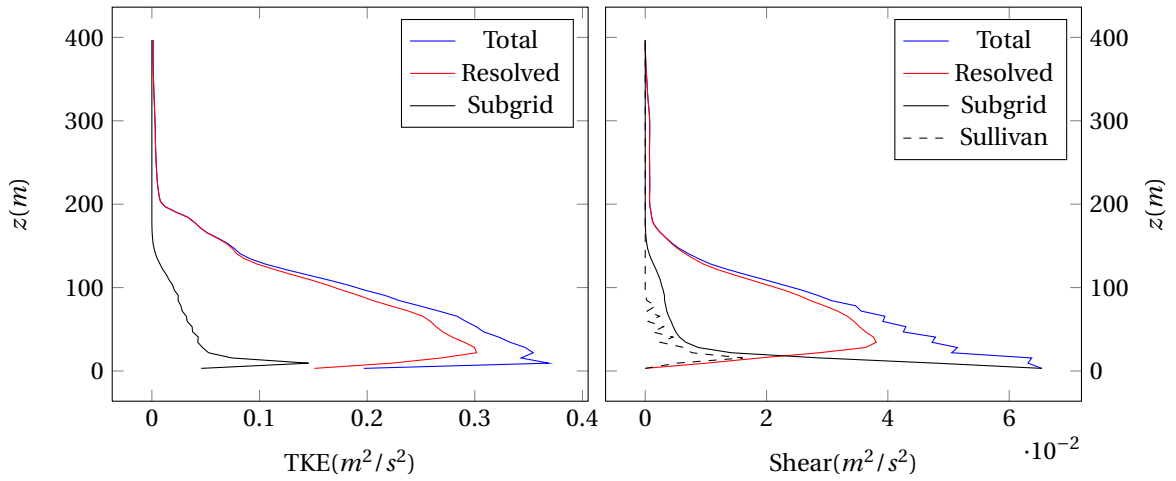
(a) TKE profiles, Δx 12.5m

(b) Shear profiles, Δx 12.5m

Figure G.40: TKE and shear profile, Sullivan model with K_H, with $\Delta x = 12.5m$
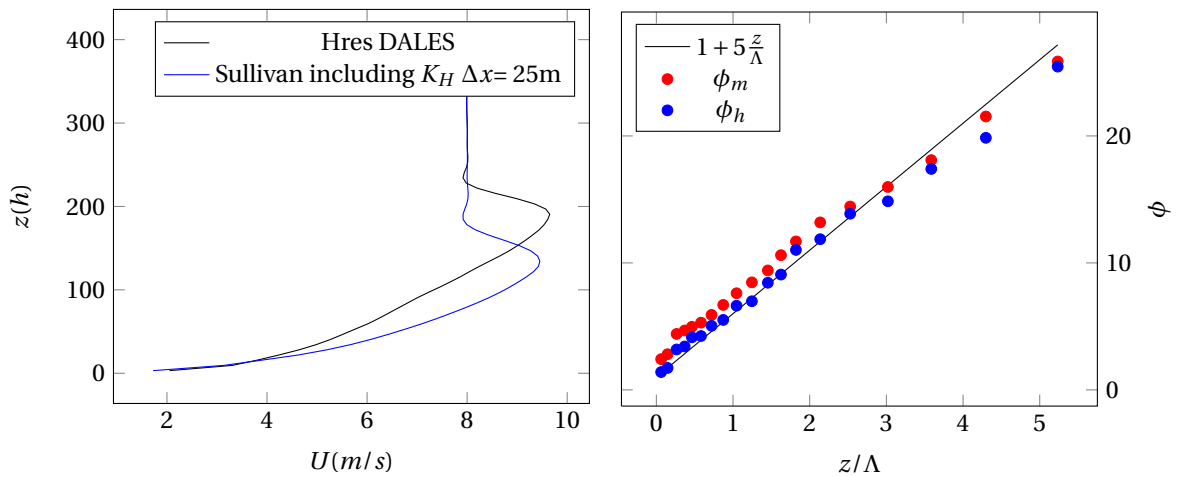
(a) U_h profile, $\Delta x = 25m$

(b) Similarity functions, $\Delta x = 25m$

Figure G.41: U_h profile and similarity functions, Sullivan model with K_H, with $\Delta x = 25m$

(a) TKE profiles, Δx 25m

(b) Shear profiles, Δx 25m
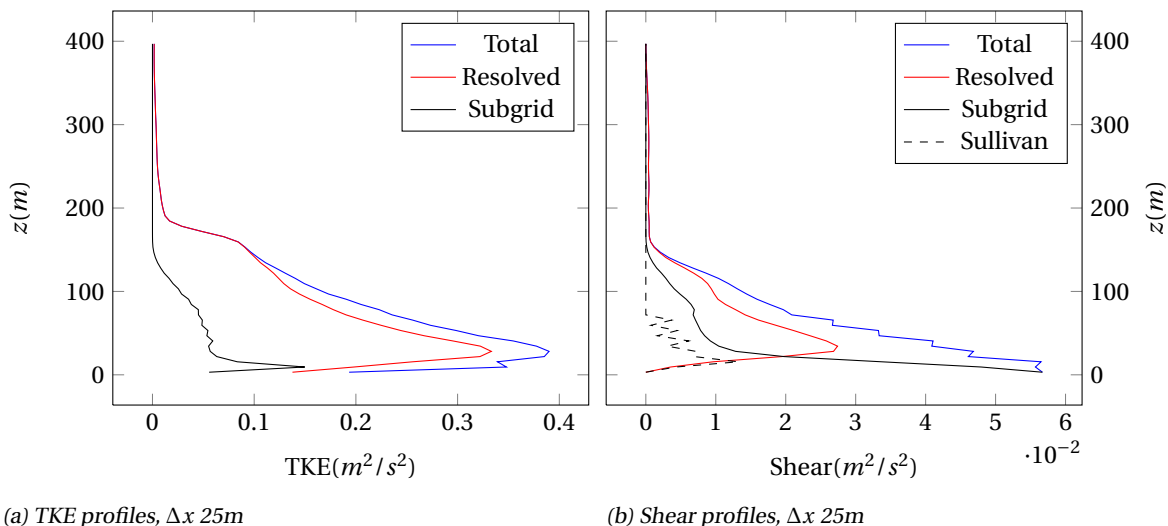
Figure G.42: TKE and shear profile, Sullivan model with K_H, with $\Delta x = 25m$

(a) U_h profile, $\Delta x = 50m$

(b) Similarity functions, $\Delta x = 50m$
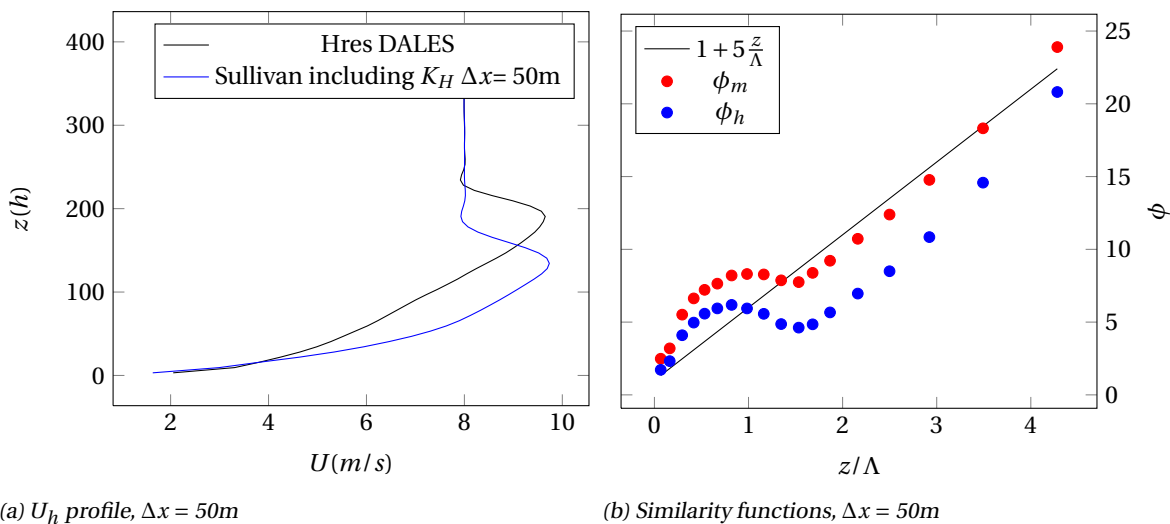
Figure G.43: U_h profile and similarity functions, Sullivan model with K_H, with $\Delta x = 50m$

(a) TKE profiles, Δx 50m

(b) Shear profiles, Δx 50m
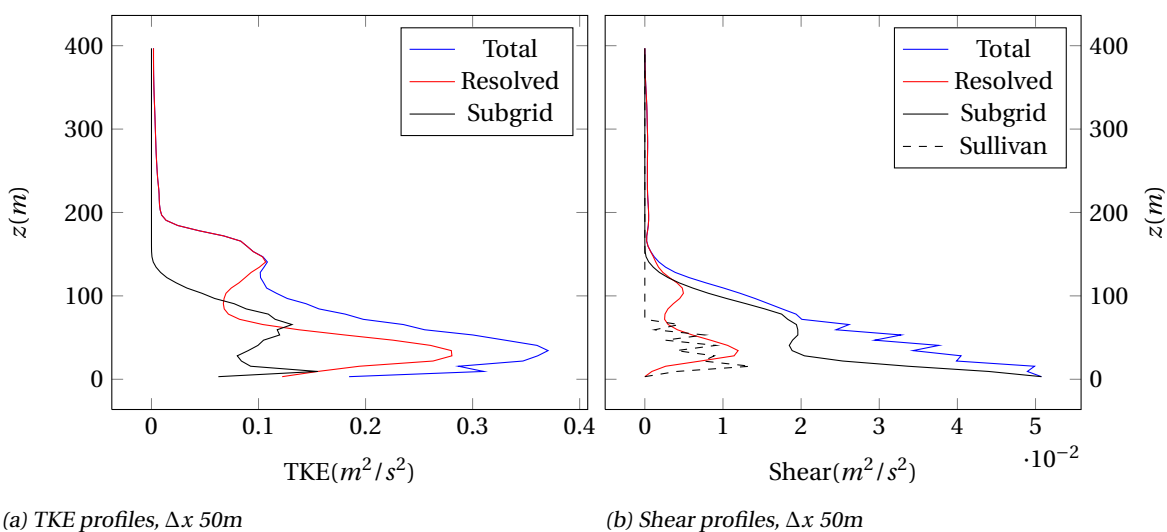
Figure G.44: TKE and shear profile, Sullivan model with K_H, with $\Delta x = 50m$